INFORMATION TO USERS

The most advanced technology has been used to photograph and reproduce this manuscript from the microfilm master. UMI films the text directly from the original or copy submitted. Thus, some thesis and dissertation copies are in typewriter face, while others may be from any type of computer printer.

The quality of this reproduction is dependent upon the quality of the copy submitted. Broken or indistinct print, colored or poor quality illustrations and photographs, print bleedthrough, substandard margins, and improper alignment can adversely affect reproduction.

In the unlikely event that the author did not send UMI a complete manuscript and there are missing pages, these will be noted. Also, if unauthorized copyright material had to be removed, a note will indicate the deletion.

Oversize materials (e.g., maps, drawings, charts) are reproduced by sectioning the original, beginning at the upper left-hand corner and continuing from left to right in equal sections with small overlaps. Each original is also photographed in one exposure and is included in reduced form at the back of the book. These are also available as one exposure on a standard 35mm slide or as a 17" x 23" black and white photographic print for an additional charge.

Photographs included in the original manuscript have been reproduced xerographically in this copy. Higher quality 6" x 9" black and white photographic prints are available for any photographs or illustrations appearing in this copy for an additional charge. Contact UMI directly to order.

U·M·I

University Microfilms International
A Bell & Howell Information Company
300 North Zeeb Road, Ann Arbor, MI 48106-1346 USA
313/761-4700 800/521-0600

Order Number 9001976

Trajectory studies of diatom-surface scattering

Kay, Ronald Dale, Ph.D.

The Ohio State University, 1989

U·M·I
300 N. Zeeb Rd.
Ann Arbor, MI 48106

TRAJECTORY STUDIES OF DIATOM — SURFACE SCATTERING

DISSERTATION

Presented in Partial Fulfillment of the Requirements for

the Degree Doctor of Philosophy in the Graduate

School of the Ohio State University

By

Ronald Dale Kay, B. A.

* * * * *

The Ohio State University

1989

Dissertation Committee:

P. L. Jones

J. M. Parson

S. J. Singer

Approved by

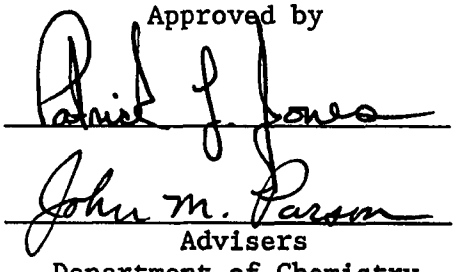

Advisers
Department of Chemistry

To my Lord, Jesus Christ, who by His power created the universe and all that is in it, and who by His grace has made me a new creation in Him.

ACKNOWLEDGMENTS

The following people deserve special mention for their contributions to this work and to my life:

I am grateful to all the people with whom I worked at Sandia National Laboratories, particularly to Bruce Kay and Keith Lykke for providing their experimental data for use in Chapter IV, to Merle Riley for all the help and advice on the REOM work in Chapters V and VI, and especially to Mike Coltrin, both for his immense help and for his friendship.

I deeply appreciate the many friends who have challenged and encouraged me throughout my graduate work. Most notable among these are Bob Mosteller, Ed Look, Bill Loffredo, David Barbee, Dan McMullen, Kevin McMahan, Bill Scott, Sue Scott, Ron McLean and Steve Smith. I also remember with joy the many wonderful people at Christ's Church in Columbus, at Hoffmantown Baptist Church in Albuquerque, and at the Bible study at the Joseph's home.

I offer my advisor, Pat Jones, my sincerest thanks for arranging the trip to Sandia where this work began, and for consistently encouraging me to stretch myself to my limits.

Above all, I express my deepest gratitude to my parents, John and Shirley Kay, whose faith in me never wavered, and who continually supported and encouraged me throughout these seven years.

VITAE

May 29, 1960	Born — Akron, Ohio
1982	B. A., Gordon College, Wenham, Massachusetts
1982 — 1983	University Fellow, the Ohio State University
1983 — 1984	Graduate Teaching Associate, Department of Chemistry, the Ohio State University
1984 — 1985	Graduate Research Associate, Department of Chemistry, the Ohio State University
1985 — 1986	Phillips Petroleum Graduate Fellow, Department of Chemistry, the Ohio State University
1986 — 1987	Graduate Teaching Associate, Department of Chemistry, the Ohio State University
October 1987 — March 1988	Researcher, Sandia National Laboratories, Albuquerque, New Mexico
1988 — present	Graduate Student and Teaching Associate, Department of Chemistry, the Ohio State University

FIELDS OF STUDY

Major Field: Chemistry

Studies in Gas-Surface Scattering, Dr. Patrick L. Jones, Advisor

TABLE OF CONTENTS

LIST OF TABLES

LIST OF FIGURES

CHAPTER I

INTRODUCTION

This dissertation presents the results of investigations into the interactions of diatomic molecules with solid surfaces using the quasiclassical trajectory (QCT) method. In particular, studies have been made on the scattering of HCl molecules from gold and of NO molecules from lithium fluoride. In the former case, the object is to obtain at least a qualitative understanding of the HCl/Au(111) collision dynamics by finding a model gas-surface interaction potential which produces results in accord with recent experiments.[1] In the latter case, the goal is to evaluate a new reduced equations of motion (REOM) method[2] for including into a scattering calculation energy transfer between a gas molecule and a surface. This assessment is made by comparing the REOM results to those from detailed calculations for the NO/LiF(001) system[3] using the stochastic trajectory method.[4]

The dissertation is divided into three parts, each containing two chapters. The first part, consisting of Chapters I and II, provides an introduction to the work presented in the second and third parts. Chapter I surveys the literature concerning gas-surface scattering theory. Chapter II discusses the procedures employed to implement the quasiclassical trajectory method in these studies. The second part of the dissertation, Chapters III and IV, discusses the work on scattering of HCl

from gold. Chapter III explains the construction of the gas-surface interaction potentials used in the calculations and provides other relevant numerical details. In Chapter IV, the calculations are presented and compared with the experimental results. The final part, Chapters V and VI, describes the calculations performed on the NO/LiF(001) system using the REOM approach. The derivation of the REOM, a discussion of the partial velocity reset procedure,[5] a description of the gas-surface interaction potential and an explanation of computational details comprise Chapter V. Chapter VI is devoted to the evaluation of the REOM method by comparing results obtained from it to those obtained from the stochastic trajectory method.

Overview of Gas-Surface Scattering Theory

The interactions of gases with solid surfaces occur in a broad spectrum of fundamentally important processes, such as catalysis, semiconductor fabrication and lift and drag on airfoils. The prevalence of gas-surface phenomena provides an incentive to understand these processes in the greatest possible detail. In the last two decades or so, tremendous progress in achieving such an understanding has been made, due to advances in both experimental and theoretical techniques. On the experimental side, improvements in ultra-high-vacuum technology, laser and molecular beam techniques and surface preparation and analysis methods have made possible detailed studies of the interactions of atoms and molecules with surfaces. These in turn have stimulated the development of theoretical models to qualitatively, and sometimes quantitatively, understand

the experimental results. The advent of larger and faster computers has also aided the growth of the theory. Comprehensive reviews concerning the experimental[6-8] and theoretical[9,10] techniques exist in the literature.

The goal of the following discussion is to locate the present work within the field of gas-surface interactions as a whole. Since these studies involve theory, experimental studies will be mentioned only briefly, in the context of their relation to particular theoretical models. Furthermore, since the gas-phase species in this work are diatomic molecules, emphasis will be given in the discussion to theory dealing with molecular rather than atomic collisions with surfaces. The overview begins by describing in Section A the exact quantum mechanical treatment of the scattering problem, known as the "close-coupling" (CC) method. Then Section B outlines the various approximate treatments, from the quantum mechanical, semiclassical and classical mechanical regimes, which have been used to model molecule-surface collisions.

A. The Exact Quantum-Mechanical Method: Close-Coupling

The exact quantum-mechanical solution for the scattering of a molecule from a surface begins with the time-independent Schrödinger equation (TISE), which, in the Born-Oppenheimer approximation, is given by

$$\hat{H}_{tot}(\vec{R},\vec{r},\vec{\xi})\ \psi(\vec{R},\vec{r},\vec{\xi}) = E_{tot}\ \psi(\vec{R},\vec{r},\vec{\xi})\ , \qquad (1.1)$$

where $\vec{R}$ and $\vec{r}$ denote the center-of-mass and internal coordinates of the

molecule, $\vec{\xi}$ represents the coordinates of the surface atoms, ψ is the total wavefunction and E_{tot} the total energy of the system, and $\hat{H}_{tot}$ is the Hamiltonian operator, given by

$$\hat{H}_{tot} = -\frac{\hbar^2}{2M}\left[\frac{\partial^2}{\partial X^2}+\frac{\partial^2}{\partial Y^2}+\frac{\partial^2}{\partial Z^2}\right] + \hat{H}_{int}(\vec{r}) + \hat{H}_s(\xi) + V(\vec{R},\vec{r},\vec{\xi}). \quad (1.2)$$

M is the reduced mass of the molecule-solid system, $\vec{R} = (X,Y,Z)$, $\hat{H}_{int}$ and $\hat{H}_s$ are the Hamiltonians for the internal motion of the molecule and the solid, respectively, and V is the gas-surface interaction potential. Because the solid contains so many atoms, solution of equation (1.1) is extremely difficult. Consequently, the rigid-surface approximation is usually invoked. When this is done, $\hat{H}_s$ in equation (1.2) is zero, the $\vec{\xi}$-dependence of ψ and V is suppressed and M becomes the mass of the molecule. Wolken[11] was the first to apply equation (1.1) to molecule-surface scattering. Assuming a rigid, perfectly periodic surface lattice, he expanded the wavefunction ψ and the potential V as

$$\psi(\vec{R},\vec{r}) = \sum_{vjmkl} (1/r)\, u_{vj}(r)\, Y_{jm}(\theta,\phi)\, \exp\{i(\vec{K}+\vec{G}_{kl})\cdot\vec{\rho}\}\, f_{vjmkl}(Z), \quad (1.3a)$$

$$V(\vec{R},\vec{r}) = \sum_{kl} v_{kl}(Z,\vec{r})\, \exp(i\vec{G}_{kl}\cdot\vec{\rho}), \quad (1.3b)$$

where $\vec{r} = (r,\theta,\phi)$, $\vec{\rho} = (X,Y,0)$ is the component of $\vec{R}$ parallel to the surface, $\vec{K} = (k_X,k_Y,0)$ is the component parallel to the surface of the incident center-of-mass wavevector $\vec{k}$, $\vec{G}_{kl}$ is a reciprocal lattice vector, $u_{vj}(r)$ is a radial wavefunction, $Y_{jm}(\theta,\phi)$ is a spherical

harmonic, and $f_{vjmkl}(Z)$ and $v_{kl}(Z,\vec{r})$ are the expansion coefficients, which depend on Z, the component of $\vec{R}$ normal to the surface. The indices v, (j,m) and (k,l) are the vibrational, rotational and diffraction quantum numbers, respectively. The wavefunction $\chi_{vjm}(\vec{r}) = (1/r)u_{vj}(r)Y_{jm}(\theta,\phi)$ is an eigenfunction of $\hat{H}_{int}$ with eigenvalue ε_{vj}. By substituting equations (1.3) into (1.1), multiplying each side by χ^*_{vjm} $\exp(-i\vec{G}_{k'l'}\cdot\vec{\rho})$ and integrating over $\vec{r}$ and $\vec{\rho}$, Wolken derived the coupled-channel equations for the amplitudes $f_{vjmkl}(Z)$, written in matrix form as[11]

$$\left[\underline{\underline{1}} \frac{d^2}{dZ^2} + \underline{\underline{D}}^2 \right] \underline{\underline{f}}(Z) = \underline{\underline{V}}(Z)\, \underline{\underline{f}}(Z), \tag{1.4}$$

where $\underline{\underline{1}}$ is the unit matrix, $\underline{\underline{f}}(Z)$ is the matrix whose columns are sets of amplitudes $f_{vjmkl}(Z)$ corresponding to different initial conditions, and the elements of the diagonal matrix $\underline{\underline{D}}^2$ and the square matrix $\underline{\underline{V}}(Z)$ are

$$D^2_{v'j'm'k'l',vjmkl} = \delta_{v'v}\,\delta_{j'j}\,\delta_{m'm}\,\delta_{k'k}\,\delta_{l'l} \times \left[\frac{2M}{\hbar^2}(E_{tot} - \varepsilon_{vj}) - (\vec{K} + \vec{G}_{kl}) \right], \tag{1.5}$$

$$V_{v'j'm'k'l',vjmkl}(Z) = \frac{2M}{\hbar^2} \langle \chi_{v'j'm'} \mid v_{\Delta k \Delta l}(\vec{r},Z) \mid \chi_{vjm} \rangle. \tag{1.6}$$

In equation (1.6), $\Delta k = k'-k$, $\Delta l = l'-l$, and the integration is over $\vec{r}$. The scattering problem is solved by integrating the coupled equations (1.4) according to the standard boundary conditions:[11,12]

$$\underline{\underline{f}}(Z \to -\infty) \sim \underline{\underline{0}} \tag{1.7a}$$

$$\underline{\underline{f}}(Z \to +\infty) \sim \underline{\underline{0}} \quad \text{for closed channels } (D^2_{vjmkl} < 0) \tag{1.7b}$$

$$\underline{\underline{f}}(Z \to +\infty) \sim \underline{\underline{I}} + \underline{\underline{O}}\,\underline{\underline{S}} \quad \text{for open channels } (D^2_{vjmkl} < 0) \tag{1.7c}$$

where $\underline{\underline{I}}$ and $\underline{\underline{O}}$ are diagonal matrices of flux-normalized incoming and outgoing asymptotic (plane-wave) solutions, and $\underline{\underline{S}}$ is the scattering matrix (S matrix), which contains all the scattering information. If i and f denote the initial and final channel quantum numbers (that is, sets of quantum numbers vjmkl), then the probability amplitude for the $i \to f$ transition is given by $|S_{fi}|^2$.

In principle, the expansion of the wavefunction ψ in terms of the basis of internal and diffraction states, equation (1.3a), includes an infinite number of basis functions (channels). In practice, however, it suffices to employ a limited number of channels to obtain converged transition probabilities; the size of the basis is determined empirically, based on the desired degree of accuracy and the available computer capacity. Since the computational effort scales as N^3, where N is the number of channels in the basis,[13] the close-coupling method becomes prohibitively expensive for systems having a large number of open channels. Thus, most of the applications of this technique have been to the scattering of light molecules such as H_2, D_2 and HD at low energies (0.1 eV or so), for which a small number of internal-diffraction channels are open. Wolken[11] applied the CC formalism to H_2/LiF(001) scattering, to compare with the experiments of O'Keefe *et al.*[14] He used basis sets containing 16 and 34 channels at E_{tot} = 104 meV, and found good agreement with the experimental results. Schinke used a basis of 54 channels at 60 meV (nine diffraction states for each of three open and

three closed rotational states) in his thorough study of rotationally-mediated selective adsorption (RMSA) resonances in HD/Pt(111) scattering,[15] which had previously been experimentally observed by Cowin and coworkers.[16] Lill and Kouri[12] tested calculations for H_2/corrugated-surface collisions using approximate techniques against close-coupled results obtained with a basis of 90 channels (15 diffraction for each of six rotational states) at E_{tot} = 0.1 eV. Drolshagen *et al.*[17] performed "benchmark" calculations using the same potential energy function as Wolken[11], but at energies up to 0.7 eV, in order to evaluate approximate techniques employed at these energies. This work involved several basis sets, the largest containing 64 channels (which for normal incidence was by symmetry equivalent to 340 channels). The largest CC calculation reported for a molecule scattering from a corrugated surface, by Lill and Kouri,[18] contained 225 rotation-diffraction states.

Because of the experimental interest[6-8] in scattering of heavier molecules from surfaces at higher energies, various close-coupled calculations for such systems have also been performed. For heavier molecules the number of open diffraction and rotational states increases rapidly. However, many of the experimental studies involve low-corrugation surfaces, such as the (111) face of transition metals, and the experiments do not resolve the closely-spaced diffraction peaks. Thus the flat-surface approximation (in which there is no diffraction) is employed in close-coupling studies of these systems. Of particular interest has been the scattering of NO from Ag(111), for which detailed experimental measurements[19-25] have been conducted for a wide range of incident energies, angles and surface temperatures. These have yielded final

rotational state distributions,[19,24,25] angular distributions,[20] spin-orbit and Λ-doublet populations[21,25] and degree of polarization of the rotational angular momentum.[22,23] One of the most interesting results of the experiments was a bimodal rotational state distribution.[19,25] At low final j, the distribution exhibited "statistical" behavior (linear Boltzmann plot), while a broad maximum appeared at high j, which was identified as a "rotational rainbow". Barker *et al.*[26] modeled NO/Ag(111) as a homonuclear molecule impinging on a flat surface, and performed CC calculations using all even rotational states $j \leq 54$ (28 channels), and obtained marginal success in reproducing the bimodality. Voges and Schinke[27] did better by using an asymmetric potential appropriate for a heteronuclear diatomic like NO, and keeping both even and odd j channels. Based on this work, they attributed the bimodal distribution to rotational rainbows at both low and high j. Lauderdale *et al.*[28] used a 55-channel basis (all $j \leq 54$) to investigate the observed[22,23] rotational polarization. The largest basis set yet reported for close-coupling calculations using standard methods is that employed by Smedley *et al.*[29] to study collisions of $^2\Pi$ molecules (like NO) with a surface. Their calculations were designed to properly include the spin-orbit and Λ-doublet states of the molecule, and thus required 4 channels for a given j; at an energy comparable to that used in the experiments of Luntz *et al.*[21] this required $j \leq 70.5$, or 282 channels. Brenig and coworkers[30] developed an alternative CC method by expressing the Schrödinger equation as an integral equation in terms of Jost functions,[31] which for Morse-type potentials is very fast since the necessary integrals for the Jost functions can be done analytically.

They performed a series of calculations on the NO/Ag(111) system,[30,32,33] using basis sets involving as many as 325 channels,[33] in which they found that surface corrugation rather than surface vibration plays a major role in broadening the rainbow features in the rotational state distribution.

B. Approximate Methods

As the discussion in the preceding section illustrates, the size of coupled-channel basis sets has increased over the years, due to improvements in computer capabilities and integration methods. Even so, the solution of the coupled-channel equations including internal and diffraction channels, not to mention phonon states of the solid, at typical experimental energies is still beyond reach. The CC approach also suffers from the disadvantage[13] that the potential must be perfectly periodic, allowing the expansion (1.3b); surfaces with imperfections, such as steps or adsorbates, are therefore excluded. Furthermore, numerical integration of the coupled equations provides little physical insight into the scattering process.[34] Due to these limitations, development of alternative methods for molecule-surface scattering calculations has generated considerable interest, leading to a host of approximate techniques which are quantal, semiclassical or classical in nature. The present section provides an overview of these techniques.

1. Quantum-Mechanical Approximations

Among the quantum-mechanical treatments, one of the most popular has been the sudden approximation, which was first introduced for molecule-surface scattering by Gerber *et al.*[35] The basic idea behind the sudden approximation is that for large collision energies, such that $E_{tot} \gg \hbar^2 G_{mn}^2/2M$ and $E_{tot} \gg \varepsilon_{vj}$, the elements of the $\underline{\underline{D}}^2$ matrix in equation (1.5) become independent of the channel quantum numbers. Thus the coupled-channel equations (1.4) can be decoupled by a coordinate transformation which diagonalizes the potential matrix (1.6). Applying the inverse transformation to the S matrix obtained from the decoupled equations yields the desired S matrix. This form of the sudden approximation is known as the matrix-diagonalization sudden (MDS).[35] Another version, called the coordinate-representation sudden (CRS), can be derived[35,36] by considering the coordinate representation of the S matrix, which is related to the probability for making a transition from the coordinates $(\vec{\rho},\vec{r})$ to the new set $(\vec{\rho}',\vec{r}')$. In a "sudden" collision, the coordinates do not change, so the S matrix is diagonal and given by $\underline{\underline{S}}(\vec{\rho},\vec{r}) = \exp[2i\eta(\vec{\rho},\vec{r})]$, where $\eta(\vec{\rho},\vec{r})$ is the WKB phase shift. The S-matrix element for the $i = (vjmkl) \rightarrow f = (v'j'm'k'l')$ transition is then found by transforming $\underline{\underline{S}}(\vec{\rho},\vec{r})$ to the quantum state representation:

$$S_{fi} = A^{-1} \int\int \exp(-i\vec{G}_{k'l'}\cdot\vec{\rho})\ \chi^{*}_{v'j'm'}(\vec{r}) \times S(\vec{\rho},\vec{r})\ \chi_{vjm}(\vec{r})\ \exp(iG_{kl}\cdot\vec{\rho})\ d\vec{r}\ d\vec{\rho}, \qquad (1.8)$$

where the $\vec{\rho}$ integration is over the surface unit cell and A is the area

of the unit cell. An intermediate approximation, the diffraction-sudden close-coupled-rotation (DSCCR) method, has also been formulated.[15] In this case only the diffraction states are uncoupled, leaving equations coupled in the internal quantum numbers v, j and m; these are solved for the $\vec{\rho}$-dependent S matrix $S_{v'j'm'\leftarrow vjm}(\vec{\rho})$, from which the full S matrix is found from an expression similar to equation (1.8), with $\chi_f^* S(\vec{\rho},\vec{r})\chi_i$ replaced by $S_{v'j'm'\leftarrow vjm}(\vec{\rho})$, and the $\vec{r}$ integration omitted. The advantages of these methods are clear. First, they greatly reduce the number of coupled channels and therefore the computational effort, particularly at higher energies where the CC method is intractable. Second, they offer significant physical insight into the scattering process. The CRS approximation in particular allows for analytical derivations of many properties of the S matrix, including scaling, factorization and sum rules.[15,35-37]

The sudden approximations have been employed frequently in the literature. Gerber *et al.*[35] used the CRS to establish several properties of the S matrix and associated transition probabilities, many of which were verified by their calculations using the MDS, as well as the CC calculations of Drolshagen *et al.*[17] Proctor, Kouri and Gerber[37] used the DSCCR to investigate Δm transitions in scattering from square and rectangular lattices, and found strong dependence of the $\Delta m \neq 0$ probability on the corrugation and on the ratio of diatom bond length to lattice parameter (which affects the effective corrugation). They also observed strong Δm selection rules for specular scattering, which they interpreted using the CRS. Motivated by the observation of a rotational (Δj) rainbow in NO/Ag(111) scattering,[19] Schinke[38] employed the CRS

(evaluated using the stationary-phase approximation) to investigate rainbow effects in molecule-surface collisions; Proctor and Kouri[39] used a similar method to analyze Δm rainbows. By treating diffraction, rotation and surface vibration in the sudden limit, Schinke and Gerber[40] derived a theory for the surface temperature dependence of rotational energy transfer in terms of a j-dependent Debye-Waller factor. (In neutron-surface scattering, the DW factor gives the attenuation of the zero-phonon diffraction spots due to the thermal motion of the lattice.) They found that the DW attenuation of the Δj transition probability decreases as the final j increases, and that individual Δj transitions are strongly dependent on surface temperature at low final j, though averaging over initial states washes out this latter effect in the rotational distributions. Tanaka and Sugano[41] showed that the bimodal rotational distribution in NO/Ag(111) collisions could be attributed to rainbows at low and high j, if the potential has an isotropic attractive well and an anisotropic repulsive wall; if the well is also anisotropic, at some value of the incident energy the anisotropies of the wall and well cancel, leaving the molecule with low rotation after the collision. This cancellation effect also appears in the CC and sudden calculations of Voges and Schinke.[34] In terms of assessing the numerical accuracy of the sudden approximation, comparisons with close-coupling calculations have shown that at high enough energies the sudden is quantitatively correct;[17] at lower energies it overestimates the high-order diffraction and rotational excitation, but still qualitatively reproduces trends seen in the exact results.[15,17,27,34]

Another approximate method, the multichannel distorted wave (MDW) perturbative approach, has been formulated by Whaley and Light.[42] This method is appropriate when the potential couples states for one degree of freedom more strongly than for any of the others. Whaley and Light treat the case for which rotation is strongly coupled, and diffraction is weakly coupled and treated perturbatively. The potential is split into a zero-order part $V^{(0)}$ (in this case, the $k = 1 = 0$ term of equation (1.3b), corresponding to a flat surface) and a perturbative part $V^{(p)}$ (the remaining terms in (1.3b)). Then equation (1.4) can be written

$$\left[\underline{\underline{1}} \frac{d^2}{dZ^2} + \underline{\underline{D}}^2 - \underline{\underline{V}}^{(0)}(Z) \right] \underline{\underline{f}}(Z) = \underline{\underline{V}}^{(p)}(Z)\, \underline{\underline{f}}(Z), \qquad (1.9)$$

where $\underline{\underline{V}}^{(0)}$ is the matrix whose only nonzero elements are those from equation (1.6) with $\Delta k = \Delta l = 0$ and $m' = m$, and where $\underline{\underline{V}}^{(p)} = \underline{\underline{V}} - \underline{\underline{V}}^{(0)}$, with $\underline{\underline{V}}$ given by (1.6). Let $\underline{\underline{f}}^{(0)}(Z)$ be the matrix of scattering amplitudes which satisfy the homogeneous ($\underline{\underline{V}}^{(p)} = \underline{\underline{0}}$) version of (1.9), and $\underline{\underline{S}}^{(0)}$ the corresponding S matrix. Then it can be shown[42] that the asymptotic form of the scattering amplitude matrix $\underline{\underline{f}}$ is

$$\underline{\underline{f}}(Z\to\infty) = \underline{\underline{f}}^{(0)}(Z\to\infty) + \frac{i}{2}\, \underline{\underline{Q}}\, \underline{\underline{S}}^{(0)\dagger} \times \int_0^\infty \underline{\underline{f}}^{(0)\dagger}(Z')\, \underline{\underline{V}}^{(p)}(Z')\, \underline{\underline{f}}(Z')\, dZ', \qquad (1.10)$$

where $\underline{\underline{Q}}$ is defined in equation (1.7c) and $\dagger$ denotes the adjoint matrix. Equation (1.10) is exact; the distorted wave approximation consists of replacing $\underline{\underline{f}}$ by $\underline{\underline{f}}^{(0)}$ in the integrand of (1.10). It is a true multichannel distorted wave method since the zero-order amplitudes are solutions of a

coupled-channel problem. In view of the boundary condition (1.7c), the MDW expression for the full S matrix is

$$\underline{\underline{S}} = \underline{\underline{S}}^{(0)} + \frac{i}{2}\,\underline{\underline{S}}^{(0)\dagger} \int_0^\infty \underline{\underline{f}}^{(0)\dagger}(Z')\,\underline{\underline{V}}^{(p)}(Z')\,\underline{\underline{f}}^{(0)}(Z')\,dZ'. \qquad (1.11)$$

Equation (1.11) can be evaluated by simultaneous propagation of the matrix $\underline{\underline{f}}(0)$ and the integral on the right-hand side.[42] Close-coupling calculations[12] were used to evaluate the accuracy of the MDW calculations[42] and the DSCCR results of Proctor *et al.*[37] for a model H_2/corrugated-surface system. It was found that the MDW and DSCCR are of comparable accuracy for non-specular peaks, while the MDW is less accurate for specular scattering at higher corrugations, where the diffraction is no longer perturbative. Another application of the distorted wave approach was developed by Gerber, Beard and Kouri[43] to investigate vibrational deactivation in molecule-surface collisions. Theirs was not a multichannel approach, since the equations for the zero-order solutions were uncoupled using the sudden approximation. Applying their model to collisions of H_2, D_2 and HD[43] and heavier diatoms[44] with rigid surfaces, they found deactivation probabilities as high as 10%, with the dominant mechanism being near-resonant V→R energy transfer.

The quantum-mechanical techniques described so far are time-independent methods, based on the TISE, equation (1.1). However, approaches based on the time-dependent Schrödinger equation (TDSE)

$$H_{tot}(\vec{R},\vec{r})\;\psi(\vec{R},\vec{r},t) = i\hbar\,\frac{\partial}{\partial t}\,\psi(\vec{R},\vec{r},t) \qquad (1.12)$$

have also been developed, most of which are based on the propagation of wavepackets. These wavepacket methods have recently been reviewed by Gerber *et al.*[9] One approach recently developed to investigate molecule-surface scattering is the close-coupling wavepacket (CCWP) technique of Mowrey and Kouri.[13,45] As its name implies, the CCWP formalism combines close-coupling and wavepacket propagation in the following way. The wavefunction ψ is expanded as

$$\psi^{v_0 j_0 m_0}(\vec{R},\vec{r},t) = \sum_{vjm} \chi_{vjm}(\vec{r})\, F^{v_0 j_0 m_0}_{vjm}(\vec{R},t) , \qquad (1.13)$$

where the coefficients F depend on $\vec{R}$ rather than Z because no expansion into $\vec{\rho}$-dependent diffraction states has been made. This permits application of the CCWP to scattering from imperfect lattices.[45] Inserting (1.13) into (1.12) yields a set of coupled equations written in matrix form as

$$i\hbar \frac{\partial}{\partial t} \underline{\underline{F}}^{v_0 j_0 m_0}(\vec{R},t) = \left[-\frac{\hbar^2}{2M} \underline{\underline{1}} \nabla^2_{\vec{R}} + \underline{\underline{\varepsilon}} + \underline{\underline{U}}(\vec{R}) \right] \underline{\underline{F}}^{v_0 j_0 m_0}(\vec{R},t), \quad (1.14)$$

where $\underline{\underline{F}}^{v_0 j_0 m_0}$ is a column vector, $\underline{\underline{\varepsilon}}$ is a diagonal matrix whose diagonal elements are the ε_{vj}, and the elements of the square matrix $\underline{\underline{U}}(\vec{R})$ are $U_{v'j'm'vjm} = \langle v'j'm'|V(\vec{R},\vec{r})|vjm\rangle$. Equation (1.14) is an initial-value problem, as opposed to equation (1.4), which is a two-point boundary-value problem. The initial condition at $t = t_0$ is $\underline{\underline{F}}^{v_0 j_0 m_0}(\vec{R},t_0)$. The wavepacket is evolved in time by expanding the propagator $\exp(-i\underline{\underline{H}}t/\hbar)$ in terms of Chebychev polynomials,[46] and evaluating the $\vec{R}$ derivatives in the Hamiltonian matrix $\underline{\underline{H}}$ (the bracketed quantity on the right-hand side

of (1.14)) using the fast-Fourier-transform algorithm.[47] When the wavepacket returns to the asymptotic region after the collision with the surface (at $t = t_f$), the column of the S matrix corresponding to the initial state $v=v_0$, $j=j_0$, $m=m_0$, $k=l=0$ is obtained by projecting out the contribution of each channel eigenfunction to the final wavefunction $\psi(\vec{R},\vec{r},t_f)$.[45] Calculations using the CCWP formalism have demonstrated that the method is just as accurate as a CC calculation.[13,45] However, because the computational effort scales as N_{int}^2, where N_{int} is the number of internal states in the basis, and because the S matrix can be extracted at several energies from a single propagation, the CCWP is computationally more efficient.[45] An example of the power of the method is a calculation for scattering of N_2 from a model corrugated surface, in which 13923 channels were included at energies of 10, 25 and 40 meV.[48]

2. Semiclassical Methods

In addition to the fully quantal methods discussed so far, several semiclassical approximations have been developed and applied to molecule-surface collisions. The semiclassical pertubation (SCP) method of Hubbard and Miller[49] is one example. In this approach, the gas-surface potential is divided into a zero-order term, $V_0(Z)$, plus a perturbation $V_p(\vec{R},\vec{r})$. This leads to a scattering phase shift of the form $\eta = \eta_0 + \eta_1(\vec{\rho}_0,\vec{r}_0)$, where η_0 is the WKB phase shift due to $V_0(Z)$, and η_1 is the time integral of the perturbation V_p:

$$\eta_1 = -\frac{1}{2}\int_{-\infty}^{\infty} dt\ V_p[\vec{R}_0(t),\vec{r}_0(t)]. \qquad (1.15)$$

In equation (1.15), $\vec{R}_0$ and $\vec{r}_0$ are trajectories determined by the zero-order potential V_0. The S matrix is found by suitable integrals of the classical S matrix, $\exp(2i\eta)$, over the angle variables conjugate to the classical actions corresponding to the quantum numbers; it can be shown[49] that the transition probabilities $P_{i\to f} = |S_{fi}|^2$ are then given by sums of products of Bessel functions, which are easily evaluated. Comparisons of SCP[49] with CC[11] and MDS[35] probabilities show that the SCP is both qualitatively and quantitatively accurate over a range of collision energies and corrugation strengths.

Other semiclassical models consist of treating one or more degrees of freedom quantum-mechanically, and using classical mechanics to describe the rest of the system. The degrees of freedom are coupled self-consistently in that the time propagation of the quantum part involves the time-dependent classical motion, while the classical motion is determined by an effective potential obtained from the wavefunction of the quantum part of the system via Ehrenfest's theorem. Billing developed a theory for molecule-surface scattering which treats the phonons of the solid as a set of coupled quantum oscillators and the gas species as a classical particle,[50] and extended the theory to include electron-hole pair excitations using an electron-gas model for the electrons of the solid.[51] Application of the model to scattering of CO from metal and insulator surfaces showed that the coupling to phonons is the dominant energy-loss channel and that electron-hole pair excitations can be neglected completely for insulators and qualitatively for metals.

Richard and DePristo[52] formulated the semiclassical stochastic trajectory (SST) approach, which handles the internal states of the molecule (vibration and rotation) using quantum mechanics and the center-of-mass and surface motion classically, the former via Hamilton's equations and the latter using the generalized Langevin equation (GLE) formalism of Tully[4] (discussed in detail below). The method was shown to be of qualitative and near quantitative accuracy,[52] and has been used to obtain state-to-state vibrational and rotational transition probabilities for H_2 scattering from flat[52,53] and corrugated surfaces,[54] and to study trapping and vibrational energy transfer in collisions of CO_2 with Pt(111)[55] and Ag(111).[56] The mean trajectory approximation (MTA) method of Jackson and Metiu[57] is similar to the SST approach, except that the center-of-mass motion is treated using wavepackets instead of classical trajectories, thus allowing for diffraction and other quantum effects involving the center of mass. The MTA is a generalization of the powerful wavepacket method for atom-surface scattering developed by Drolshagen and Heller.[58] For H_2/corrugated-surface scattering the MTA results are of comparable accuracy to those produced by the DSCCR and MDW techniques,[57] but differ from CC and CCWP results by as much as 29%.[45] A final example of the semiclassical methods is the self-consistent eikonal method (SCEM) of Rice *et al.*[59] The SCEM is derived by applying the "common eikonal" formalism of Micha[60] to the close-coupled equations for the system. This yields Hamilton's equations of motion for the center-of-mass trajectory, and Hamilton-like equations for the time-dependence of the real and imaginary parts of the quantum-state amplitudes $C_j(t) = X_j(t) + iY_j(t)$. The transition probability to state j at

any time t during the trajectory is given by $|C_j(t)|^2/2\hbar$. The method was compared to the close-coupled calculations of Smedley *et al.*[29] for rotational and fine-structure transitions in NO/Ag(111) collisions, and found to give good agreement at higher collision energies (0.83 eV); at lower energies (0.31 eV) the rotational excitation was overestimated. The calculations also indicated that the NO/Ag interaction is not impulsive, since the probability distribution evolves slowly throughout the trajectory.

3. Classical Methods

In addition to the quantal and semiclassical approaches, classical mechanics has been used to model the gas-surface scattering process. The classical techniques all involve integration of Hamilton's or Newton's equations of motion (EOM) for every degree of freedom in the model; the models differ in how many degrees of freedom in the surface are considered. The simplest models involve rigid surfaces which are either flat or corrugated; only the molecular degrees of freedom, which include translation, rotation and perhaps vibration, are treated explicitly. More complex approaches include motion of the atoms of the solid with varying levels of sophistication. Classical techniques are usually (but not always) applied to systems characterized by low-frequency motions (or, alternatively, small energy spacings), for which one expects quantum effects to be small. In some applications, correspondences are made between the classical trajectory results and quantum numbers for the system. This procedure is called the quasiclassical trajectory (QCT)

method. As opposed to the semiclassical methods, no part of the actual dynamics is treated with quantum mechanics in a QCT calculation.

Classical trajectory studies of molecule-surface scattering have sought both to elucidate general features of the energy transfer and dynamics and to model experimental results. In the former case, Hurst *et al.*[61] have shown that final rotational distributions resulting from impulsive collisions of a diatomic molecule with a hard repulsive wall will exhibit some or all of the following features: "rainbow" peaks at zero and high rotational energy, a "trapping cutoff" at the highest rotational energy when the interaction potential has an attractive well, and a perfectly polarized rotational distribution if the surface is flat. The rainbow features are due to extrema in the classical "excitation function" $j_f(\theta_i)$, that is, the final rotational angular momentum as a function of the initial orientation of the molecule; classically, such extrema cause singularities in the probability distribution. The zero-energy rainbow comes from a minimum in the excitation function, which means that for some range of initial orientations the net torque on the molecule due to the collision is zero. Rainbows at higher energies result from maxima in the excitation function, meaning that the collision with the surface imparts a maximum torque on the molecule. Two of these nonzero-energy rainbows may appear if the molecule is heteronuclear, since a different maximum torque is exerted depending on which end of the molecule strikes the surface; this fact is the basis for the "double-rainbow" interpretations of the NO/Ag(111) rotational distribution, which have been discussed earlier.[27,41] If the potential has an attractive part, the effective

impulsive collision energy is increased by the well depth. If the maximum torque is high enough, the molecule may temporarily become trapped in the well due to T→R energy transfer. This produces a trapping cutoff, that is, a degradation of the highest energy rainbow. Finally, polarization of the rotational distribution occurs in scattering from flat surfaces, since in this case the angular momentum component normal to the surface is conserved. Other work has elaborated on these results. Polanyi and Wolf[62] have shown that multiple (more than two) rainbows, due to multiple collisions, may occur for heteronuclear molecules if the offset of the center of mass from the midpoint of the internuclear axis is large enough; calculations by Elber and Gerber[63] suggest that multiple collisions may cause a double rainbow even for homonuclear molecules under certain conditions. Park and Bowman[64] have demonstrated that surface corrugation broadens the high-energy rainbow features, since the maximum torque is impact-site dependent. Corrugation also wipes out the zero-energy rainbow in impulsive collisions and destroys the perfect polarization of the rotational distribution at low but not high final j values, as discussed by Wolf, Collins and Mayne.[65] Inclusion of surface motion using simple models has indicated that this motion broadens and diminishes the rainbow features and broadens the trapping cutoff.[61,66,67] The impulsive collision limit just described pertains to scattering when the attractive part is isotropic (invariant with respect to initial orientation of the molecule), or when the collision energy is much greater than the well depth. Bowman and Park[68] have shown that when the collision energy is low and the well anisotropic, the well rather than the repulsive wall controls the dynamics. The

excitation functions in this case are more complicated than those for the impulsive collision regime, resulting in probability distributions which deviate from the impulsive behavior described above. For example, the anisotropies of the well and wall tend to cancel one another, resulting in rotational distributions peaked at low final j. This effect has also been observed before in quantal calculations,[34,41] as discussed previously.

Comparisons of classical calculations have been made to the results of both experiments and other theories. One of the first such applications was the QCT study by Ray and Bowman[69] of the diffractive and rotationally inelastic scattering of H_2 and D_2 from LiF(001) at low collision energy, using the rigid, corrugated surface model of Wolken.[11] The QCT results showed good qualitative agreement with the CC calculations of Wolken[11] and the experiments of Rowe and Ehrlich[70] for this system, which is somewhat surprising considering the low collision energy used and the large rotational spacing of H_2. Another set of QCT calculations on the H_2/LiF(001) system was performed by Saini *et al.*[71] using higher collision energies, for comparison with the sudden (CRS and MDS) results of Gerber *et al.*[35] Saini *et al.* found that the QCT transition probabilities conformed to most of the rules analytically derived using the CRS, but differed quantitatively from numerical MDS values. Drolshagen *et al.*[17] compared these QCT and MDS values with CC results. They found the QCT method to be more accurate than the MDS for low corrugation strengths at 0.5 eV collision energy; at higher collision energy (0.7 eV) the MDS became much better than the QCT results. Asada[72] developed a classical model for linear molecules striking flat, moving

surfaces, in which the molecular non-sphericity and the amplitude of surface vibration are treated perturbatively. Using it he was able to qualitatively reproduce his experimental finding[73] that the scattering lobe for molecules is shifted toward the surface tangent relative to that for atom-surface scattering, due to T→R energy transfer. Kubiak *et al.*[25] applied the hard-cube formalism of Nichols and Weare[74] to obtain insight into the dynamics of the NO/Ag(111) system. They were able to reproduce the collision-energy and surface-temperature dependence of the average final NO rotational energy with this model, but only by using values of the fitting parameters which implied trapping probabilities much greater than those determined experimentally. Recently, Coltrin and Kay[75] employed a QCT study of ammonia scattering from a flat, rigid gold surface to interpret an experimental investigation[76] of the NH_3/Au(111) system. The QCT results qualitatively reproduced many of the experimental observations and demonstrated the dynamical importance of long-range orienting forces in this system. The success of this treatment provided motivation for the QCT study of HCl/Au scattering presented in Chapters III and IV, and further details of the NH_3/Au results as they relate to the present work are discussed in Chapter IV.

To obtain greater insight into the role of the surface in the scattering process, and to reproduce experimental results more quantitatively, realistic modeling of the motion of the atoms of the solid must be employed. Classical mechanics has proven useful in this regard. One obvious way to account for motion of the solid is to integrate classical EOM for a number N_s of solid atoms using a molecular dynamics (MD)

procedure. Early work along these lines, which explored the scattering of rare gas atoms from surfaces, treated the solid as a small monolayer of independent[77a] or nearest-neighbor coupled[77b] harmonic oscillators, embedded in a lattice of atoms frozen at their equilibrium positions. Barker *et al.*[78] extended this model by integrating the EOM of a 5x5x5 slab of nearest-neighbor coupled harmonic oscillators sitting atop a frozen lattice, and using periodic boundary conditions in the X and Y directions to obtain the motion of atoms in adjacent slabs. It is apparent that MD can describe the gas-surface energy transfer and dynamics to any desired degree of accuracy, given a sufficiently large N_s, but such a "bigger hammer" approach clearly requires a significant computational effort. In addition, physical considerations have motivated the search for alternatives to the MD approach. In a gas-surface collision, only a few solid atoms interact strongly with the incoming molecule. These "primary" atoms are the ones of physical interest; the remainder of the solid is important chiefly for its influence on the primary atoms. Furthermore, most experiments focus on the final state of the gas molecule rather than on that of the solid. This means that an acceptable procedure is one which treats the solid approximately but accurately describes its effect on the molecule.

The most popular technique for inclusion of surface motion into a gas-surface scattering calculation is the generalized Langevin equation (GLE) approach developed by Adelman and Doll[79] and by Tully,[4] who called it the "stochastic trajectory method". Two assumptions are involved in formulating this approach: that, as mentioned above, the gas molecule interacts with only a few atoms (the "primary zone" or "P zone" atoms);

and that the forces between the P zone and the remainder of the solid (the "secondary" or "Q zone") are harmonic. Under these conditions, the EOM for the atoms in the solid can be written in matrix form as[80]

$$\ddot{\underline{u}}_P = \underline{\underline{F}}(\underline{x}_g, \underline{u}_P, \underline{u}_Q{=}0) - \underline{\underline{\Omega}}_{PQ}\, \underline{u}_Q \,, \tag{1.16}$$

$$\ddot{\underline{u}}_Q = -\underline{\underline{\Omega}}_{QP}\, \underline{u}_P - \underline{\underline{\Omega}}_{QQ}\, \underline{u}_Q \,, \tag{1.17}$$

where $\underline{u}_P$ and $\underline{u}_Q$ are column matrices containing the displacements of the P and Q zone atoms, respectively, from their equilibrium positions, $\underline{\underline{\Phi}}$ is the harmonic force constant matrix for the solid, and the P,Q subscripts denote partitions of $\underline{\underline{\Phi}}$ into the various submatrices that couple the P and Q zones. The column matrix $\underline{F}$ contains all the forces (divided by masses) on the primary atoms except those due to the secondary atom displacements. These include the forces among the P zone atoms (which may or may not be harmonic) and the forces due to the gas-surface interaction potential, which depend on the gas molecule coordinates $\underline{x}_g$, the primary atom displacements and possibly the equilibrium positions of the Q zone atoms. Equation (1.17) can be solved formally for $\underline{u}_Q$ in terms of $\underline{u}_P$, and the result substituted into (1.16) to obtain[4] the GLE's for the primary atoms:

$$\ddot{\underline{u}}_P(t) = \underline{\underline{F}}'(\underline{x}_g, \underline{u}_P, \underline{u}_Q{=}0) - \int_0^t \underline{\underline{\Lambda}}(t-t')\, \dot{\underline{u}}_P(t')\, dt' + \underline{R}(t). \tag{1.18}$$

In equation (1.18), the integral accounts for dissipation of energy from the P zone to the Q zone, while the (Gaussian) fluctuating force $\underline{R}(t)$

accounts for energy transfer from Q to P due thermal motion of the secondary atoms. $\underline{R}(t)$ and the "memory matrix" $\underline{\underline{\Lambda}}(t)$ are related by the "second fluctuation-dissipation theorem",[81] which ensures that the P zone remains at a constant temperature by requiring the net dissipation loss to balance the net thermal energy gain. The force matrix $\underline{F}'$ contains $\underline{F}$ from equation (1.16) plus some extra terms generated during the derivation of equation (1.18).

As it stands, equation (1.18) is exact. Although the essentially infinite number of solid atom EOM has been reduced to N_P equations, no less work is involved in solving (1.18) than (1.16) and (1.17), since the matrices $\underline{\underline{\Lambda}}$ and $\underline{R}$ contain all of the information contained in equation (1.17). The basic idea of the stochastic trajectory method is thus to employ approximate forms for these matrices, which result in considerable simplification of equation (1.18), while still adequately representing the effects of the Q zone. These forms contain adjustable parameters which may be fit to reproduce properties of the solid, such as phonon densities or velocity autocorrelation functions. For modeling metal surfaces, for which a typical P zone may contain $N_P = 4$ atoms, Tully[4] derived an approximation to (1.18) which included the Q-zone effects by coupling each primary atom to a "ghost atom" satisfying a Brownian oscillator equation of motion. In this case, only $2 \times N_P$ (= 8) surface atom EOM need be integrated along with those of the gas molecule. In ionic crystals the long-range ionic forces require larger P zones ($N_P = 32$ for LiF,[3] for example); this motivated Lucchese and Tully[82] to formulate a method in which the primary atoms along the P-Q interface are treated as Brownian oscillators.

The many applications of the stochastic trajectory method to atom-surface scattering have been reviewed by Tully.[80] Several studies of diatom-surface scattering have also been reported. Tully, Muhlhausen and Ruby[83] examined the scattering of N_2 from Ag(111). They found that the vibrational motion of the nitrogen molecule was only very weakly coupled to its translation and rotation and to the vibration of the solid, yielding vibrational deactivation probabilities of less than 5%. They also saw evidence of rainbow structure in the rotational distribution, though it was broadened considerably by the surface motion and corrugation. Lucchese and Tully[3] conducted extensive calculations on the NO/LiF system. Their objectives were to evaluate the experimental results of Zacharias *et al.*[84] for the NO vibrational deactivation, and to study the general features of vibrational energy transfer in molecule-surface collisions. With respect to the former, they found extremely low deactivation probabilities (less than 1%), which conflicted with the experimental result of essentially unit deactivation probability. (Subsequent experiments[85] found deactivation probabilities of 10%). The results of the vibrational energy transfer calculations will be discussed thoroughly in Chapter VI, where they are used as a standard for evaluating new calculations using the REOM technique.[2] Finally, Muhlhausen *et al.*[86] performed an extensive study of scattering and adsorption/desorption of NO from the (111) faces of Ag and Pt, for which abundant experimental data exist.[6,7] Using an interaction potential with a strongly orientation-dependent attractive part, they were able to reproduce all the experimental results for these two systems with qualitative and, in most instances, quantitative accuracy. It is interesting

that this study reproduced the bimodal NO/Ag(111) rotational state distribution using an anisotropic potential, and attributed the Boltzmann-like portion to averaging of many types of collisions rather than a low-energy rainbow. This differs from the interpretations discussed earlier[27,33,41] on both counts, illustrating that the dynamics for the NO/Ag(111) system have not yet been resolved unambiguously.

The final topic in this overview involves work on improvements on and alternatives to the stochastic trajectory approach. The methods discussed above[4,82] for reducing equation (1.18) to a smaller number of EOM, as well as that of Adelman and Doll,[79] invoke a Brownian oscillator approximation at some point. Diestler and Riley[87] proposed a simple modification to the Lucchese-Tully (LT) method[82] as well as other approaches not based on the Brownian approximation, and tested the old and new theories using various P-zone sizes against a (classically) numerically-exact gas-surface scattering data base which they had previously generated.[88] They found many of these approaches to be quite accurate, and recommended their bond-corrected Debye (modified LT) approximation (BCDA) as the best, considering both accuracy and ease of implementation. Recently, Riley, Coltrin and Diestler[5] presented an alternative to the GLE approach for simulation of the damping and thermal effects of the secondary atoms, based on Andersen's velocity-reset procedure for constant-temperature MD simulations.[89] The method of Riley *et al.* is discussed great detail in section B of Chapter V; here let it suffice to say that the approach involves integrating equation (1.16) for the P zone motion, periodically resetting the velocities of the atoms according to an algorithm which preserves a canonical velocity distribution

and which incorporates damping and thermal effects. As shown in reference 88 and in Chapter V, this "partial velocity reset" reduces to the LT procedure in the limit that the time interval between velocity resets goes to zero. The method is easy to apply, compares well with the LT method for all reset intervals and is not restricted to harmonic lattices.

The accuracy of approaches involving a reduced number of surface atom equations of motion in a gas-surface scattering calculation has prompted inquiries into whether accurate results might be obtained by a method in which the entire surface is treated as the Q zone and only the gas molecule EOM are integrated explicitly. Such an approach, based on Tully's ghost-atom approximation, has been formulated recently by Zeiri.[90] He showed that his "effective equations of motion" (EEM) gave good quantitative agreement with the results of the ghost-atom method for a one-dimensional model of Ar and Xe/Ag scattering. Diestler and Riley[2] derived reduced equations of motion (REOM) based upon an adiabatic approximation for the surface atoms' response to the presence of the gas molecule, assuming the solid to be at T = 0 K. They tested the model against the data base of numerically-exact atom scattering results, and found it to be reliable for sufficiently large values of the ratio of gas to solid atom mass and of collision energy to potential well depth. In section A of Chapter V the derivation of the REOM is presented in detail. The method is applied in the present work to the scattering of NO from LiF(001), with nonzero surface temperature included via the velocity-reset procedure; In Chapter VI the results are presented and compared with those of Lucchese and Tully.[3]

CHAPTER II

IMPLEMENTATION OF THE QUASICLASSICAL TRAJECTORY METHOD

This chapter explains how the quasiclassical trajectory method was employed in this work to compute and analyze trajectories for gas diatoms colliding with a rigid surface. In particular, information applying to both the HCl/Au and NO/LiF calculations is presented here. The NO/LiF studies involve modifications to this general framework, related to the implementation of the REOM formalism using the velocity-reset procedure. Details concerning those modifications are given in Chapter V. The discussion in Chapter II is organized as follows. Section A describes the coordinate system and the canonical variables in terms of which the Hamiltonian is expressed, and summarizes the procedure for doing the trajectory calculations. In section B, specifics related to selecting initial conditions for a trajectory are presented. Section C is devoted to the numerical integration of Hamilton's equations, including a discussion of the rigid-rotor constraint. Finally, section D concludes by outlining the methods used to analyze results from individual trajectories and from sets of trajectories.

A. Coordinate System and Canonical Variables

The method of quasiclassical trajectories involves integrating the appropriate classical equations of motion for the system in question, given some randomly or systematically selected set of initial conditions. The equations of motion used here are Hamilton's equations[91a]:

$$\dot{q}_i = \frac{\partial H}{\partial p_i} , \qquad \dot{p}_i = -\frac{\partial H}{\partial q_i} , \tag{2.1}$$

where the $\{q_i\}$ are the generalized coordinates of the system, the $\{p_i\}$ their conjugate momenta, and H is the Hamiltonian (total energy function) of the system, expressed as a function of the $\{q_i\}$ and $\{p_i\}$. A dot over a variable denotes the total derivative of that variable with respect to time. The set of variables $\{q_i,p_i\}$ are called the canonical variables of the system. In order to proceed, the coordinate system must be specified.

For these calculations, a Cartesian coordinate system (the "laboratory frame") is chosen such that the Z axis is normal to the surface and the X and Y axes lie in the plane of the surface; the solid occupies the half-space $Z \leq 0$. For a diatomic molecule moving above a rigid surface, there are six Cartesian coordinates (the laboratory X, Y and Z coordinates for each atom) and six Cartesian components of momentum conjugate to them (P_x, P_y and P_z on each atom). Choosing these as the canonical variables, the Hamiltonian is given by

$$H = \frac{P_{1x}^2 + P_{1y}^2 + P_{1z}^2}{2m_1} + \frac{P_{2x}^2 + P_{2y}^2 + P_{2z}^2}{2m_2} + V_{tot}(X_1,Y_1,Z_1,X_2,Y_2,Z_2), \quad (2.2)$$

in which m_i is the mass of atom i and V_{tot} is the total potential energy function for the system. In these calculations V is always a function of the coordinates only. If $\vec{R}_i$ and $\vec{P}_i$ represent the position vector (X_i,Y_i,Z_i) and momentum vector (P_{ix},P_{iy},P_{iz}), respectively, of atom i in the laboratory frame, then equation (2.2) may be written more compactly in vector notation as

$$H = \frac{P_1^2}{2m_1} + \frac{P_2^2}{2m_2} + V_{tot}(\vec{R}_1,\vec{R}_2), \quad (2.3)$$

where P_i is the magnitude of $\vec{P}_i$.

The quantities of interest here are the translational, vibrational and rotational energies or quantum numbers of the diatom (both before and after the collision with the surface); these various degrees of freedom are not easily separated from each other when the Hamiltonian is expressed as above. Thus it is convenient to form from the set of atomic coordinates and momenta a new set involving center-of-mass and relative Cartesian coordinates and momenta. In vector notation this transformation is given by

$$\vec{R}_{cm} = \eta_1 \vec{R}_1 + \eta_2 \vec{R}_2, \quad (2.4a)$$

$$\vec{r} = \vec{R}_2 - \vec{R}_1, \quad (2.4b)$$

$$\vec{P}_{cm} = \vec{P}_1 + \vec{P}_2, \tag{2.4c}$$

$$\vec{p} = \gamma_1 \vec{P}_1 + \gamma_2 \vec{P}_2, \tag{2.4d}$$

where the "cm" subscripts denote center-of-mass quantities, and lower-case unsubscripted letters represent relative quantities. The vectors $\vec{R}_{cm}$ and $\vec{P}_{cm}$ give the position and momentum vectors of the center of mass of the gas molecule in the laboratory frame. while $\vec{r}$ and $\vec{p}$ give the relative position and momentum with respect to a coordinate system whose axes are parallel to those of the lab frame. The mass factors η_i and γ_i are defined by

$$\eta_1 = \frac{m_1}{M}, \qquad \eta_2 = \frac{m_2}{M}, \tag{2.5a}$$

$$\gamma_1 = \frac{-m_2}{M}, \qquad \gamma_2 = \frac{m_1}{M}, \tag{2.5b}$$

where $M = m_1 + m_2$. The inverse transformation, which gives the lab frame position and momentum vectors of atom i in terms of the center-of-mass and relative quantities, is

$$\vec{R}_i = \vec{R}_{cm} + \gamma_i \vec{r}, \tag{2.6a}$$

$$\vec{P}_i = \eta_i \vec{P}_{cm} + (-1)^i \vec{p}. \tag{2.6b}$$

The following two paragraphs show how transforming to center-of-mass and relative coordinates separates the various degrees of freedom.

If one subjects equation (2.3) to the transformation given by equations (2.4), the Hamiltonian in the new canonical variables is

$$H = \frac{P_{cm}^2}{2M} + \frac{p^2}{2\mu} + V_{tot}(\vec{R}_{cm},\vec{r}), \qquad (2.7)$$

where P_{cm} and p are the magnitudes of $\vec{P}_{cm}$ and $\vec{p}$, respectively, and $\mu = m_1 m_2 / M$ is the reduced mass of the diatom. The total potential V_{tot} is the sum of the internal (vibrational) potential of the diatom and the interaction potential of the diatom with the surface:

$$V_{tot}(\vec{R}_{cm},\vec{r}) = V_{int}(r) + V_{gs}(\vec{R}_{cm},\vec{r}). \qquad (2.8)$$

It is assumed that V_{int} depends only on the internuclear separation r, which is the magnitude of $\vec{r}$. When the diatom is far from the surface, V_{gs} goes to zero and the Hamiltonian of equation (2.7) reduces to that of an isolated diatom moving through space:

$$H_{iso} = \frac{P_{cm}^2}{2M} + \frac{p^2}{2\mu} + V_{int}(r) \qquad (2.7')$$

The first term on the right hand side of equation (2.7′) is the translational energy of the diatom, E_T; the remaining terms contain the internal (vibrational plus rotational) energy of the molecule, E_{int}. Changing from atom to center-of-mass/relative coordinates thus has automatically separated the translational energy from the internal energies; the vibrational and rotational energies can be found by expressing p^2 in

terms of the vibrational and angular momenta.

The vibrational momentum $\vec{p}_r$ is the component of the relative momentum $\vec{p}$ along the direction of $\vec{r}$. Using the definition of the scalar product of two vectors one can easily find an expression for p_r, the magnitude of the vibrational momentum:

$$p_r = p \cos \alpha = \frac{\vec{r} \cdot \vec{p}}{r} = \frac{x\, p_x + y\, p_y + z\, p_z}{r}, \qquad (2.9)$$

where α is the angle between $\vec{r}$ and $\vec{p}$. The angular momentum is defined as $\vec{j} = \vec{r} \times \vec{p}$, the vector product of $\vec{r}$ and $\vec{p}$, which gives the familiar expressions for the x, y and z components of $\vec{j}$:

$$j_x = y\, p_z - z\, p_y, \qquad (2.10a)$$

$$j_y = z\, p_x - x\, p_z, \qquad (2.10b)$$

$$j_z = x\, p_y - y\, p_x. \qquad (2.10c)$$

Using equations (2.9) and (2.10) and a little bit of algebra, one can show that the following equality holds:

$$\frac{p^2}{2\mu} = \frac{p_x^2 + p_y^2 + p_z^2}{2\mu} = \frac{p_r^2}{2\mu} + \frac{j^2}{2\mu r^2}, \qquad (2.11)$$

where $j^2 = j_x^2 + j_y^2 + j_z^2$ is the square of the magnitude of the angular momentum. The first term on the right hand side of equation (2.11) is the vibrational kinetic energy; adding to it $V_{int}(r)$ gives the classical vibrational energy E_V of the molecule. The second term on the right hand

side is the classical rotational energy E_R.

Having thus specified the coordinate system and the canonical variables, the procedure for implementing the quasiclassical trajectory method can be outlined. To run a single trajectory, one starts with the diatom very far from the surface, at which point initial values of P_{cm}, p_r, j and r for the isolated molecule are selected, given initial values of the translational energy and the vibrational and rotational quantum numbers. From these one determines the initial values of the canonical coordinates $(X_{cm}, Y_{cm}, Z_{cm}, x, y, z)$ and momenta $(P_{cm,x}, P_{cm,y}, P_{cm,z}, p_x, p_y, p_z)$. Then equations (2.1) are numerically integrated from this starting point, using the Hamiltonian given by equation (2.7), until the collision with the surface is over and the molecule is again far from the surface (or until some time limit has been reached, since in some trajectories the diatom may stick to the surface). Finally, at the end of the trajectory the final vibrational and rotational quantum numbers v_f and J_f, as well as the final translational, vibrational and rotational energies E_T^f, E_V^f and E_R^f, are extracted from the final values of the canonical variables. To obtain useful information for comparison with experiment, one runs sets of trajectories using the above procedure, with each set characterized by fixed values of the experimentally-controlled parameters, such as initial translational energy and quantum numbers. The individual trajectories differ in their values of the uncontrollable parameters, such as initial orientation and vibrational phase; at the end of the set the results can be averaged over the uncontrolled variables. In the studies reported here, this averaging is done via the Monte Carlo technique,[92] which utilizes random selection of

the quantities to be averaged. The following sections explain each of the above steps in greater detail.

B. Quasiclassical Correspondence and Selection of Initial Conditions

The quasiclassical trajectory method is so named because it attempts to relate the results of a classical-mechanical calculation to their quantum-mechanical analogues. This is done by specifying equations of correspondence between the classical action variables and the quantum numbers for the system. For a diatomic molecule the action variables are the angular momentum j (defined above) and the vibrational action N, defined by[91b]

$$N = \int p_r \, dr, \tag{2.12}$$

where the integral is over one period of the vibrational motion. These correspond to the angular momentum and vibrational quantum numbers J and v, respectively. The equations of correspondence used in this work are

$$j = \sqrt{J(J+1) - \Omega^2}, \tag{2.13a}$$

$$N = (v + \tfrac{1}{2})\,\hbar, \tag{2.13b}$$

in which Ω is the electronic orbital angular momentum quantum number for the electronic state of the diatom, and $\hbar$ is Planck's constant. It is assumed here that all trajectories are adiabatic (a single potential energy surface applies throughout); in this case Ω will be a constant

for all trajectories. Most treatments of the quasiclassical correspondence for the angular momentum omit the Ω^2 term from equation (2.13a). This is certainly appropriate for molecules in $^1\Sigma$ electronic states, such as HCl in its ground state, since for these states Ω is zero. Equation (2.13a) arises from the formula for the rotational energy of a Hund's case (a) diatomic molecule,[93a] of which NO in its ground state is an example. The facts that such molecules do not have J less than Ω and have half-integral J if Ω is half-integral are automatically accounted for when (2.13a) is used.

Given the quasiclassical correspondence, one can obtain the initial values of the relative coordinates and momenta for a vibrating, rotating diatomic molecule from the quantum numbers v and J. To do this, equations (2.13) are employed to convert the quantum numbers to the corresponding values of the classical total (internal) energy and rotational angular momentum, which are conserved quantities for an isolated diatomic molecule. The relative coordinates and momenta are then found by specifying the isolated molecule's vibrational phase and orientation with respect to the laboratory coordinate system. The following paragraphs describe this procedure in detail.

Consider an isolated diatomic molecule in the rovibrational state (v,J), in a coordinate system (the "isolated frame") chosen so that the molecular motion is in the xy plane. The classical angular momentum j corresponding to the quantum number J is given immediately by equation (2.13a) while the classical total (internal) energy E_{int} may be estimated from the spectroscopic expression[93b]

$$E_{int}^{est} = (v + \tfrac{1}{2})\,\omega_e - (v + \tfrac{1}{2})^2\,\omega_e x_e + B_v\,[J(J+1) - \Omega^2] - D_e\,J^2(J+1)^2, \qquad (2.14)$$

in which $B_v = B_e - \alpha_e(v + \tfrac{1}{2})$ and ω_e, $\omega_e x_e$, B_e, α_e and D_e are the spectroscopic constants. The vibrational quantum number v_{calc} corresponding to any particular values of E_{int} and j may be calculated from equations (2.12) and (2.13b), as explained in the next paragraph; since equation (2.14) is not exact, the value of v_{calc} computed using E_{int}^{est} will not equal v. To find the correct total energy corresponding to v, an iterative procedure developed by Coltrin *et. al.*[94] is used. This involves modifying E_{int}^{est} until $v_{calc} = v$.

To find v_{calc} from (2.13b), given values of j and E_{int}, one must solve equation (2.12) for the vibrational action N. A convenient way to do this is to change the integration variable in (2.12) from r to t:

$$N = \int p_r\,dr = \int_0^\tau p_r \frac{dr}{dt}\,dt = \frac{1}{\mu}\int_0^\tau p_r^2\,dt \qquad (2.15)$$

where τ is the vibrational period. Equation (2.15) is equivalent to integrating the ordinary differential equation

$$\dot{N} = \frac{1}{\mu}\,p_r^2, \qquad (2.15')$$

with initial condition N = 0 at t = 0, over a cycle of the vibrational motion. This is accomplished by integrating equation (2.15′), using p_r given by (2.9), while the equations of motion (2.1) are integrated from

one vibrational turning point (where p_r equals zero) to the other, using the internal Hamiltonian

$$H_{int} = \frac{p^2}{2\mu} + V_{int}(r). \qquad (2.16)$$

Equation (2.16) differs from equation (7′) only in the absence of the center-of-mass term. The turning point from which the integration begins is found as follows. At an instant when the molecular axis lies along the x axis and the internuclear separation r is equal to its equilibrium value r_e, the relative coordinates and momenta in the isolated coordinate system have the values $(x,y,z) = (r_e,0,0)$ and $(p_x,p_y,p_z) = (p_r^e, j/r_e, 0)$, where $p_r^e = p_r(r = r_e)$ is obtained from (2.16) and (2.11) using the given j and E_{int}. From these initial coordinates and momenta, equations (2.1) are integrated until $p_r = 0$. Then the integration of (2.15′) begins. The time required to integrate between turning points is half the vibrational period and the result of integrating equation (2.15′) this far is N/2; since the integration of the second half of the cycle will be identical to that for the first half, it can be eliminated and the period and action found instead by multiplying by two. Having thus determined the value of N, the vibrational quantum number v_{calc} corresponding to the E_{int} and j of interest can be obtained from equation (2.13b).

As mentioned above, the value of E_{int}^{est} from (2.14) does not yield v_{calc} equal to the initial quantum number v. To obtain the proper value of E_{int}, the procedure given in the preceding paragraph is iterated,

modifying the estimate of E_{int} each time, until v_{calc} matches v to the desired accuracy. The algorithm for modifying the energy is

$$E_2 = E_1 + (v - v_1) \frac{\partial E}{\partial v}, \tag{2.17a}$$

$$E_{i+1} = E_i + (v - v_i) \left[\frac{\Delta E}{\Delta v}\right]_i, \tag{2.17b}$$

where E_1, the first guess at the energy, is given by E_{int}^{est} and v_1 is the corresponding v_{calc}. The slopes in (2.17) are

$$\frac{\partial E}{\partial v} = \omega_e - 2 (v + \tfrac{1}{2}) \omega_e x_e + \alpha_e [J(J + 1) - \Omega^2], \tag{2.18a}$$

$$\left[\frac{\Delta E}{\Delta v}\right]_i = \frac{E_i - E_{i-1}}{v_i - v_{i-1}}. \tag{2.18b}$$

Equation (2.18a) is the partial derivative with respect to v of equation (2.14). Typically four to six iterations are sufficient to match v to six decimal places.

To this point the values of E_{int} and j corresponding to the quantum numbers have been determined. However, the orienting procedure described in the next two paragraphs requires values for r and p_r along with j. Since, for a given E_{int} and j, the values of r and p_r vary depending on where the molecule is in its vibrational cycle (that is, on its vibrational phase), the next step in initializing the relative coordinates and momenta is to choose the vibrational phase ϕ_{vib} and find the associated values of r and p_r. This is done by integrating the equations of motion (2.1), using H_{int}, for a time $t_p = (\phi_{vib}/2\pi)\, \tau$, starting from one

of the turning points (at which the molecule with the correct total energy was left at the end of the iteration procedure above). The value of ϕ_{vib} is selected either randomly or systematically. At the end of the integration, r and p_r are calculated.

Given j, p_r and r at the start of the trajectory, the initial values of the relative variables are obtained by orienting the relative Cartesian coordinate system of the isolated molecule with respect to the "laboratory" relative Cartesian coordinate system, whose axes are parallel to those of the laboratory frame. The orientation is described by the Euler angles[91c] θ, ϕ and ψ, which are selected either randomly or systematically. In what follows, primed coordinates refer to the isolated frame and unprimed ones to the laboratory frame. The isolated coordinate system is defined, as above, such that the molecular motion is in the x′y′ plane. Assuming the molecular axis lies along the x′ axis, the values of the coordinates and momenta in this system are $(x',y',z') = (r,0,0)$ and $(p_{x'},p_{y'},p_{z'}) = (p_r,j/r,0)$.

The transformation from the lab to the isolated coordinates is performed via a series of rotations specified by the Euler angles. There are various conventions for choosing these angles;[91c] these calculations employ the "x convention" to define the transformation. In this scheme, the isolated coordinate axes are oriented via successive counterclockwise rotations by an angle ϕ around the z axis, by θ around the x′ axis and by ψ around the z′ axis. The result of this operation is shown in Figure 1. The intersection of the xy and x′y′ planes is called the "line of nodes";[91c] ϕ is the angle between the x axis and the line of nodes, ψ the angle between the line of nodes and the x′ axis, and θ the angle

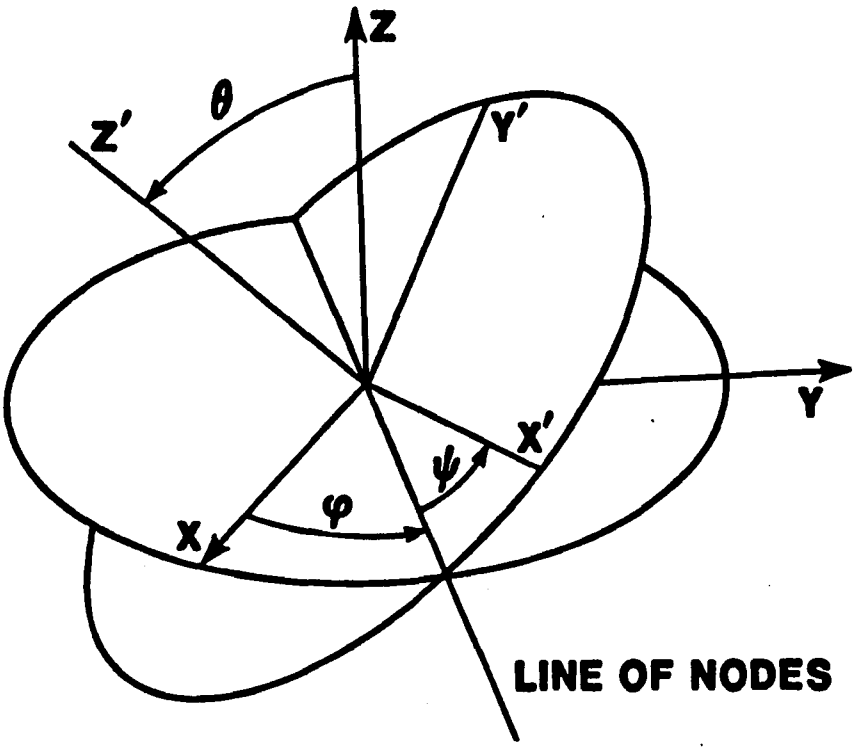

Figure 1. Euler angle transformation between the isolated and laboratory coordinate systems. The diatom lies along the x′ axis.

between the z and z′ axes. The ranges of the Euler angles are thus $0 \leq \phi \leq 2\pi$, $0 \leq \theta \leq \pi$ and $0 \leq \psi \leq 2\pi$. The transformation matrix $\underline{\underline{A}}$ for obtaining the isolated coordinates from the lab coordinates, and its inverse $\underline{\underline{T}} = \underline{\underline{A}}^{-1} = \underline{\underline{A}}^{T}$ for finding the lab coordinates from the isolated ones, have been worked out;[91c] the latter of these is needed here since the isolated coordinates have been specified and the lab coordinates are sought. The matrix is

$$\underline{\underline{T}} = \begin{bmatrix} \cos\psi\cos\phi-\cos\theta\sin\phi\sin\psi & -\sin\psi\cos\phi-\cos\theta\sin\phi\cos\psi & \sin\theta\sin\phi \\ \cos\psi\sin\phi+\cos\theta\cos\phi\sin\psi & -\sin\psi\sin\phi+\cos\theta\cos\phi\cos\psi & -\sin\theta\cos\phi \\ \sin\theta\sin\psi & \sin\theta\cos\psi & \cos\theta \end{bmatrix} \quad (2.19)$$

and the transformation given by

$$\begin{bmatrix} x \\ y \\ z \end{bmatrix} = \underline{\underline{T}} \begin{bmatrix} x' \\ y' \\ z' \end{bmatrix} \tag{2.20}$$

with a similar expression for the momenta. Applying equation (2.20) to the values of the isolated coordinates and momenta from the preceding paragraph thus specifies the initial values of the relative coordinates and momenta in the laboratory frame.

This completes the determination of the initial values of the relative corrdinates and momenta when the diatom is a vibrating rotor.In the case that the diatom is a rigid rotor, the above procedure can be greatly simplified. As before, the classical angular momentum j is calculated using equation (2.13a). However, since the molecule cannot vibrate, one simply sets the vibrational momentum p_r equal to zero and the internuclear separation equal to r_e before proceeding with the orientation procedure described in the preceding two paragraphs.

Determining the initial values of the canonical variables for the center-of-mass motion of a trajectory is straightforward. The vectors $\vec{R}_{cm}$ and $\vec{P}_{cm}$ describe the center-of mass motion in the laboratory frame. Initial values of the components of $\vec{R}_{cm}$ are selected as follows. In the HCl/Au calculations, which employ a flat-surface model, the coordinates X_{cm} and Y_{cm} parallel to the surface are (arbitrarily) set to zero; for the rigid-lattice model used in the NO/LiF work, X_{cm} and Y_{cm} are randomly or systematically assigned values X_{in} and Y_{in} within a surface

unit cell. In either case, the height Z_{cm} of the center of mass above the surface is set to some large positive value Z_{in} at which the gas-surface interaction potential V_{gs} is negligible. The initial center-of-mass momenta can be found given values of the initial translational energy and incidence angles. If θ_i and Φ_i are the polar and azimuthal incidence angles, respectively, then the following expressions can be used to obtain the momenta:

$$P^{in}_{cm,x} = P^{in}_{cm} \sin\theta \cos\Phi , \tag{2.21a}$$

$$P^{in}_{cm,y} = P^{in}_{cm} \sin\theta \sin\Phi , \tag{2.21b}$$

$$P^{in}_{cm,z} = - P^{in}_{cm} \cos\theta , \tag{2.21c}$$

where $P_{cm} = (2ME_T)^{1/2}$ and E_T is the initial translational energy. The negative sign in (2.21c) is needed so that the molecule initially moves downward toward the surface. In all the calculations done here the value of Φ_i is chosen to be zero.

In summary, then, to establish the initial values of the canonical coordinates x, y, z, X_{cm}, Y_{cm} and Z_{cm}, and momenta p_x, p_y, p_z, $P_{cm,x}$, $P_{cm,y}$ and $P_{cm,z}$ for a particular trajectory, the following quantities must be supplied: the vibrational and rotational quantum numbers v and J; the vibrational phase ϕ_{vib}, for trajectories involving vibration; the Euler angles θ, ϕ and ψ; locations X_{in} and Y_{in} of the center of mass above the surface unit cell (for calculations not involving a flat-surface model); the initial height Z_{in} of the center of mass above the surface; the initial translational energy E_T; and the incidence angle θ_i.

Some of these (v, Z_{in}, and E_T) are input to the computer program which performs the trajectory calculations; others (ϕ_{vib}, θ, ϕ, ψ, X_{cm} and Y_{cm}) are calculated as required by the trajectory code; the rest (J and θ_i) are either input or calculated, depending on the trajectory. For trajectories requiring random sampling of J or θ_i from appropriate distributions, the values are selected by the program; when specific values of J or θ_i are needed, they are input to the program. All of the parameters generated by the trajectory code are selected either systematically or randomly. Systematic sampling is done using coded control loops, whose limits and increments are given as input to the program. Random sampling, for the purposes of Monte Carlo averaging, employs random numbers ξ_i, chosen uniformly from the standard rectangular distribution[92a] (that is, from the interval $0 \leq \xi_i \leq 1$), in various algorithms to calculate the desired quantities. These algorithms are discusssed below.

For vibrating-rotor trajectories, the vibrational phase ϕ_{vib} is needed. Since the phase is equally likely to have any value within its range (0 to 2π), it is simply calculated as

$$\phi_{vib} = 2\pi\xi_p \tag{2.22}$$

where ξ_p is a random number. This means that the integration time to find r and p_r as described above is $t_p = \xi_p \tau$.

For trajectories using a lattice model for the surface, X_{in} and Y_{in} are required. For the square lattice used in the NO/LiF calculations, these must lie within the square formed by the four surface atoms at the

center of the lattice. If the origin lies at the center of this square, and if the sides of the square are of length ℓ, then

$$X_{in} = \ell\ (\xi_x - \tfrac{1}{2}), \tag{2.23a}$$

$$Y_{in} = \ell\ (\xi_y - \tfrac{1}{2}), \tag{2.23b}$$

where ξ_x and ξ_y are random numbers.

The Euler angles are selected using the random numbers ξ_ϕ, ξ_θ and ξ_ψ. Since ϕ and ψ are both azimuthal angles, any value within their ranges is equally likely. Thus these angles are simply found from the equations

$$\phi = 2\pi\xi_\phi, \tag{2.24a}$$

$$\psi = 2\pi\xi_\psi. \tag{2.24b}$$

However, the polar angle θ has a $\sin\theta$ weighting, and must be treated differently. Since the portion of a sphere having polar angles between zero and θ contains a fraction $f_\theta = \frac{1}{2}\ (1 - \cos\theta)$ of the total surface area of the sphere, the correct way to randomly select θ is via the expression

$$\theta = \cos^{-1}\ (1 - 2\ \xi_\theta). \tag{2.24c}$$

In the few instances when Monte Carlo selection of the initial rotational quantum number J or the incidence angle θ_i from appropriate distributions is required, the method of cumulative probabilities is used.[95] This involves constructing for each of these quantities a cumulative probability distribution, that is, a distribution $P_\alpha(\alpha')$ which gives the probability that quantity α has a value less than or equal to α'. Having such distributions, the value of the desired quantity α is chosen to be that α' for which $P_\alpha(\alpha')$ first becomes greater than or equal to the random number ξ_α (for discrete distributions), or for which $P_\alpha(\alpha') = \xi_\alpha$ (for continuous distributions). The cumulative distribution is built from the appropriate probability distribution for the individual values of α.

The probability distribution used in this work to construct the (discrete) cumulative distribution for J is either an experimentally-determined distribution of rotational states (in a molecular beam, for example), or a Boltzmann distribution at a rotational temperature T_{rot}. The latter is given by

$$P_{Boltz}(J'') = \frac{W_I(J'')\ (2J''+1)\ \exp[-\beta\ E_{J''}]}{\sum_{J''} W_I(J'')\ (2J''+1)\ \exp[-\beta\ E_{J''}]}\ , \qquad (2.25)$$

in which $\beta = (kT_{rot})^{-1}$, k is Boltzmann's constant, and $E_{J''}$ is the rotational energy of state J'', given by the last two terms on the right hand side of equation (2.14). The sum in the denominator of (2.25) runs over all possible values of J''. The weight factors $W_I(J'')$, in which I is the nuclear spin quantum number, are equal to unity for all J'' for a

heteronuclear diatomic; their values for a homonuclear diatomic depend on the parity of J'', the value of I and the symmetry of the electronic state wavefunction with respect to nuclear interchange.[96] The cumulative probability distribution corresponding to equation (2.25) is

$$P_J(J') = \sum_{J''=0}^{J'} P_{Boltz}(J''). \tag{2.26}$$

The value of J corresponding to the random number ξ_J is J' such that $P_J(J'-1) \leq \xi_J \leq P_J(J')$.

Random selection of the incidence angle θ_i is based on a $\cos\theta$ probability distribution, that is, $P(\theta'') = \cos(\theta'')$; this is the appropriate distribution for a gas in thermal equilibrium with a surface.[97a] The (continuous) cumulative distribution corresponding to $P(\theta'')$ is

$$P_\theta(\theta') = \int_0^{\theta'} P(\theta'')\, d\theta'' = \sin(\theta'). \tag{2.27}$$

From equation (2.27) the value of θ_i corresponding to the random number ξ_θ is evidently $\theta' = \sin^{-1}(\xi_\theta)$.

C. Integration of Trajectories

Having established the initial values of the canonical variables using the procedures outlined in section B, Hamilton's equations may be integrated, using the Hamiltonian H of equation (2.7). Given this form for H, it is apparent that derivatives of H with respect to momenta only

involve the first two terms on the right hand side of equation (2.7), while derivatives with respect to coordinates only act on the potential energy V_{tot}. Thus equations (2.1) simplify to

$$\dot{q}_i = \frac{p_i}{m_i}, \qquad \dot{p}_i = -\frac{\partial V}{\partial q_i} \tag{2.28}$$

where $m_i = M$ if q_i is a center-of-mass coordinate and $m_i = \mu$ if q_i is a relative coordinate.

Equations (2.1) and (2.28) are appropriate for the case of a vibrating, rotating molecule. For trajectories run with the diatom constrained to be a rigid rotor, these must be modified to include the constraint. For constraints which can be expressed mathematically as $F(\{q_i\},\{p_i\}) = 0$, Hamilton's equations become[98]

$$\dot{q}_i = \frac{\partial H}{\partial p_i} + \lambda \frac{\partial F}{\partial p_i}, \qquad \dot{p}_i = -\frac{\partial H}{\partial q_i} - \lambda \frac{\partial F}{\partial q_i} \tag{2.1'}$$

where λ is a Lagrange undetermined multiplier. In the case of a rigid rotor, the constraint equation is

$$F = x^2 + y^2 + z^2 - r^2 = 0, \tag{2.29}$$

in which the internuclear distance r is a constant, usually chosen as the equilibrium separation r_e. Clearly, the equations for the $\dot{q}_i$ are identical to those for the unconstrained case, since $\partial F/\partial p_i = 0$; the same is true of the equations for the time derivatives of the center-of-mass momenta. The time derivatives of the relative momenta become

$$\dot{p}_\zeta = -\frac{\partial H}{\partial \zeta} - 2\lambda\zeta = -\frac{\partial V}{\partial \zeta} - 2\lambda\zeta, \qquad (2.30)$$

where ζ = x, y or z. The rightmost equality in equation (2.30) follows since the only part of H dependent on the coordinates is V. The value of λ can be found as follows. Multiplying the second derivative with respect to time of equation (2.29) by the reduced mass μ, one obtains

$$\frac{p^2}{2\mu} + x\dot{p}_x + y\dot{p}_y + z\dot{p}_z = 0. \qquad (2.31)$$

Substituting equations (2.30) into equation (2.31) and solving for λ yields[98]

$$\lambda = \frac{1}{2r^2}\left\{\frac{p^2}{2\mu} - x\frac{\partial V}{\partial x} - y\frac{\partial V}{\partial y} - z\frac{\partial V}{\partial z}\right\}. \qquad (2.32)$$

Whenever rigid rotor trajectories are run, the only necessary change to the procedure outlined in the preceding paragraph is to modify equations (2.28) using equations (2.30) and (2.32). Another way to handle the rigid-rotor case would be to express the Hamiltonian in terms of the rigid-rotor action-angle variables j and θ. Working in Cartesian coordinates with a constraint is more convenient because it is usually easier to express the potential in Cartesian coordinates (see section C of Chapter V, for example).

Numerical integration of the trajectories is accomplished using either the DEROOT integrator subroutine package[99] or a simple fourth-order Runge-Kutta algorithm,[100a] depending on the step size required.

For very small step sizes a significant time savings is realized using the latter of these. Both integrators call a subroutine which evaluates equations (2.28) for the particular system being studied, including the rigid rotor constraint where appropriate. Correct operation of the integrators is verified by ensuring that the total energy of the system is conserved throughout the course of a trajectory. Additional details concerning the numerical integration (choice of integrator, step size, and so on) relevant to the particular sets of calculations performed in this work are given in section B of Chapter 3 for the HCl/Au system and in section D of Chapter 5 for the NO/LiF system.

D. Analysis of Trajectory Results

When a trajectory reaches its end, the final values of the quantities of interest must be extracted from the values of the canonical variables. In these calculations, only trajectories which end when the gas molecule reaches some predetermined height above the surface after the collision are analyzed. Trajectories ending because a time limit is reached (which is the case if the molecule is trapped on the surface) are not analyzed. This latter situation arises only in the NO / LiF studies, in which there exists a mechanism for energy loss to the surface.

At the end of a trajectory the quantities of interest include the final vibrational and rotational quantum numbers v_f and J_f, the final scattering angles θ_f and Φ_f and the final energies of translation,

vibration and rotation (the latter two of these energies being referenced to the equilibrium internuclear distance r_e). The calculations are straightforward. To get the rotational quantum number J_f, one finds the classical angular momentum $\vec{j}$ and its magnitude j, using equations (2.10); from this J_f is evaluated using

$$J_f = \frac{1}{2}\left\{ \left[1 + 4\left(\Omega^2 + \frac{j^2}{\hbar^2}\right) \right]^{\frac{1}{2}} - 1 \right\} - \Omega, \qquad (2.33)$$

which is the inverse of (2.13a). For the purposes of a histogram analysis of a set of trajectories, J_f is rounded to the appropriate integer value (see below). To obtain the vibrational quantum number v_f, one calculates E_{int} at the end of a vibrating-rotor trajectory from equation (2.16), and uses it along with the angular momentum j in the procedure specified in the fourth paragraph of section B above. This gives the value of v_f corresponding to the particular E_{int} and j at the end of the trajectory. In the case of rigid-rotor trajectories, of course, v_f is simply set to zero.

The final polar and azimuthal scattering angles Θ_f and Φ_f are found from the components of the center-of-mass momentum at the end of the trajectory using the expressions

$$\Theta_f = \cos^{-1}\left\{ \frac{P_{cm,z}}{P_{cm}} \right\}, \qquad (2.34a)$$

$$\Phi_f = \tan^{-1}\left\{ \frac{P_{cm,y}}{P_{cm,x}} \right\}. \qquad (2.34b)$$

In equation (2.34a), $P_{cm} = (2ME_T^f)^{\frac{1}{2}}$, and the final translational energy

E_T^f is given by the first term on the right-hand side of (2.7′). Equation (2.34a) comes from inverting equation (2.21c); equation (2.34b) arises from dividing (2.21b) by (2.21a) and solving for Φ. Since Φ_i is always zero and also since Φ is conserved during a collision with a flat surface, Φ_f need not be calculated when a flat surface model is used.

The final energies of the various degrees of freedom of the gas molecule at the end of the collision also must be evaluated. The final translational energy E_T^f is easily computed as mentioned in the previous paragraph. Specifying the final vibrational and rotational energies for vibrating-rotor trajectories is complicated somewhat by the coupling of the vibrational and rotational motion, which arises since r^2 appears in the denominator of the last term of equation (2.11). Because the values of E_V and E_R depend on r, whose final value will not in general be the same for different trajectories, some ambiguity arises as to how to report these quantities. This problem is solved by referencing E_V^f and E_R^f to the equilibrium separation r_e in the following way. The constants of the motion for the gas molecule are its angular momentum j and energy E_{int}. Thus, the rotational and vibrational energies referenced to $r = r_e$ can be found using

$$E_R^f = \frac{j^2}{2\mu r_e^2}, \tag{2.35a}$$

$$E_V^f = E_{int} - E_R^f. \tag{2.35b}$$

Equation (2.35a) is just the last term on the right hand side of (2.11), with r replaced by r_e. Occasionally it may happen that the classical

motion of the isolated gas diatom at the end of the trajectory will have high rotational energy and very low vibrational energy. In such a case, centrifugal distortion could result in the motion having a domain of internuclear separations which does not include r_e; application of (2.35) would then yield E_R^f greater than E_{int} and, thus, E_V^f less than zero and small in magnitude. When this occurs, E_V^f is simply set to zero. For the case of a rigid rotor, no ambiguity arises; the rotational energy is equal to E_{int}.

At the end of a set of trajectories, Monte Carlo analysis can be done on the results for the set to extract the desired information. In so doing, only direct trajectories are included in the analysis. Two procedures are applied here, one for the quantum numbers and one for the average final energies. In the former case a histogram analysis is used. This involves counting how many times each particular final value of a quantum number, say J, arises in a set of N trajectories (similar considerations would apply to the vibrational quantum number v). For counting purposes, the values of J_f found from equation (2.33) are placed into bins of width 1 centered on integer values of J (that is, rounded to the nearest integer), when the diatom is heteronuclear. For the homonuclear case (which does not arise in the present work), the symmetry requires that the only allowed rotational transitions are those having ΔJ = 0 or even, so that the bins must be of width 2 centered on even or odd J, depending on whether the initial J is even or odd. (There is no symmetry restriction on vibrational transitions.) If N_J is the number of times that J_f = J, then the probability for making a transition to final state

J is just $P_J = N_J / N$. The Monte Carlo standard error in the probability is given by[92b]

$$\sigma_J = \sqrt{\frac{P_J\,(1 - P_J)}{N}} \,. \tag{2.36}$$

Thus, one can make the error as small as desired by increasing the number N of trajectories in the set, with σ_j decreasing as $N^{-\frac{1}{2}}$. The calculated probability distribution $\{P_J\}$ can be compared to the experimental distribution directly, or a Boltzmann plot, that is, a plot of $\log\{P_J/(2J+1)\}$ versus the energy $E_R(J)$, can be made.

When final average energies are the quantities of interest, these can be calculated, as usual, from

$$\langle E_M^f \rangle = \frac{1}{N} \sum_{n=1}^{N} E_{M,n}^f \,, \tag{2.37}$$

where M = T, V or R represents the appropriate degree of freedom. The Monte Carlo standard error in this calculation is given by[92c]

$$\sigma_{<E>} = \frac{\sigma_E}{N^{\frac{1}{2}}} \tag{2.38}$$

in which the standard deviation σ_E of the set of final energies $E_{M,n}^f$ is obtained from its usual estimator s_E:[92c]

$$\sigma_E \approx s_E = \sqrt{\frac{\left[\sum_n (E^f_{M,n})^2\right] - N \langle E^f_M \rangle^2}{N-1}}. \qquad (2.39)$$

Thus, again, the error in the desired value can be decresed by increasing the number of trajectories N. For studies involving a surface at a temperature T_s, another useful quantity, the energy accommodation coefficient (EAC), can be calculated using the final average energy. The EAC, which is given the symbol α, provides a measure of the extent of thermal equilibration between the gas molecule and the surface. The EAC for degree of freedom M, α_M, is defined by[97b]

$$\alpha_M = \frac{E^i_M - \langle E^f_M \rangle}{E^i_M - \langle E^s_M \rangle}, \qquad (2.40)$$

where E^i_M is the initial energy for degree M, and $\langle E^s_M \rangle$ is the average classical energy of a distribution in thermal equilibrium *with a surface* at temperature T_s. For the vibrational and rotational degrees of freedom of a diatomic molecule, $\langle E^s_M \rangle$ takes the gas-phase equipartition value kT_s, where k is Boltzmann's constant. For translational motion the gas-phase equipartition value $3kT_s/2$ is inappropriate because of the "streaming correction" due to the presence of the surface[97a]; the correct value[97a] is $2kT_s$. The initial energy in each degree of freedom (referenced to r_e for vibration and rotation) is calculated at the start of each trajectory and saved for use in equation (2.40); in any set of trajectories from which an α_M is extracted, each trajectory has the same

value for the corresponding E_M^i.

Details concerning the number N of trajectories per set and the resulting values for the error as well as the specific data analysis procedures for the various studies carried out in this work are given in section B of Chapter III and section D of Chapter V.

CHAPTER III

INTERACTION POTENTIALS AND METHODOLOGY FOR HCl/Au CALCULATIONS

This chapter and Chapter IV which follows present the application of the quasiclassical trajectory method to the scattering of HCl from a gold surface, treating HCl as a rigid rotor and the gold surface as rigid and perfectly flat. Recently Coltrin and Kay[75] applied a similar treatment to the scattering of ammonia from gold, and succeeded in obtaining a qualitative understanding of the experiments performed by Kay and coworkers[76] on that system. The present work, which was motivated by the success of the NH_3/Au study, aims at gaining an understanding of recent HCl/Au scattering experiments[1] by finding a model gas-surface interaction potential for which the trajectory results, at least qualitatively, reproduce the experimental data. In pursuit of this goal, three different model potentials have been constructed and their predictions compared to the experimental findings. Chapter IV presents the results of the trajectory calculations and compares them to the experiments. The present chapter, which explains how the calculations were performed, is divided into two sections. Section A describes the interaction potentials employed in the calculations. First the "building blocks" used to construct the potentials are discussed, then details concerning each potential are presented. Section B enumerates other computational details involved in the work.

A. HCl/Gold Interaction Potentials

In these calculations, each of the interaction potentials used consists of a sum of four terms: a long-range attraction with anisotropy, a short-range repulsion referenced to the molecular center of mass, and an atom-surface potential for both of the atoms in the HCl molecule. In each case, the functional form of the first two of these terms is the same (though values of parameters differ), while the forms chosen for the atom potentials vary from one interaction potential to another. The following paragraphs describe these various "building blocks".

The first term to be discussed is the long-range attraction. There are two contributions to this potential: the van der Waals (dispersion) interaction and the dipole-image dipole interaction. The former of these is treated first. An atom or molecule far from a solid surface experiences a long-range dispersion potential of the form[101]

$$V_{disp} = -\frac{C_3}{Z_{cm}^3}, \tag{3.1}$$

where Z_{cm} is the height of the center of mass above the surface and C_3 is a constant which depends on the polarizability of the atom or molecule and the dielectric function of the solid. Because the polarizability of a molecule is a tensor quantity, C_3 for that case depends on the orientation of the molecular axis with respect to the surface normal. Harris and Feibelman[102] have shown that for molecules

$$C_3 = C_3^{(0)} + C_3^{(2)} P_2(\cos\theta), \tag{3.2}$$

where $P_2(\cos\theta) = \frac{1}{2}(3\cos^2\theta - 1)$ is the second Legendre polynomial, θ is the angle between the molecular axis and the surface normal and

$$C_3^{(j)} = \frac{\hbar}{4\pi}\int_0^\infty \frac{\epsilon(i\omega) - 1}{\epsilon(i\omega) + 1}\ \alpha^{(j)}(i\omega)\ d\omega. \tag{3.3}$$

In equation (3.3), $\alpha^{(j)}(i\omega)$ and $\epsilon(i\omega)$ are frequency-dependent molecular polarizability and solid dielectric functions, respectively, evaluated at the imaginary frequency $i\omega$. The quantity $\alpha^{(0)} = \frac{1}{3}(\alpha_{\|} + 2\alpha_{\perp})$ in equation (3.3) is equal to α, the bulk polarizability of the molecule, while $\alpha^{(2)} = \frac{1}{6}(\alpha_{\|} - \alpha_{\perp})$ is one-sixth of its polarizability anisotropy. The symbols $\alpha_{\|}$ and $\alpha_{\perp}$ denote the components of the polarizability parallel to and perpendicular to the molecular axis, respectively. Equations (3.2) and (3.3) reduce to the Lifshitz formula[101] when the gas species is an atom, for which the polarizability anisotropy is zero.

Evaluation of the integral in equation (3.3) requires functional forms for $\alpha^{(j)}(i\omega)$ and $\epsilon(i\omega)$. For the polarizabilities $\alpha^{(j)}(i\omega)$ the $[1,0]_\beta$ Padé approximant[103] is used:

$$\alpha^{(j)}(i\omega) = \frac{\alpha^{(j)}(0)}{1 + (\omega/\omega_0)^2}, \tag{3.4}$$

where $\alpha^{(j)}(0)$ denotes the static (zero-frequency) value of $\alpha^{(j)}$. The parameter ω_0 is assumed to be the same for both $\alpha^{(0)}$ and $\alpha^{(2)}$ and is found from the expression (in Gaussian units)

$$\omega_0 = e\left[\frac{N}{\alpha\, m}\right]^{1/2} , \tag{3.5}$$

in which e is the electron charge, m the electron mass and N the number of electrons in the molecule. Equation (3.5) gives an upper bound on the polarizability.[103] For the dielectric function $\epsilon(i\omega)$, the Drude (classical electron gas) theory gives the expression[104a]

$$\epsilon(i\omega) = 1 + (\omega_p/\omega)^2 , \tag{3.6}$$

where $\omega_p = (4\pi n_c e^2/m)^{1/2}$ is the plasma frequency of the metal, and n_c its free-electron density. If equations (3.4) and (3.6) are substituted into equation (3.3) and the integration is performed using the identity[105]

$$\frac{1}{x + y} = \frac{2}{\pi}\int_0^\infty \frac{xy\, du}{(x^2 + u^2)\,(y^2 + u^2)} , \tag{3.7}$$

one obtains

$$C_3^{(j)} = \frac{\hbar\omega_p\omega_0\alpha^{(j)}(0)}{8(\omega_p + \sqrt{2}\,\omega_0)} . \tag{3.8}$$

It remains to evaluate the $C_3^{(j)}$ for the specific case of HCl/gold. For HCl, Bridge and Buckingham[106] measured the bulk polarizability and polarizability anisotropy of HCl as $\alpha = 2.600$ Å^3 and $(\alpha_\parallel - \alpha_\perp) = 0.311$ Å^3, from which $\alpha^{(0)} = \alpha = 2.600$ Å^3 and $\alpha^{(2)} = 0.0518$ Å^3. Using α along with $N = 18$ electrons for HCl yields $\omega_0 = 4.187 \times 10^{16}$ s^{-1}. Taking

$n_c = 5.90 \times 10^{22}$ cm^{-3} for gold[104a] gives the value $\omega_p = 1.37 \times 10^{16}$ s^{-1} for the plasma frequency. Putting these numbers into equation (3.8) renders the values $C_3^{(0)} = 1.683$ eV $Å^3$ and $C_3^{(2)} = 0.03366$ eV $Å^3$.

The contribution to the long-range attraction due to the interaction of the dipole moment of the molecule with its image in the solid can be found by first considering the interaction of two dipoles in free space. The potential energy of a dipole $\vec{\mu}_2$ in the electric field $\vec{E}_1(r)$ of another dipole $\vec{\mu}_1$ a distance r away is $V_{\mu-\mu} = -\vec{\mu}_2 \cdot \vec{E}_1(r)$, with $\vec{E}_1(r)$ given by[109]

$$\vec{E}_1(r) = \frac{3\,\hat{r}\,(\vec{\mu}_1 \cdot \hat{r}) - \vec{\mu}_1}{r^3}, \tag{3.9}$$

where $\hat{r}$ is a unit vector along the line joining the centers of the dipoles, directed from $\vec{\mu}_1$ to $\vec{\mu}_2$. $\vec{E}_1$ and $V_{\mu-\mu}$ are, of course, dependent on the relative orientation of $\vec{\mu}_1$ and $\vec{\mu}_2$. One can thus write $V_{\mu-\mu}$ explicitly as

$$V_{\mu-\mu} = \frac{\vec{\mu} \cdot \vec{\mu} - 3\,(\vec{\mu} \cdot \hat{r})\,(\vec{\mu} \cdot \hat{r})}{r^3}. \tag{3.10}$$

For simplicity the case of coplanar dipoles is considered. This situation is pictured in part (a) of Figure 2. The angle between $\hat{r}$ and $\vec{\mu}_1$ is θ_1 and that between $\hat{r}$ and $\vec{\mu}_2$ is θ_2, while the angle between $\vec{\mu}_1$ and $\vec{\mu}_2$ is $(\theta_1 + \theta_2)$. With these definitions equation (3.10) becomes

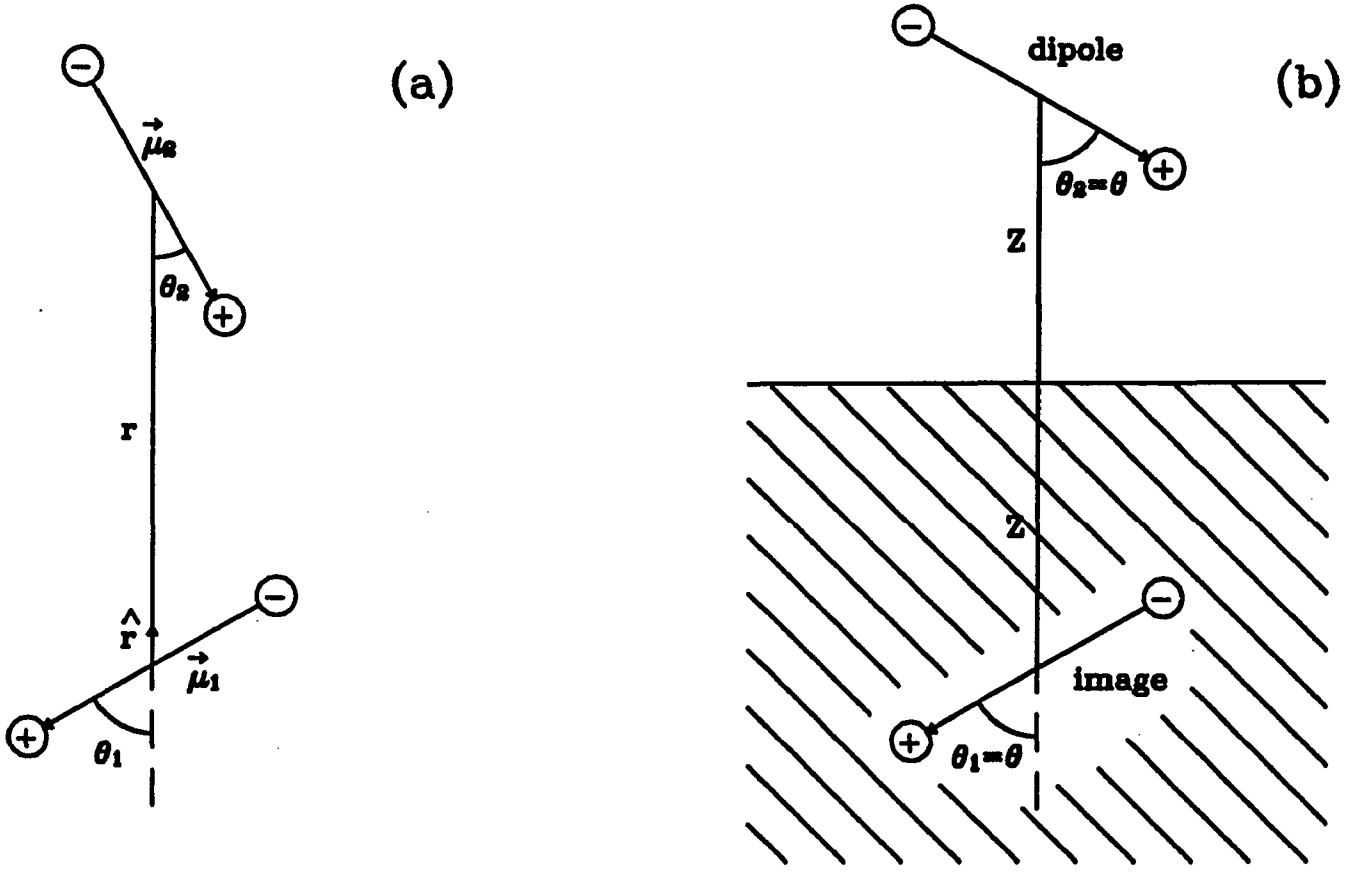

Figure 2. Relative orientations of (a) two coplanar dipoles in free space, and (b) a dipole near a solid and its image within the solid.

$$V_{\mu\text{-}\mu}(r,\theta_1,\theta_2) = \frac{\mu_1 \mu_2}{r^3}\left[\cos(\theta_1 + \theta_2) - 3\cos\theta_1\cos\theta_2\right]$$

$$= -\frac{\mu_1 \mu_2}{r^3}\left[\sin\theta_1 \sin\theta_2 + 2\cos\theta_1 \cos\theta_2\right], \quad (3.11)$$

where $\mu_i = |\vec{\mu}_i|$. The force $F_r(r;\theta_1,\theta_2)$ exerted by $\vec{\mu}_1$ on $\vec{\mu}_2$ at r in the $\hat{r}$ direction, with θ_1 and θ_2 fixed, is then

$$F_r(r;\theta_1,\theta_2) = -\frac{\partial V(r,\theta_1,\theta_2)}{\partial r}$$

$$= -\frac{3\mu_1\mu_2}{r^4}\left[\sin\theta_1 \sin\theta_2 + 2\cos\theta_1 \cos\theta_2\right]. \quad (3.12)$$

The force in equation (3.12) may be either attractive or repulsive, depending on the values of θ_1 and θ_2. Given such an expression for the force, the potential energy imparted to $\vec{\mu}_2$ as it is brought from $r' = \infty$ (where $V = 0$) to $r' = r$ is given by $V(r) = -\int_\infty^r F_r(r';\theta_1,\theta_2)\, dr'$. Performing this integration on equation (3.12) yields equation (3.11), as it should.

At this point one can discuss the dipole-image dipole situation, which is depicted in part (b) of Figure 2. When a dipole lies a distance Z above a metal surface, a mirror image is formed in the metal a distance Z below the surface, so that the distance between the center of the dipole and the center of its image is 2Z. As Figure 5-1b shows, the mirror-image geometry requires that $\theta_1 = \theta_2 = \theta$. In addition, the magnitudes of the dipole and its image are equal, so that $\mu_1 = \mu_2 = \mu$. One can therefore immediately write down the force in the Z direction exerted on the dipole at Z by its image, using equation (3.12):

$$F_Z(Z;\theta) = -\frac{3\mu^2}{(2Z)^4}\left[\sin^2\theta + 2\cos^2\theta\right]$$

$$= -\frac{3\mu^2}{16Z^4}\left(1 + \cos^2\theta\right). \qquad (3.13)$$

This force is always attractive. The potential energy of the dipole-image dipole interaction, that is, the potential energy imparted to the dipole by bringing it from infinity to Z at some fixed θ, can be found by integrating equation (3.13):

$$V_{\mu\text{-}i\mu} = \frac{3\mu^2}{16}\left(1 + \cos^2\theta\right)\int_{\infty}^{Z}\frac{dZ'}{Z'^4}$$

$$= -\frac{C_{dip}}{Z^3}\left(1 + \cos^2\theta\right), \qquad (3.14)$$

where $C_{dip} = \mu^2/16$. The seemingly roundabout procedure of writing down the force and integrating to find the potential is necessary to obtain the correct final result; if one simply substitutes $\theta_1 = \theta_2 = \theta$, $\mu_1 = \mu_2 = \mu$ and $r = 2Z$ into equation (3.11) for $V_{\mu\text{-}\mu}$, one obtains $C_{dip} = \mu^2/8$, which is wrong by a factor of two. Using the value $\mu = 1.093$ Debye for HCl[108] gives $C_{dip} = 0.04662$ eV Å^3.

Based on the above, the overall long-range attraction can be written as

$$V_{LR} = V_{disp} + V_{\mu\text{-}i\mu} = -\frac{D + E\cos^2\theta}{(Z_{cm} - Z_0)^3}, \qquad (3.15)$$

in which

$$D = C_3^{(0)} - \frac{1}{2} C_3^{(2)} + C_{dip} = 1.713 \text{ eV Å}^3, \quad (3.16a)$$

$$E = \frac{3}{2} C_3^{(2)} + C_{dip} = 0.09711 \text{ eV Å}^3. \quad (3.16b)$$

To arrive at the rightmost member of equation (3.15), it is assumed that the distance Z of the center of the dipole from the surface in equation (3.14) can be replaced by the height Z_{cm} of the center of mass. The parameter Z_0 in the denominator has been included to give increased flexibility in fitting the overall gas-surface potential, as discussed below. In all the interaction potentials used for trajectory calculations, values of D and E from (3.16) are used; the only change in V_{LR} from potential to potential is in the value of Z_0.

The second term used in constructing the HCl-gold potentials is the short-range center-of-mass repulsion. It has the form

$$V_{SR} = \frac{C_9}{(Z_{cm} - Z_0)^9}, \quad (3.17)$$

where C_9 is a constant and Z_0 is, in most cases, the same parameter that appears in V_{LR}. Such an expression arises if one assumes Lennard-Jones repulsions (r^{-12}) between the gas species and the atoms of the solid, then approximates the solid as a semi-infinite continuum and integrates over its extent.[105] The values of the parameters C_9 and Z_0 are determined by fitting the overall interaction potential V_{gs} to have certain features. This is accomplished in two steps. First, a specific height

and orientation of the molecule with respect to the surface are chosen, and values are assigned to all but n of the potential parameters, where n = 2 or 3. Then n equations are simultaneously solved for the n remaining parameters. For example, if n = 2 then the two unknowns are C_9 and Z_0. If n = 3 then some parameter appearing in one or both of the atom potentials (see below) is determined along with C_9 and Z_0. The equations to be solved include in every case $V_{gs} = \delta$ and $\partial V_{gs}/\partial Z_{cm} = 0$. The first of these equations fixes the depth δ of V_{gs} at the specified height and orientation. The second requires that the potential reach a minimum with respect to Z_{cm} at the selected height and geometry; this minimum may or may not be the absolute minimum of V_{gs}. When n = 3, a third equation is added which establishes some other property of V_{gs}. Further details concerning the fitting procedure for each of the interaction potentials used in the calculations are provided later in the chapter.

Remaining to be examined are the various forms used for the atom potentials. Three types of atom potentials are employed: repulsive exponential, Morse and modified Morse. The exponential repulsion is simply

$$V_i^{EXP} = A_i \exp(-\alpha_i Z_i) , \tag{3.18}$$

where Z_i is the height of atom i above the surface and A_i and α_i are parameters. The Morse potential is

$$V_i^{M} = B_i \left\{ \exp[-2\beta_i(Z_i - Z_i^{eq})] - 2 \exp[-\beta_i(Z_i - Z_i^{eq})] \right\}, \tag{3.19}$$

in which B_i, β_i and Z_i^{eq} are parameters. When $Z_i = Z_i^{eq}$, the Morse potential obtains its minimum value, $-B_i$. The modified Morse function differs from equation (3.19) only in that a factor of $\cos^2\theta$ is included in the attractive portion:

$$V_i^{MM} = B_i \left\{ \exp[-2\beta_i(Z_i - Z_i^{eq})] - 2\cos^2\theta \exp[-\beta_i(Z_i - Z_i^{eq})] \right\}. \quad (3.20)$$

This modified Morse potential was employed by Muhlhausen *et al.*[86] in their stochastic trajectory study of NO interactions with Ag(111) and Pt(111). The effect of the $\cos^2\theta$ term, where as usual θ represents the angle between the molecular axis and the surface normal, is to ensure that the minimum of the overall potential occurs when the molecule is aligned normal to the surface. Except for B_i, all of the parameters appearing in equations (3.18) through (3.20) are taken from the literature or reasonable estimates. B_i, when it appears, is determined along with C_9 and Z_0 in the fitting procedure. It should be noted that for a heteronuclear diatomic molecule such as HCl, the overall potential should include a contribution from odd powers of $\cos\theta$. In the present case, the various atom potentials provide this contribution, as well as one from even powers of $\cos\theta$, through the dependence on $\cos\theta$ of the atomic coordinates Z_i which appear in the various exponents.

With the above building blocks, overall interaction potentials for the HCl-gold system can be put together for use in trajectory calculations. In this work three potentials have been used to run trajectories. The first of these, designated hereafter as the "strongly perpendicular" (SP) potential, has the form $V_{SP} = V_{LR} + V_{SR} + V_H^{EXP} + V_{Cl}^{MM}$. The values of

Table 1. Parameters for the SP potential.

Potential Term	Parameter	Value
H atom exponential repulsion[a]	A_H	634.45 eV
	α_H	3.366 $Å^{-1}$
Cl atom modified Morse potential[b]	B_{Cl}	0.2308 eV
	β_{Cl}	1.887 $Å^{-1}$
	Z_{Cl}^{eq}	2.30 Å
Center-of-mass repulsion[c]	C_9	41.438 eV
	Z_0	0.587 Å

[a] see equation (5.18).

[b] see equation (5.20).

[c] see equation (5.17). Z_0 also appears in the long-range attraction, equation (5.15).

the various parameters for V_{SP} are given in Table 1. The values of A_H and α_H for the H atom repulsion were taken from the NH_3-gold calculations of Coltrin and Kay[75]. The modified Morse exponential constant β_{Cl} is the same as that used by Ron *et al.*[109], while the Cl-surface equilibrium distance Z_{Cl}^{eq} was estimated from calculations of halogen interactions with copper[110] and silver[111] clusters. The modified Morse depth B_{Cl} was determined along with C_9 and Z_0 in the fitting procedure. The third equation used in the fit was $\partial^2 V_{SP}/\partial Z_{cm}^2 = k$, where k is the force constant for the molecule-surface vibration. The potential was constrained to have $\delta = 350$ meV with the HCl molecule at $Z_{cm} = 2.5$ Å and oriented perpendicular to the surface with the chlorine end down. This is the absolute minimum of the SP potential. The HCl-gold vibrational frequency was chosen to be 143 cm^{-1} (for which $k = 2.71$ eV/Å^2). The location and depth of the minimum were reasonable estimates in the absence of any experimental data; the frequency was estimated from reference 111.

A contour plot of the strongly perpendicular potential V_{SP} is presented in Figure 3. In this and similar figures to follow, θ is the angle between the molecular axis and the surface normal (not to be confused with the Euler angle θ), and $\theta = 0°$ means that the HCl molecule is aligned normal to the surface with the chlorine end down. Only the range $0° \leq \theta \leq 180°$ is presented because the potential is symmetric about $\theta = 0°$. The force on the molecule in the Z_{cm} direction is given by $-\partial V_{SP}/\partial Z_{cm}$, while the torque around the center of mass is $-\partial V_{SP}/\partial\theta$; hence, contour lines parallel to the θ axis contribute to the force but not to the torque, and the converse is true for lines parallel to the

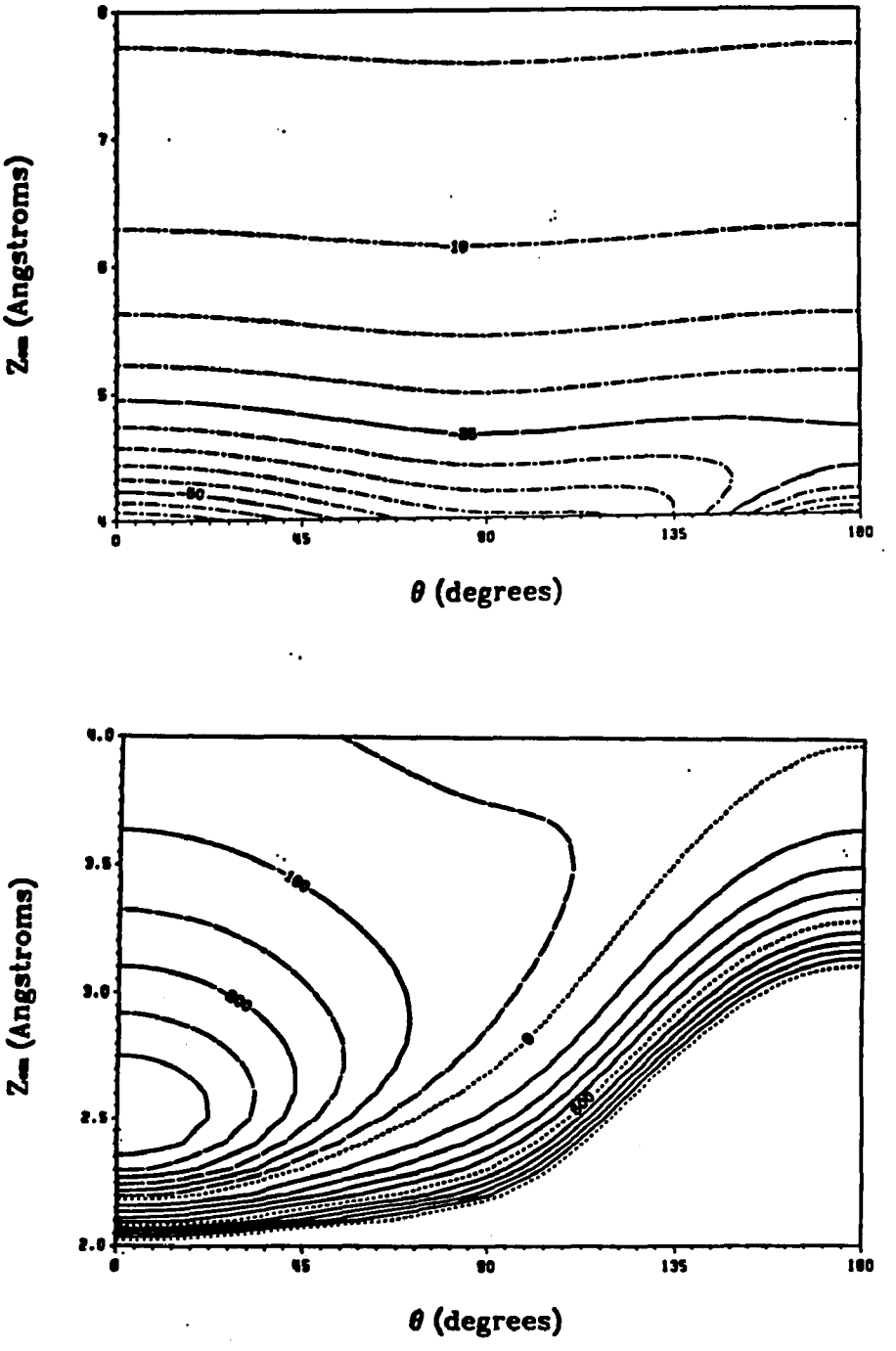

Figure 3. Contour plots of the SP potential. Contour lines are distinguished as follows: dotted, multiples of 500 meV; solid, multiples of 100 meV; short-dashed, odd multiples of 50 meV; long-dashed, odd multiples of 25 meV; dot-dashed, multiples of 5 meV. A few contours are labeled (in meV) for reference.

Z_{cm} axis. The strength of the force and/or torque at a particular point is determined by how closely spaced the contour lines are. Figure 3 indicates that the SP interaction exhibits relatively strong torques toward $\theta = 0°$ at all values of θ when Z_{cm} is less than about 4 Å (this is the origin of the name "strongly perpendicular"). The strength of the torque is indicated by the sharp increase in V_{SP} as θ increases through its range. At larger values of Z_{cm}, a much weaker torque toward $\theta = 0°$ or $\theta = 180°$ (depending on whether θ is greater or less than 90°) is exerted on the molecule. The long-range torque is due to the anisotropic part of the long-range term in the potential, V_{LR}. The strength and extent of the short-range torque is due to the magnitude of the H atom exponential repulsion, while the fact that the torque is experienced for all θ arises from the $\cos^2\theta$ factor in the modified Morse potential.

The second potential used for trajectory calculations is the "weakly perpendicular" (WP) potential, $V_{WP} = V_{LR} + V_{SR} + V_H^{EXP} + V_{Cl}^{EXP}$. Here the modified Morse potential on the Cl atom has been replaced by an exponential repulsion and the strength of the H atom repulsion has been reduced, resulting in a decrease in the strength and range of the short-range forces which align the molecule perpendicular to the surface (hence the name "weakly perpendicular"). Constants for V_{WP} are listed in Table 2. The parameters in the exponential repulsions were determined by calculating Morse parameters for each atom using chemisorption data, then using only the repulsive part of the resultant Morse potentials, with the equilibrium distances Z_i^{eq} set to zero. Results of theoretical calculations for the chemisorption of chlorine on silver[111] and hydrogen on gold[112] were used in this process. The values of C_9 and Z_0 were found

Table 2. Parameters for the WP potential.

Potential Term	Parameter	Value
H atom exponential repulsion[a]	A_H	2.45 eV
	α_H	2.12 $Å^{-1}$ [b]
Cl atom exponential repulsion[a]	A_{Cl}	2.59 eV
	α_{Cl}	1.586 $Å^{-1}$ [b]
Center-of-mass repulsion[c]	C_9	6.76 eV
	Z_0	0.75145 Å

[a] see equation (5.18).

[b] twice the value of the Morse exponential parameter obtained from chemisorption data.

[c] see equation (5.17). Z_0 also appears in the long-range attraction, equation (5.15).

by fitting the potential to have a well depth of 5 kcal/mole (≈220 meV) at Z_{cm} = 2.33 Å and θ = 110.7°. The 5 kcal/mole well depth was determined in the HCl/Au experiments.[1] (This value was not used in constructing the SP potential described previously, because the calculations for that potential were performed before the experiments were done.) The choice of Z_{cm} and θ corresponds to the orientation the molecule would have if the distances of the H and Cl atoms from the surface were equal to their equilibrium distances as determined from the chemisorption data. The intention was that the global minimum would lie at this geometry; however, the actual minimum was found to be 284 meV at Z_{cm} = 2.30 Å and θ = 0°. A contour plot of the WP potential comprises Figure 4. Comparing this with Figure 3 shows that the magnitude of the short-range orienting forces has been greatly reduced in V_{WP}, since the potential does not rise nearly as abruptly as θ increases for a given value of Z_{cm}. In addition, the fact that the contour lines in the potential well stop forming closed loops much closer to the surface in Figure 4 indicates that the range of these torques has decreased. Also noteworthy is that the anisotropy (the slope with respect to θ) at the hard wall for this interaction is much less than for the SP potential, particularly for $\theta \geq 90°$; this reflects the decrease in the strength of the H atom repulsion. The smaller hard-wall anisotropy means that molecules which actually strike the wall with the hydrogen end down experience much less torque during the encounter.

The third gas-surface potential employed in these studies, labeled as the "almost parallel" (AP) potential, is given by $V_{AP} = V_{LR} + V_{SR} +$

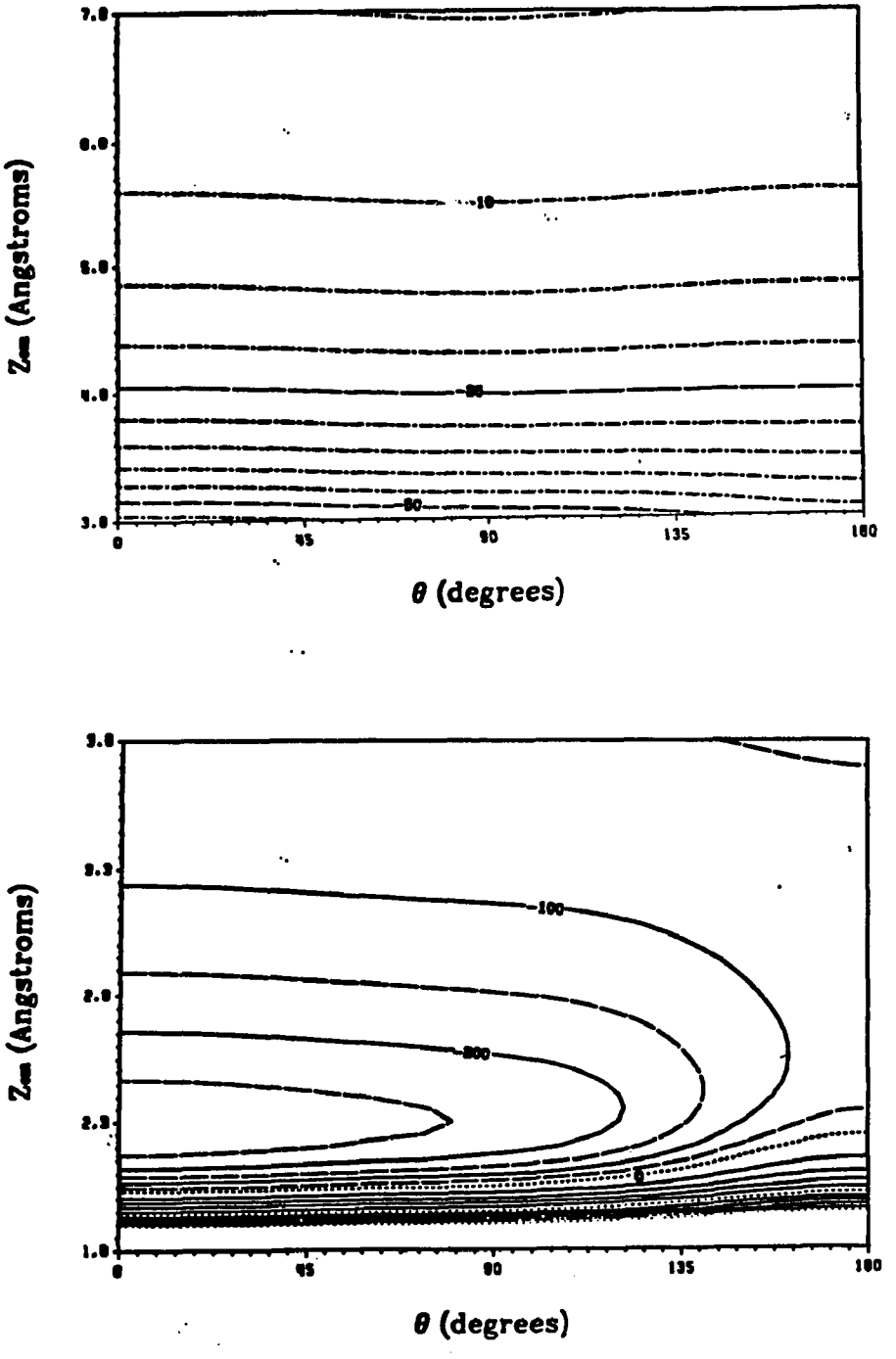

Figure 4. Contour plots of the WP potential. Contour lines have the same interpretation as in Figure 3.

$V_H^M + V_{Cl}^M$. This potential is so named because the minimum of the potential occurs with the HCl molecule oriented nearly parallel to the surface; such an orientation at the minimum was achieved by putting Morse potentials on both atoms. The constants used in V_{AP} are listed in Table 3. The Morse parameters β_i and Z_i^{eq} are the ones calculated from chemisorption data[111,112] for use in the WP potential. The depth parameter $B = B_H = B_{Cl}$ was determined along with C_9 and Z_0 in the fitting procedure; in the fit the same depth B was used for each atom, since the well depths determined from the chemisorption data were very similar (compare the values of A_H and A_{Cl} in Table 2). The third equation used in the fit was $\partial V_{AP}/\partial(\cos\theta) = 0$, which requires the specified geometry to be a minimum with respect to θ. Also, for this potential the parameter Z_0 was set to zero in the long-range term V_{LR}, so that it appears in the overall potential only through the V_{SR} term. The AP potential was fit to have $\delta = 217$ meV (the experimental value) at $Z_{cm} = 2.33$ Å and $\theta = 112.3°$. It was found that the values of C_9, Z_0 and B were very sensitive to the value of θ used in the fit for θ near 110.7°, so that small changes in θ produced large changes in the parameters. This enabled θ to be adjusted such that the value of Z_0 obtained in the fit was very nearly zero (3×10^{-5} Å), which was convenient in that the trajectory code did not have to be modified to remove Z_0 from the long-range term in the potential. Figure 5 contains a contour plot of V_{AP}. The figure clearly shows that close to the surface ($Z_{cm} \lesssim 3$ Å) this potential turns the molecule toward a parallel alignment, especially for $\theta \gtrsim 45°$, while at large distances the long-range anisotropy rotates the molecule toward the normal. At intermediate heights (between about 3 and

Table 3. Parameters for the AP potential.

Potential Term	Parameter	Value
H atom Morse potential[a]	B_H	0.06229 eV
	β_H	1.06 $Å^{-1}$
	Z_{Cl}^{eq}	1.89 Å
Cl atom Morse potential[a]	B_{Cl}	0.06229 eV
	β_{Cl}	0.793 $Å^{-1}$
	Z_{Cl}^{eq}	2.34 Å
Center-of-mass repulsion[c]	C_9	89.094 eV
	Z_0	0.0000 Å

[a] see equation (5.19).

[b] see equation (5.17). Z_0 is also set to zero in equation (5.15).

6 Å), the potential rotates the molecule toward $\theta = 180°$ (H end down) almost exclusively. The anisotropy at the hard wall is about the same as that for the WP potential, although a little larger at high values of θ.

B. Computational Details

The actual implementation of the HCl-gold calculations is quite straightforward. For each of the interaction potentials described in the previous section, two groups of four sets of trajectories were run. Each set in the first group, from which rotational state distributions were extracted for comparison with the experimental results, consisted of 4000 trajectories and employed Monte Carlo selection of the initial diatom orientation. The set size was sufficient to bring the Monte Carlo error in the probability, given by equation (2.36), to less than 10% for any state having probability greater than 0.025. Each set in the second group, from which excitation functions (final J as a function of initial diatom orientation) were obtained, systematically selected the initial polar orientation angle θ_i from its range $0° \leq \theta_i \leq 180°$ in steps of 0.1° (1801 trajectories total). Each trajectory had initial rotational quantum number $J_i = 0$. In addition to these, another group of four 4000-trajectory sets was run for the WP potential, which used Monte Carlo selection for both the initial diatom orientation and the initial rotational quantum number. The four sets of trajectories in each of the above groups were distinguished by the value of the incident energy E_T; the values of E_T were 100, 350, 700 and 1000 meV. Each set used an

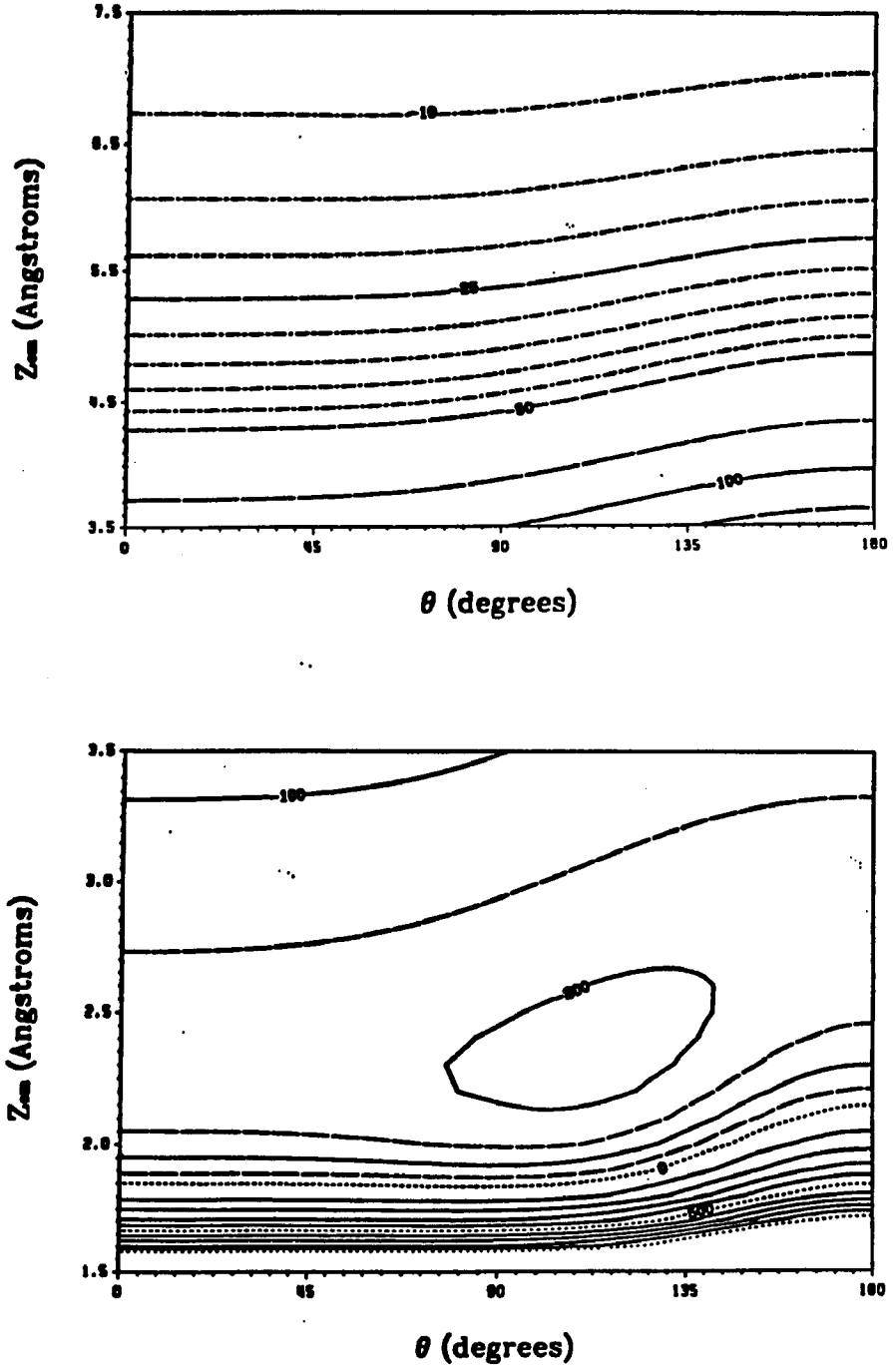

Figure 5. Contour plots of the AP potential. Contour lines have the same interpretation as in Figure 3.

initial incidence angle $\theta_i = 0°$ (normal incidence). The diatom was in all cases treated as a rigid rotor with internuclear distance constrained to be the equilibrium distance $r_e = 1.2746$ Å.[93c] The atomic masses used in the calculations were $m_H = 1.0078$ amu and $m_{Cl} = 34.9688$ amu. The HCl spectroscopic constants[93c] were $B_e = 10.5909$ cm^{-1}, $\alpha_e = 0.3019$ cm^{-1} and $D_e = 5.32 \times 10^{-4}$ cm^{-1}.

The procedure for computing a set of trajectories consists of the following steps. At the start of the set, the molecular constants for HCl and the parameters for the gas-surface interaction potential of interest are input to the trajectory code, along with the values of E_T, θ_i and J_i (unless J_i is selected using the Monte Carlo procedure). Then the individual trajectories are run. To do this, initial conditions are established as described in section B of Chapter 2, based on the values of E_T, θ_i and J_i; the values of any other necessary quantities are randomly or systematically assigned by the program, except for the initial height Z_{in}, which is 20 Å for all trajectories. When J_i is randomly selected, the required cumulative probability distribution is built from the experimental probability distribution of states in the incident HCl molecular beam (given in section A of Chapter IV). To select the HCl orientation angle θ_i systematically, the Euler angles θ and ϕ are set to 90° and 0°, respectively, and ψ is varied from -90° to 90° in steps of 0.1°. After the initialization, Hamilton's equations of motion (2.28) are integrated, with the rigid-rotor constraint given by equations (2.30) and (2.32), using the appropriate gas-surface interaction potential. The end of the trajectory occurs when the diatom reaches a height of 20 Å above the surface after the collision; all HCl/Au trajectories

end in this manner since in the rigid-surface approximation molecules cannot become permanently trapped on the surface. When the trajectory is over, the final rotational quantum number J_f and the final rotational energy E_R^f are extracted from the coordinates and momenta. After the entire set of trajectories has completed, a histogram analysis is performed to compute final rotational state distributions and Boltzmann plots, and the average final rotational energy for the set is also evaluated. Section D of Chapter 2 describes the analysis procedures.

Numerical integration of the trajectories was accomplished using the DEROOT integrator subroutine package[99], which automatically adjusts its order and step size to control the error. The integrator typically achieved energy conservation of better than 0.005% at E_T = 100 meV and better than 10^{-4}% at the higher incident energies used. The calculations were performed on the IBM 3081D at the Ohio State University and on the Cray X-MP at the Ohio Supercomputer Center in Columbus, Ohio. A typical set of 4000 trajectories at E_T = 100 meV took roughly 32 CPU-minutes on the IBM and about 5 CPU-minutes on the Cray; at E_T = 1 eV these times decreased to 15 minutes on the IBM and 2.3 minutes on the Cray.

CHAPTER IV

RESULTS OF HCl/Au TRAJECTORY CALCULATIONS

This chapter presents the results of the QCT calculations performed on the scattering of HCl from gold using the model interaction potentials described in the previous chapter, and compares them to the experimental findings of Kay and Lykke.[1] Section A contains an overview of the experimental results. The results of the trajectory calculations are then described in Section B. The discussion in that section begins with a brief summary of the NH_3/Au trajectory study of Coltrin and Kay,[75] which provided a starting point for thinking about the HCl/Au problem. Then, for each of the interaction potentials, calculated final rotational state distributions are analyzed, and the associated Boltzmann plots and average final rotational energies are compared with the experimental ones. Finally, Section C contains a discussion of the conclusions which can be drawn from the work.

A. Experimental Results for HCl/Au Scattering

The experiments which motivated the present calculations are those conducted by Kay and Lykke[1] on the scattering of HCl from the Au(111) surface. The incident HCl molecules were produced in seeded supersonic molecular beams, using various carrier gases to obtain different

incident energies. Velocities and internal states of the scattered molecules were determined using time-of-flight (TOF) and multiphoton ionization (MPI) spectroscopy, respectively. Experiments were conducted for several surface temperatures between 100 K and 800 K. The pertinent results of these experiments are presented in Figures 6 through 9, which come directly from reference 1. The remainder of this section describes these results.

Figure 6 shows the multiphoton ionization (MPI) spectra of the incident and scattered HCl molecules for a typical experiment, along with the MPI spectrum of HCl gas at 300 K. In that experiment, the surface temperature was 300 K, the incident beam (middle panel of Figure 6) had a translational energy of 17.9 kcal/mole, or 776 meV, and the approximate rotational "temperature" of the molecules in the beam was about 10 K. The only rotational states with appreciable population in the incident beam were J = 0, 1 and 2; the percentages of each of these states in the beam (determined from Figure 6) were 85.2%, 10.4% and 4.4%, respectively. These percentages did not vary significantly over the range of translational energies studied. The final state distribution of the scattered HCl (bottom panel) appears Boltzmann-like, with a rotational "temperature" somewhat in excess of the surface temperature of 300 K, based on a comparison with the static gas spectrum (top panel). The fact that the final rotational temperature does not equal the surface temperature suggests that the scattering proceeds via a direct rather than a trapping/desorption mechanism. Boltzmann plots of the experimental final state distributions for several incident energies of motion normal to the surface are presented in Figure 7. The fact that these are

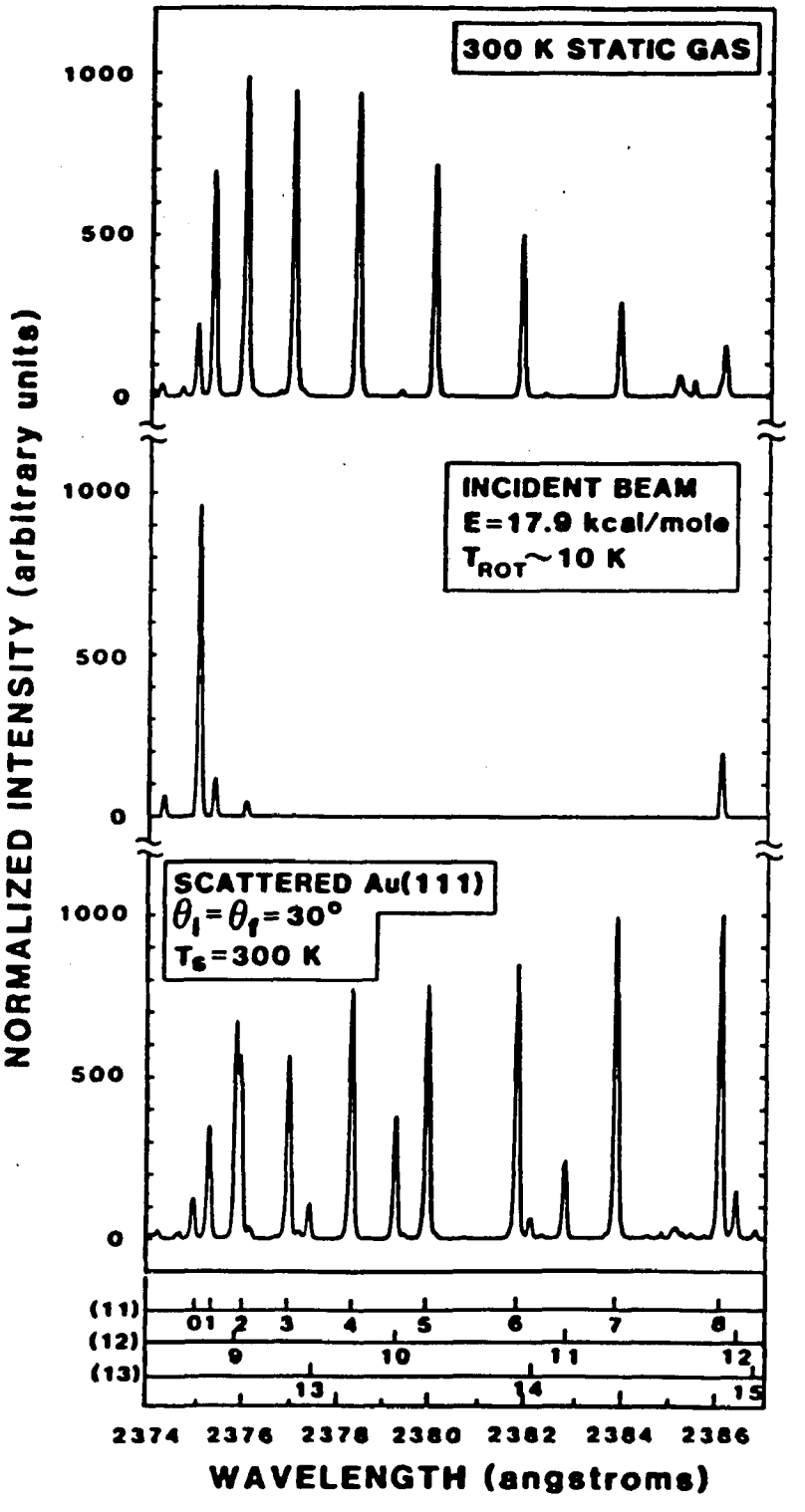

Figure 6. Comparison of MPI spectra for HCl in a 300 K static gas (top panel), a typical incident molecular beam (middle panel), and scattered from a 300 K Au(111) surface (lower panel). The figure is taken directly from reference 1.

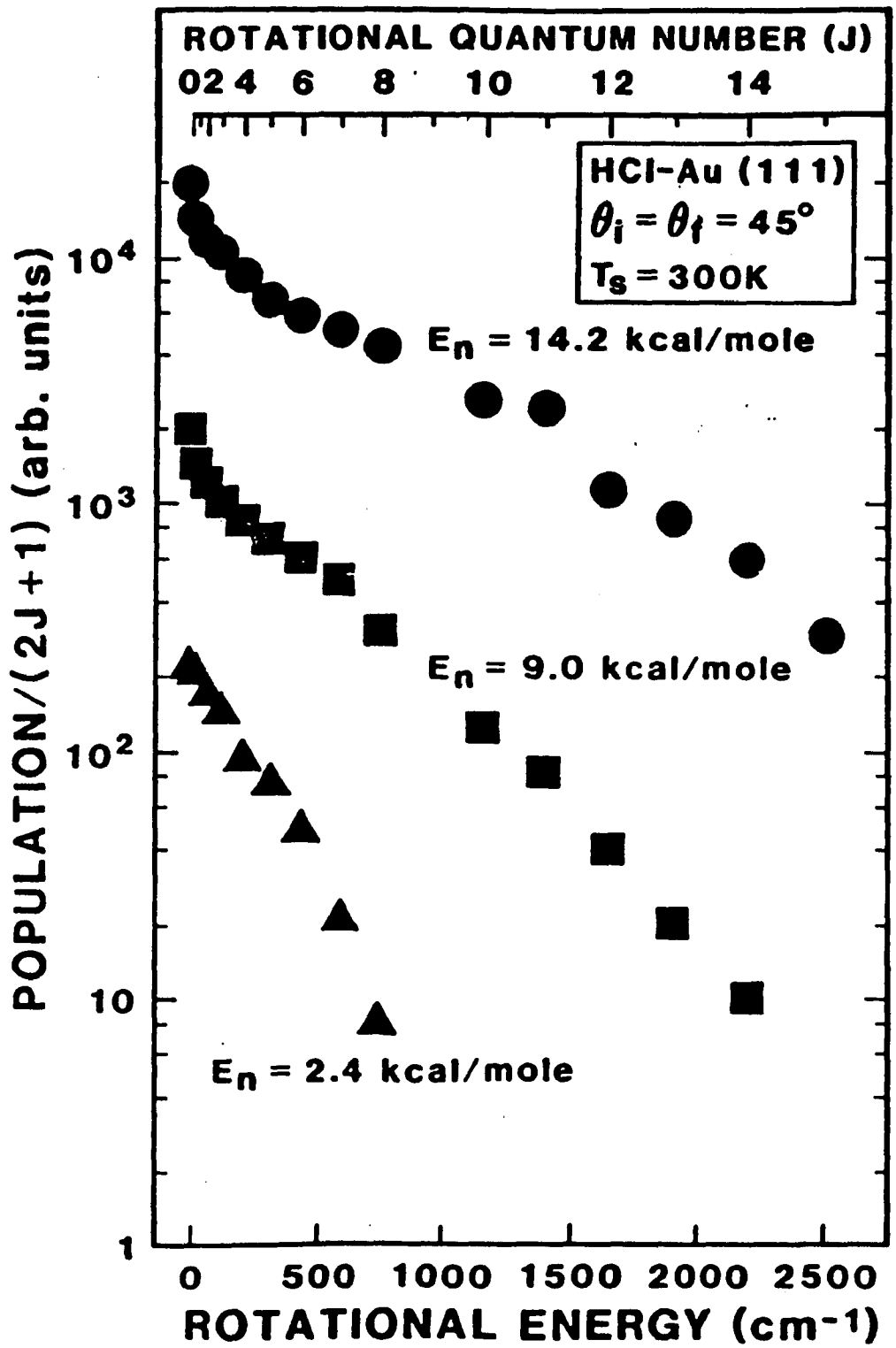

Figure 7. Experimental rotational Boltzmann plots for HCl scattered from Au(111), for several incident kinetic energies of normal motion. The figure is taken directly from reference 1.

relatively linear reflects the resemblance of the distributions to Boltzmann distributions. In light of the calculations to be discussed later in the chapter, it is interesting to note that a slight peak at $J_f = 0$, which evinces a zero-energy rotational rainbow, appears in the Boltzmann plots at $E_T = 9.0$ kcal/mole (390 meV) and at $E_T = 14.2$ kcal/mole (616 meV), but not at all at $E_T = 2.4$ kcal/mole (104 meV). At higher values of J_f the Boltzmann plots show a very faint shoulder, which may indicate the presence of a rotational rainbow at nonzero rotational energy.

A plot of the experimental average final rotational energy of the scattered HCl versus the incident kinetic energy of normal motion is presented in Figure 8. The graph shows that the degree of rotational excitation depends linearly on the incident energy of normal motion; the slope of the least-squares line obtained from the data is 0.08, indicating that about 8% of the incident translational energy is converted to rotational energy in the scattering process. Also, the rotational excitation is independent of the energy of motion tangential to the surface, since Figure 8 indicates that experiments conducted with the same normal energy but different tangential energies (different incidence angles) yielded essentially the same value for the mean rotational energy. This result indicates that the surface is relatively flat, since tangential motion is unaffected by a collision with a flat surface. Thus the flat-surface approximation used in these calculations would appear to be acceptable for this case. Another important piece of information which one can extract from Figure 8 is an estimate of the average well depth of the gas-surface interaction potential. To do this, one assumes (by

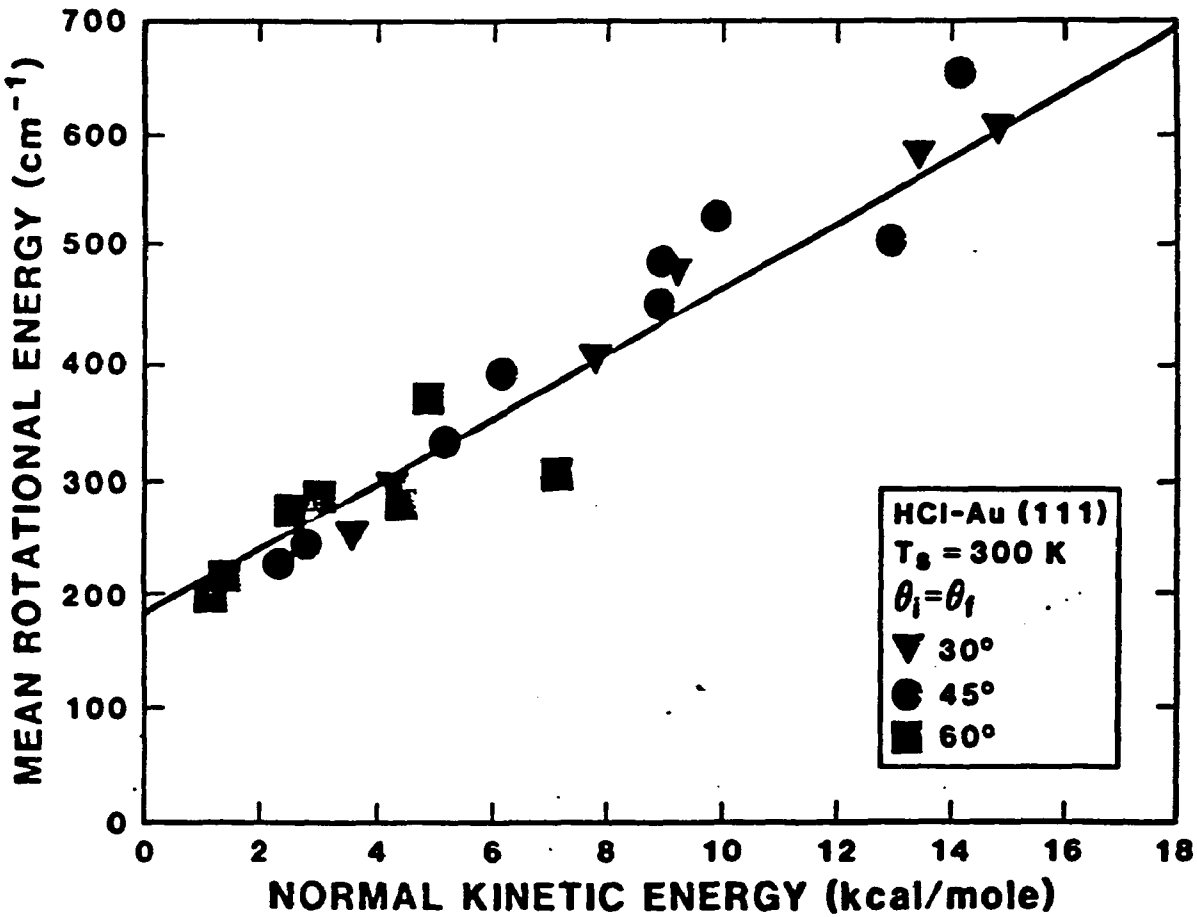

Figure 8. Experimental dependence of the average final rotational energy of scattered HCl on the incident energy of normal motion. The figure is taken directly from reference 1.

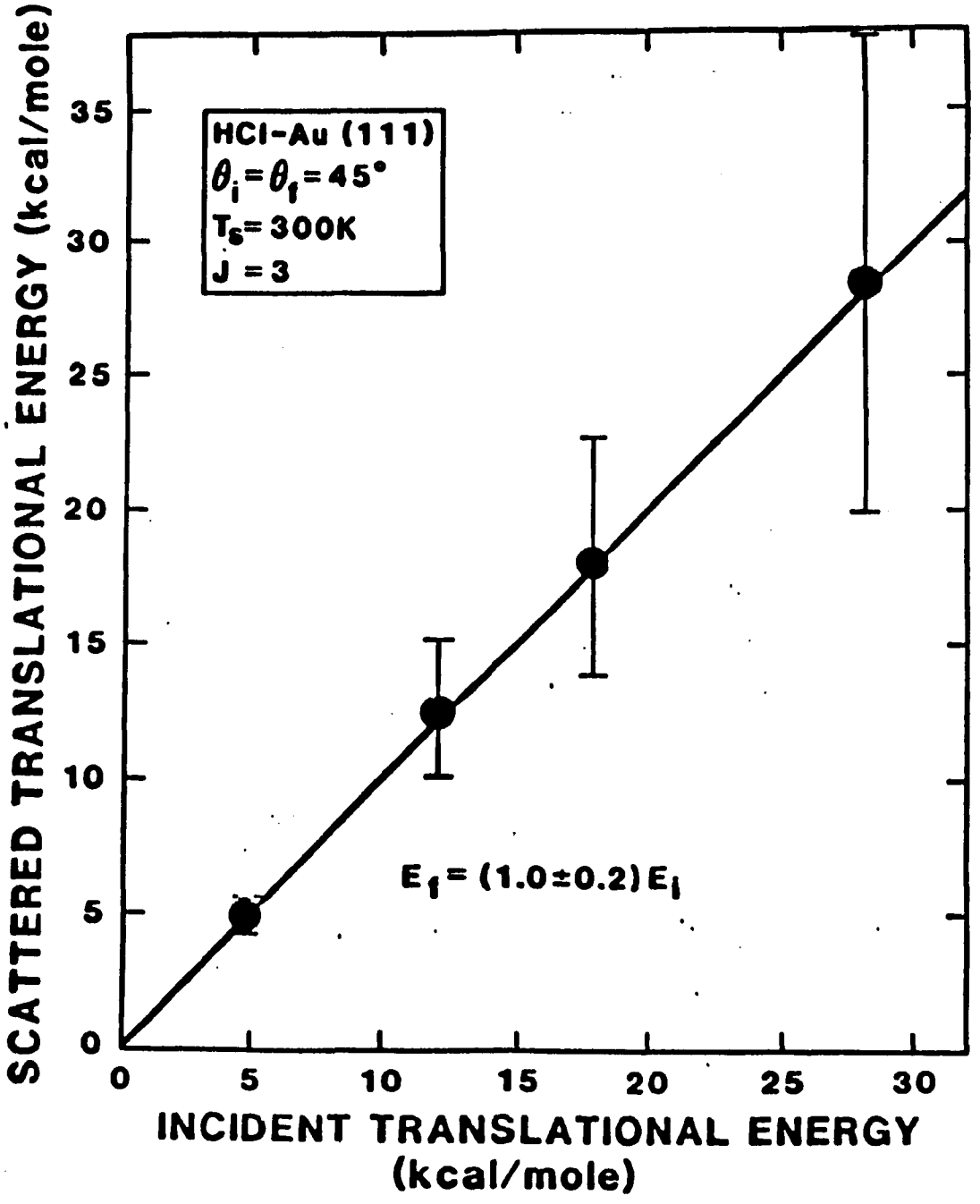

Figure 9. Experimental dependence of the translational energy of scattered HCl on the incident translational energy. The figure is taken directly from reference 1.

analogy to the case of a square-well potential) that the molecule strikes the surface with an energy equal to the sum of the incident translational energy and the well depth. This suggests that the value of $\langle E_R^f \rangle$ where $E_T = 0$ (i.e. the y-intercept of the least-squares line in Figure 8) is 8% of the well depth, based on the slope of the least-squares line in Figure 8. The value of the well depth obtained by this procedure is 5 kcal/mole (217 meV). A plot of the final translational energy of molecules scattered into $J_f = 3$ as a function of the incident translational energy is shown in Figure 9. As noted on the figure, the graph indicates that, to within ±20%, the final translational energy is the same as the incident energy. This suggests that only a small amount of translational energy is transferred to the surface lattice, which implies that using a rigid-surface model for the calculations may not be a bad approximation for this system.

B. Results of Quasiclassical Trajectory Calculations

This section is devoted to a presentation of the results of QCT calculations on the HCl/Au system. After an introductory discussion of previous studies on the scattering of NH_3 from gold, computations involving the SP, WP and AP potentials, respectively, are described in some detail. The discussion for each potential starts by explaining how features in the calculated probability distributions at various incident energies are related to the interaction potential; then the computed Boltzmann and average final rotational energy plots for that potential are compared to the experimental ones given in Figures 7 and 8.

1. Ammonia/Gold Scattering

In their experimental study of ammonia scattering from gold, Kay and coworkers[76] observed a zero-energy rotational rainbow, that is, a large probability for scattering into states of low rotational energy. They also found a dynamic propensity for scattering into rotational states with low values of the K quantum number; such states correspond to end-over-end tumbling motion of the ammonia molecule. To qualitatively explain these results, Coltrin and Kay[75] employed a gas-surface interaction potential containing a long-range anisotropic term, plus short-range atomic potentials (exponential repulsions for the H atoms and a modified Morse for the N atom) designed to ensure that the potential minimum occurred with the nitrogen end closest to the surface and the molecular symmetry axis perpendicular to the surface. The resulting trajectory calculations showed that the long-range anisotropy serves to orient the molecule with its symmetry axis normal to the surface, leading to a "rocking" motion about this orientation. The amplitude and period of this motion decrease as the ammonia molecule approaches the surface, due to the increasing steepness of the rocking potential, so that it impacts the repulsive wall in an essentially perpendicular alignment. Since by symmetry such a collision can exert no torque around the center of mass, the molecule leaves the surface without being rotationally excited by the collision. Thus, for a large percentage of initial orientations (increasingly large as the translational energy decreases), molecules are scattered into states of low rotational energy, which leads to the experimentally-observed zero-energy

rotational rainbow. The majority of the other initial orientations, while lying so far away from the normal that there is not enough time for the molecule to be aligned completely, are also sufficiently affected by the long-range anisotropy to create the observed propensity for preferential scattering into tumbling rotational states.

Like ammonia, HCl has a "hydrogen end" and an "electron-rich" end. Hence it was thought that, as in the ammonia case, a potential having a long-range anisotropy and forcing the molecule to orient itself normal to the surface at the minimum, with the electron-rich (chlorine) end down, would adequately describe the HCl-gold interaction. Thus the "strongly perpendicular" (SP) potential discussed in Chapter III was developed, by analogy with reference 75, as an initial attempt to model the interaction potential. It was anticipated that using this potential function to govern the scattering would, by analogy to the ammonia case, produce a zero-energy rainbow due to orientation of the HCl molecule by the long-range anisotropic potential. However, it was also expected that a peak would appear in the probability distribution at some high value of the rotational quantum number, since the short-range orientational forces would cause the molecule to flip over if it approached with the hydrogen end pointing toward the surface. This behavior was observed in the calculations by Muhlhausen *et al.* on the scattering of NO from platinum and silver, in which a similar gas-surface potential was used.[86] Such a high-energy feature did not appear in the ammonia case, due to the fact that the hydrogen atoms in NH_3 do not lie on the symmetry axis. The repulsive interactions of these off-axis H atoms prevent the ammonia molecule from flipping over, so that low-torque

configurations are obtained in the case of NH_3 scattering regardless of which end of the approaching molecule is pointed toward the surface. As the discussion in the remainder of Section B will demonstrate, the fact that no such barrier to reorientation between $\theta = 0°$ and $\theta = 180°$ exists in the HCl case plays an important role in the scattering dynamics, at least for the potentials used in this work. First to be considered are the results of calculations using the SP potential, for which the NH_3/Au work just discussed served as a starting point.

2. Calculations Using the SP Potential

Figure 10 presents final rotational state distributions computed using the SP potential at various incident energies. As noted in Section B of Chapter III, the initial rotational quantum number for these calculations (as well as those discussed below involving the WP and AP potentials) was $J_i = 0$. The SP distributions largely bear out the expectations mentioned in the previous paragraph. The prominent features of the distributions are: a peak at low rotational energy (either at $J_f = 0$ or spread among the first few rotational states); a peak at higher rotational energy; and a high rotational energy "tail" of sparsely populated states. The dynamical origin of these features is discussed in the following paragraphs. To facilitate the analysis, the corresponding excitation functions, which show the quasiclassical final rotational "quantum number" J_f as a function of the initial orientation angle θ_i, are given in Figure 11.

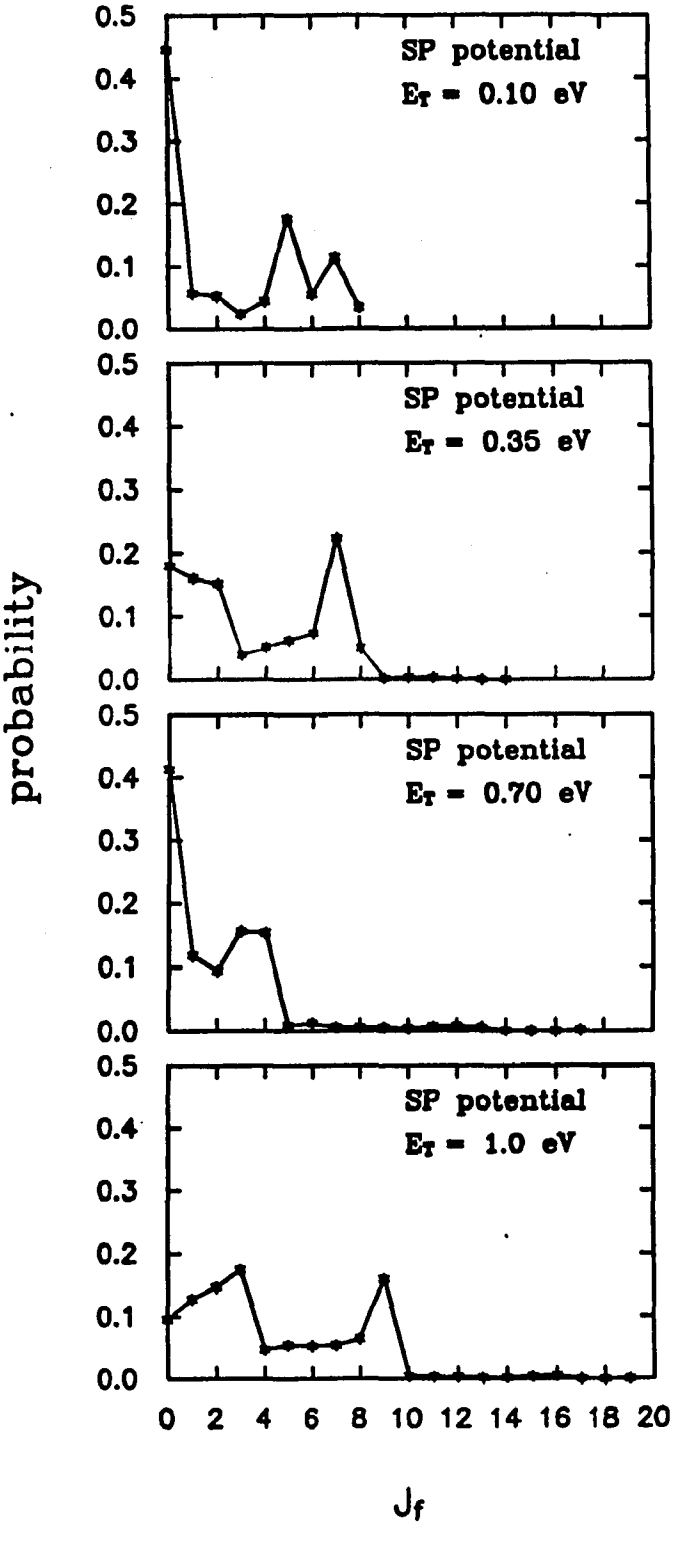

Figure 10. Final rotational state probability distributions calculated using the SP potential.

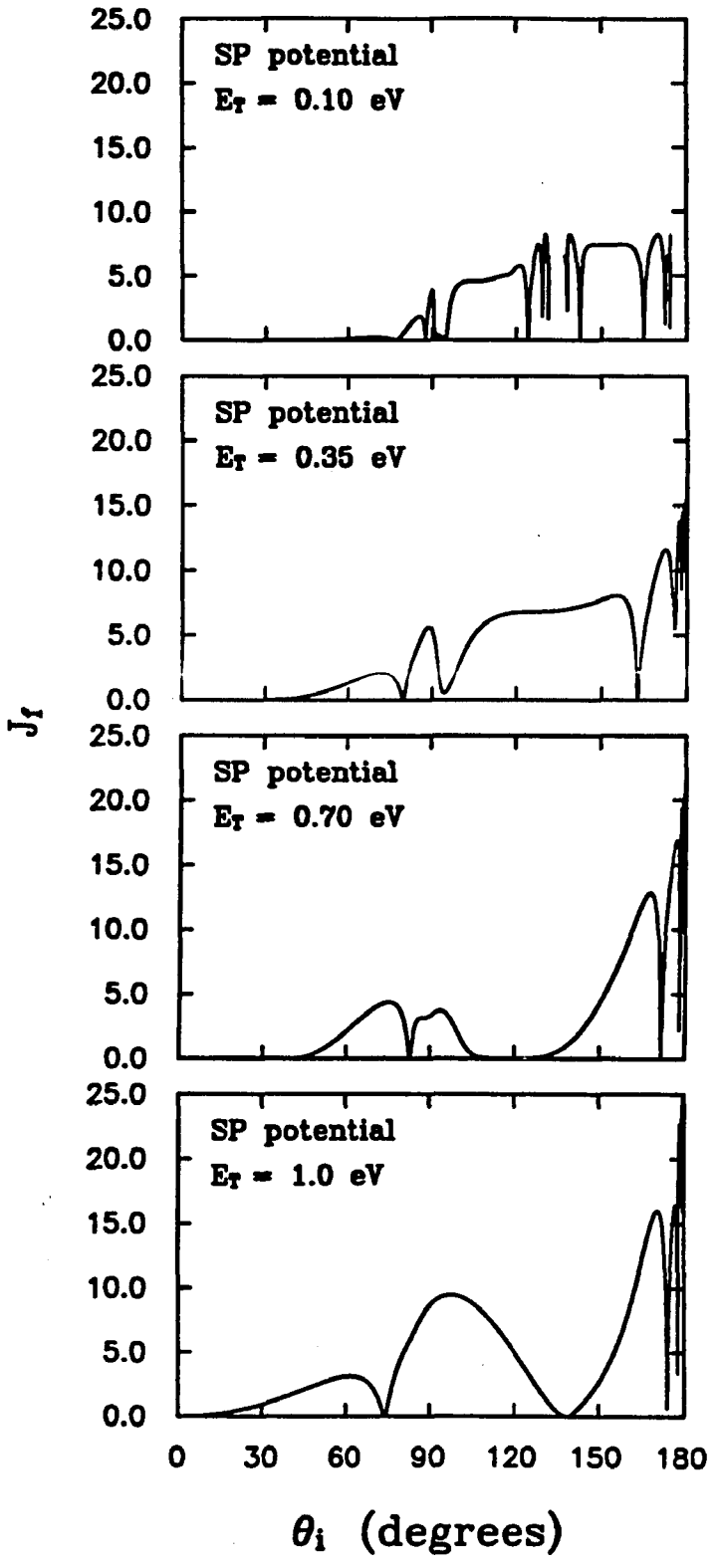

Figure 11. Excitation functions calculated using the SP potential.

The large peak at $J_f = 0$ in the distributions corresponds to a zero-energy rotational rainbow. As mentioned in Chapter I, rainbows occur whenever the excitation function has an extremum; the zero-energy rainbow arises when the extremum is a minimum having the value $J_f = 0$. As Figure 11 indicates, the excitation functions do have such minima at $\theta_i = 0°$, and, except for $E_T = 1$ eV, the rotational excitation remains very small for a large range of θ_i near 0°. (As in Chapter III, $\theta = 0°$ means that the chlorine end points directly toward the surface.) The dynamical origin of the zero-energy rainbow lies in the long-range and short-range orienting forces, which align molecules having small θ_i so that they strike the surface nearly perpendicularly with the chlorine end down. Such collisions impart only a small torque to the diatom, as the contour plot of the SP potential shows (see Figure 3, in Chapter III), leading to small rotational excitation.

As the incident energy increases, the range of initial orientation angles near 0° which leads to elastic scattering grows smaller. Thus, for $E_T = 100$ meV, the $J_f = 0$ feature is due almost entirely (90%) to trajectories having θ_i between 0°and 80°. For $E_T = 350$ meV, the corresponding range is θ_i less than 49°, and at 1 eV it shrinks to θ_i less than 23°. Two factors contribute to this effect. One of these is that as the velocity of the diatom increases, the orientational forces have less time to turn the molecule toward the low-torque configuration. Second, for a given anisotropy about the center of mass of the molecule, an impact at higher velocity creates more torque, which leads to higher excitation. The overall result is that the angle range that contributed to elastic scattering at $E_T = 100$ meV produces scattering into the first

few rotational states at higher values of E_T. This is easily seen by comparing the $0° \leq \theta_i \lesssim 80°$ portion of the excitation functions, or by looking at the low-J_f part of the rotational distributions. At E_T = 350 meV, for example, 86% of the peak at $J_f \leq 2$ arises from trajectories having initial orientations between 0° and 82°, while at E_T = 1 eV the 0° to 80° range provides 72% of the peak at $J_f \leq 3$.

Besides the alignment toward low-torque configurations, there is another dynamical effect that contributes to low rotational excitation for this interaction potential. This is the *damping* of rotational excitation of the molecule by the strong short-range orientational forces as the molecule leaves the surface after the collision. Because the potential energy increases so rapidly as θ goes from 0° to 180° (see Figure 3), molecules that are excited by the collision with the surface can in many cases lose almost all of their rotational energy as they rotate toward higher θ while the molecule leaves the surface. This is an example of the cancellation of the anisotropies of the attractive and repulsive parts of the interaction potential, which has been observed previously in close-coupling and sudden calculations.[34,41] In accord with the previous work, the degree of cancellation depends on the collision energy; nowhere is the behavior more evident than in the E_T = 700 meV case. In addition to the J_f = 0 minimum for θ_i near 0°, the excitation function for this energy shows another broad minimum for the range $104° \leq \theta_i \leq 135°$, due to damping by the short-range forces of the interaction potential. No such minimum appears in the E_T = 350 meV excitation function; at 1 eV collision energy the minimum is much narrower. Only 42% of the large J_f = 0 peak at E_T = 700 meV comes from low-torque

collisions (initial θ less than 50°); trajectories experiencing the damping effect contribute 57% to this peak. (The fact that the damped trajectories make a larger contribution, even though they come from a narrower range of initial angles, is due to the $\sin\theta$ weighting of the initial orientations in the Monte Carlo selection process.)

The peaks at higher values of J_f in the distributions of Figure 10 (in particular, $J_f = 5$ at $E_T = 100$ meV, $J_f = 7$ at $E_T = 350$ meV and $J_f = 9$ at $E_T = 1$ eV) are rainbow peaks which arise not from an interaction with the repulsive part of the potential, but rather from rotational excitation of the HCl molecule by the short-range orienting forces as the molecule leaves the surface. In these cases, the details of the trajectory before and during the collision with the surface are such that the molecule stops rotating while still close enough to the surface that the short-range forces can impart to it significant rotational excitation as it recedes. Trajectories exhibiting this behavior contribute 86%, 97% and 98%, respectively, to the three peaks listed at the start of this paragraph. It should also be noted that the range of θ_i producing the $J_f = 7$ peak at $E_T = 350$ meV (114° to 147°) is nearly twice as large as that contributing to $J_f = 5$ at $E_T = 100$ meV (101° to 119°) or to $J_f = 9$ at $E_T = 1$ eV (90° to 107°), while the actual number of trajectories is only greater by about 40 percent. Again, this reflects the $\sin\theta$ weighting of the initial orientation angles. The peak at $J_f = 3$ and 4 in the $E_T = 700$ meV rotational distribution is due primarily to two contributions, which correspond to the two humps in the $E_T = 700$ meV excitation function between $\theta_i = 50°$ and $\theta_i = 105°$. The leftmost of these humps, which accounts for 50% of the scattering into $J_f = 3$ and 4,

lies in what has earlier been referred to as the low-torque regime ($\theta_i \lesssim 80°$); the right-hand hump, which contributes 42%, is in the same range of θ_i (between 85° and 98°) from which the rainbow peaks just described for the other collision energies originate. The fact that the rainbow due to rotational excitation by the short-range forces occurs in this instance at such a small value of J_f (commensurate with the low-torque excitation) is another manifestation of the greater degree to which the anisotropies cancel at this collision energy.

The remaining outstanding feature of the distributions in Figure 10 is the "tail" of sparsely populated rotational states of high energy. Trajectories ending up in these final rotational states begin with the HCl molecule oriented such that the hydrogen end is pointed almost directly toward the surface (initial θ greater than 143, 167, 150 and 162 degrees at E_T = 100, 350, 700 and 1000 meV, respectively). These molecules are rotated toward, or in some cases, past θ = 180° by the long-range orienting forces, until the molecule is about 4 Å from the surface. At this point the short-range forces take over, rotating the diatom strongly toward the chlorine-end-down arrangement. However, the resulting rotation is so fast that after the θ = 0 point has been passed the short-range forces cannot stop the rotation completely. Thus the hydrogen end of the molecule has a strong repulsive interaction with the surface, which sends it rotating the other direction toward another hard-wall interaction. This kind of motion is called "chattering".[62] As the molecular center of mass approaches and leaves the surface, the molecule may experience three or more such chattering collisions. The final angular momentum imparted to a molecule which chatters is very

sensitive to the initial orientation, as evidenced by the complicated structure (many extrema) of the excitation functions in Figure 11 for the appropriate range of angles. Similar excitation functions were calculated by Polanyi and Wolf[62] for HF/surface scattering using a model repulsive potential. The extrema in the excitation function, which produce singularities in the probability distribution, account for the peaks in the tail of high-J_f states, such as $J_f = 12$ at $E_T = 700$ meV and $J_f = 16$ at $E_T = 1$ eV. Overall, the states arising from the chattering behavior are sparsely populated, since the corresponding trajectories are less probable due to the $\sin\theta$ weighting of initial orientations. It is evident that the multiple encounters with the surface ultimately limit the amount of rotational excitation which can be obtained for the SP potential, since the highest rotational state populated is lower than that allowed by energy conservation at each of the collision energies used here except the lowest, 100 meV. At this energy the scattering into $J_f = 7$ and 8 is due to chattering collisions. The peak at $J_f = 7$ is due to the "plateau" at $144° \leq \theta_i \leq 163°$ in the $E_T = 100$ meV excitation function. The population in $J_f = 8$ is reduced relative to $J_f = 7$ due to a trapping cutoff.[61,62] In this case, the diatom acquires so much rotational energy during the collision that not enough is left in translation to escape the potential well. The molecule is temporarily trapped in the well until a subsequent interaction with the surface transfers enough energy back into translation that the molecule can escape. The net result of this *rotational trapping* is to convert the highest J_f state into a random distribution of rotational states whose average J_f is smaller. The portions of the excitation function where the curve is

broken correspond to the θ_i regions leading to rotational trapping ($130° \leq \theta_i \leq 140°$ and $\theta_i \geq 173°$).

In order to discover how important the long-range orientational forces are in these calculations, sets of trajectories were run at the same incident energies as above, with the anisotropy constant E in the long-range term of the potential, equation (3.15), set to zero. The resultant probability distributions are presented in Figure 12. At the higher incident energies, 700 meV and 1 eV, the distributions are essentially the same as those in Figure 10. The major features are located in the same places, with differences only in the relative heights of peaks. For example, at $E_T = 1$ eV, the scattering into $J_f = 0$ drops by 40 percent, and the low-energy peak is at $J_f = 2$ instead of $J_f = 3$; at $E_T = 700$ meV, the $J_f = 0$ peak loses some intensity to $J_f = 1$ and 2, while $J_f = 4$ grows at the expense of $J_f = 3$. At the lower incident energies, especially at 100 meV, the changes are more pronounced, which is not surprising since at the lower velocities the long-range forces have more time to exert their influence on the molecule. At $E_T = 350$ meV, the most noticeable changes after turning off the long-range anisotropy are that the population of the $J_f = 1$ state grows at the expense of those at 0 and 2, and that the peak at $J_f = 7$ spreads out among $J_f = 5$ through 7. At $E_T = 100$ meV, significant changes occur. Over half of the trajectories from the low-torque orientation range which gave elastic scattering in the presence of the anisotropy contribute to $J_f = 1$ in its absence; also, over half of the orientations that contributed to the peak at $J_f = 5$ now lead to trajectories experiencing damping by the short-range forces, which yield $J_f = 0$. The large peak at $J_f = 4$ without the long-range forces

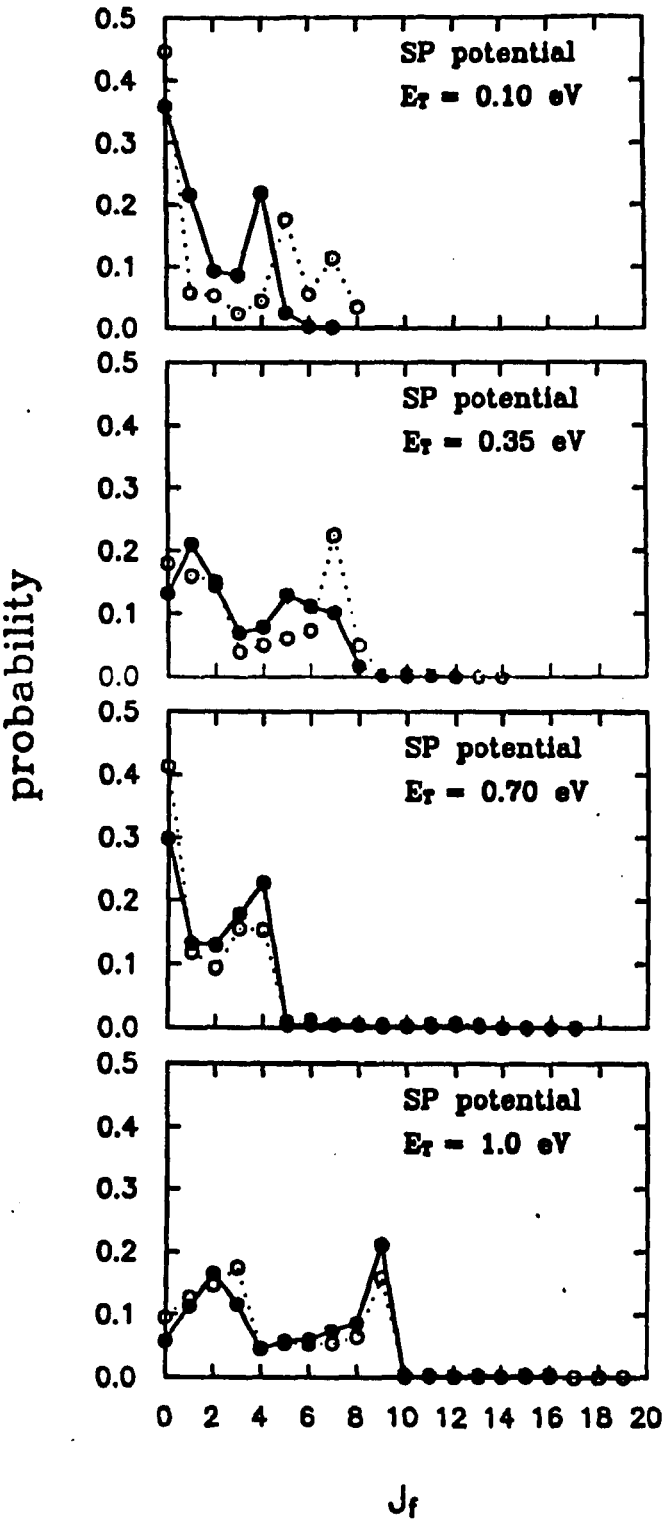

Figure 12. Effect of turning off the anisotropy of the long-range part of the SP potential. The filled circles give the no-anisotropy distribution; the open circles give the distributions from Figure 10 for the full potential.

comes mostly from the range of orientations that formerly yielded the peak at $J_f = 7$. A consistent theme underlying all these changes is that the scattering into states both at $J_f = 0$ and at the highest values of J_f decrease in favor of scattering into states having intermediate J_f values. This is easily explained by the fact that the long-range anisotropy rotates the HCl molecule toward normal alignments ($\theta = 0$ or 180°), which lead to the production of the lowest or highest final rotational states. Similar observations were made by Coltrin and Kay[75] in their study of ammonia/gold scattering.

Boltzmann plots for the rotational distributions calculated using the SP potential are presented in Figure 13. A comparison of these with the experimental ones in Figure 7 clearly demonstrates that the SP potential does not accurately reflect the true potential. The numerous features in the calculated plots are absent in the experimental plots, and the variation of the calculated populations as the rotational energy is increased covers twice as many orders of magnitude as that for the experimental results. Figure 14 contains a plot of the average final rotational energy of the SP distributions versus the incident energy. The slope of the least-squares line describing the calculated results has a slope of 0.016, compared to 0.08 for the slope of the experimental fit. This reflects an overestimation of elastic and nearly elastic scattering by the SP potential, compared to the actual gas-surface interaction.

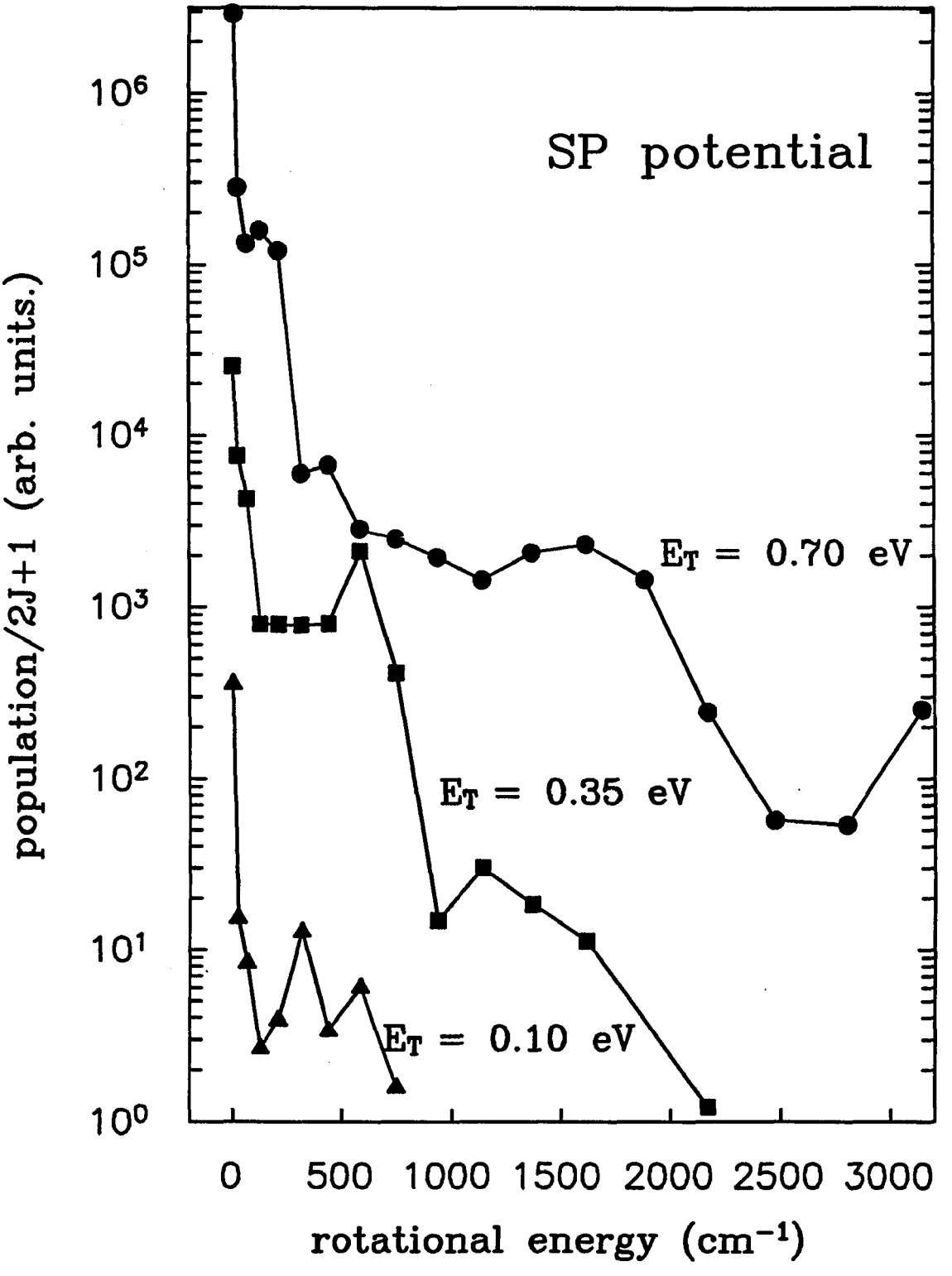

Figure 13. Rotational Boltzmann plots for the SP potential.

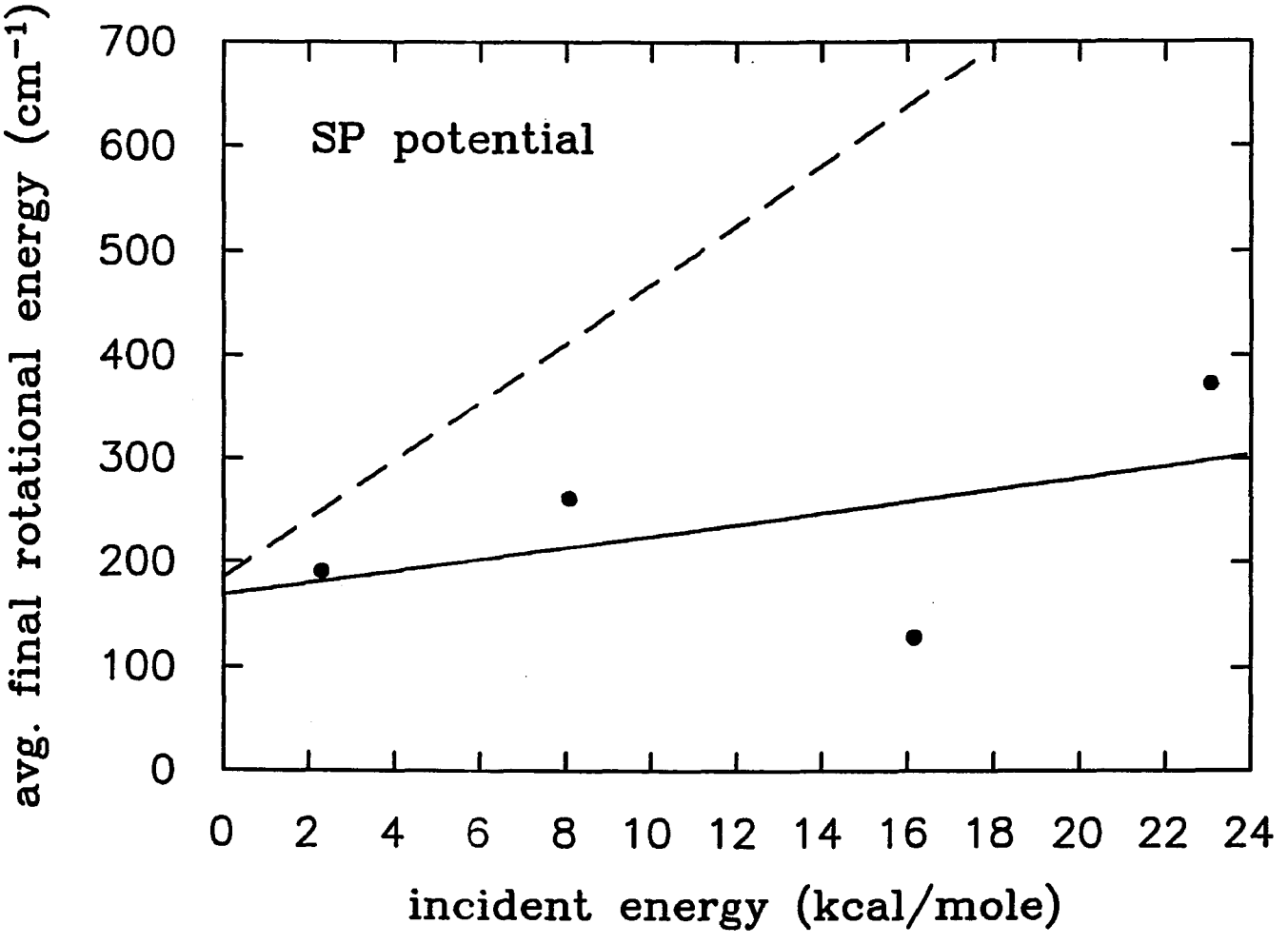

Figure 14. Dependence of the average final rotational energy on the incident translational energy for the SP potential. The solid line is a least-squares fit to the calculated results; the broken line is the least-squares fit to the experimental data from Figure 8.

3. Calculations Using the WP Potential

Since the potential initially chosen to represent the HCl-gold interaction did not yield results in accordance with the experimental data, a second one was developed and tested. This is the "weakly perpendicular" (WP) potential. Because the short-range forces seemed to play the dominant role in the SP case, this was the part of the interaction potential which was changed. As discussed in Chapter III, the magnitude and extent of the short-range orienting forces has been greatly reduced in the WP potential compared to the SP, and the anisotropy of the repulsive wall is much less. The final rotational state distributions resulting from the WP potential are presented in Figure 15, and Figure 16 contains the corresponding excitation functions. The most striking features of the distributions in Figure 15 are the prominent $J_f = 0$ peaks that appear at the lower two incident energies, and the relative smoothness of the distributions, particularly for collision energies above 100 meV. These characteristics are discussed in the following paragraphs.

For $E_T = 100$ and 350 meV, there is a peak at $J_f = 0$, corresponding to a zero-energy rotational rainbow. As indicated by the excitation functions for these incident energies, the peak in the $E_T = 100$ meV distribution is due entirely to initial orientations having $\theta_i \leq 84°$, while at $E_T = 350$ meV it comes from the range $\theta_i \leq 53°$. At the higher incident energies, the peak in the probability distribution at $J_f = 0$ has disappeared, but the excitation functions do show that $dJ_f/d\theta_i = 0$ at $\theta_i = 0°$, indicating the presence of a rainbow. This is manifested by

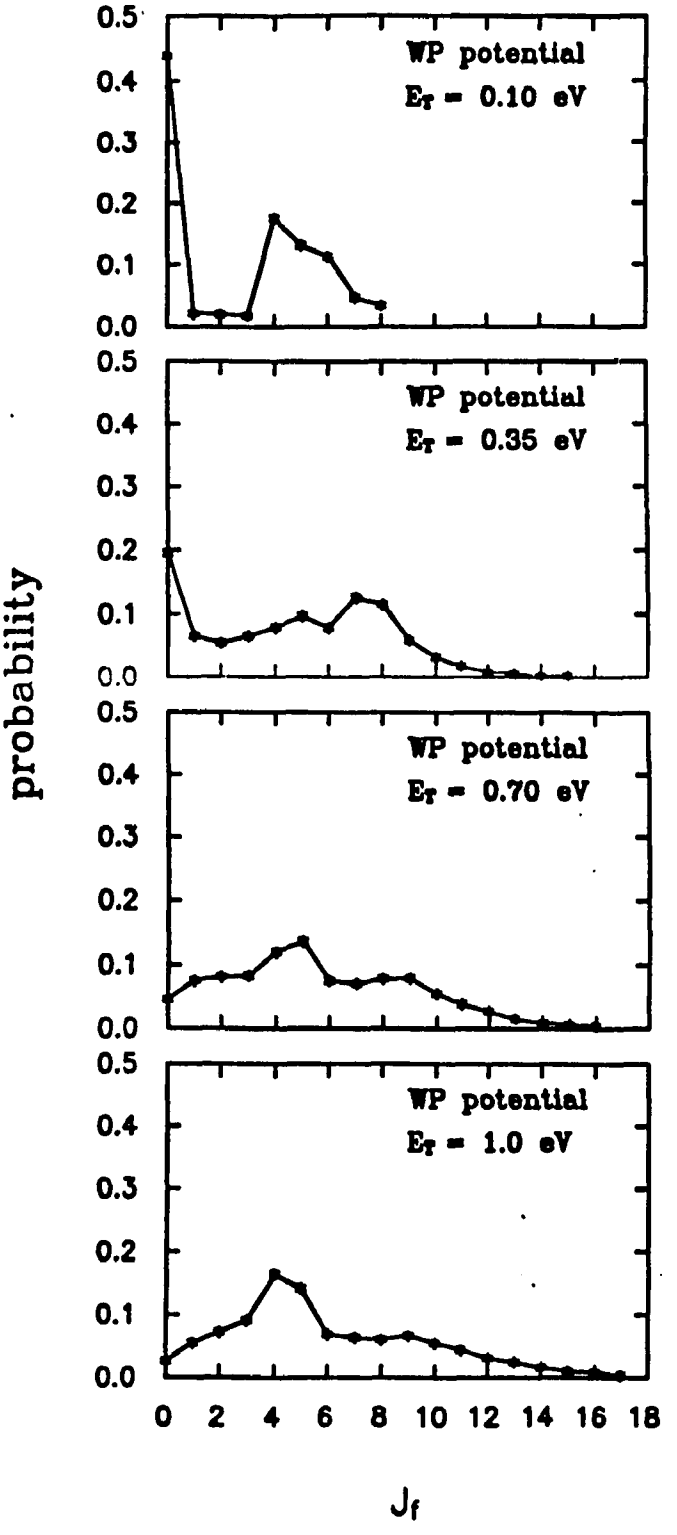

Figure 15. Final rotational state probability distributions calculated using the WP potential.

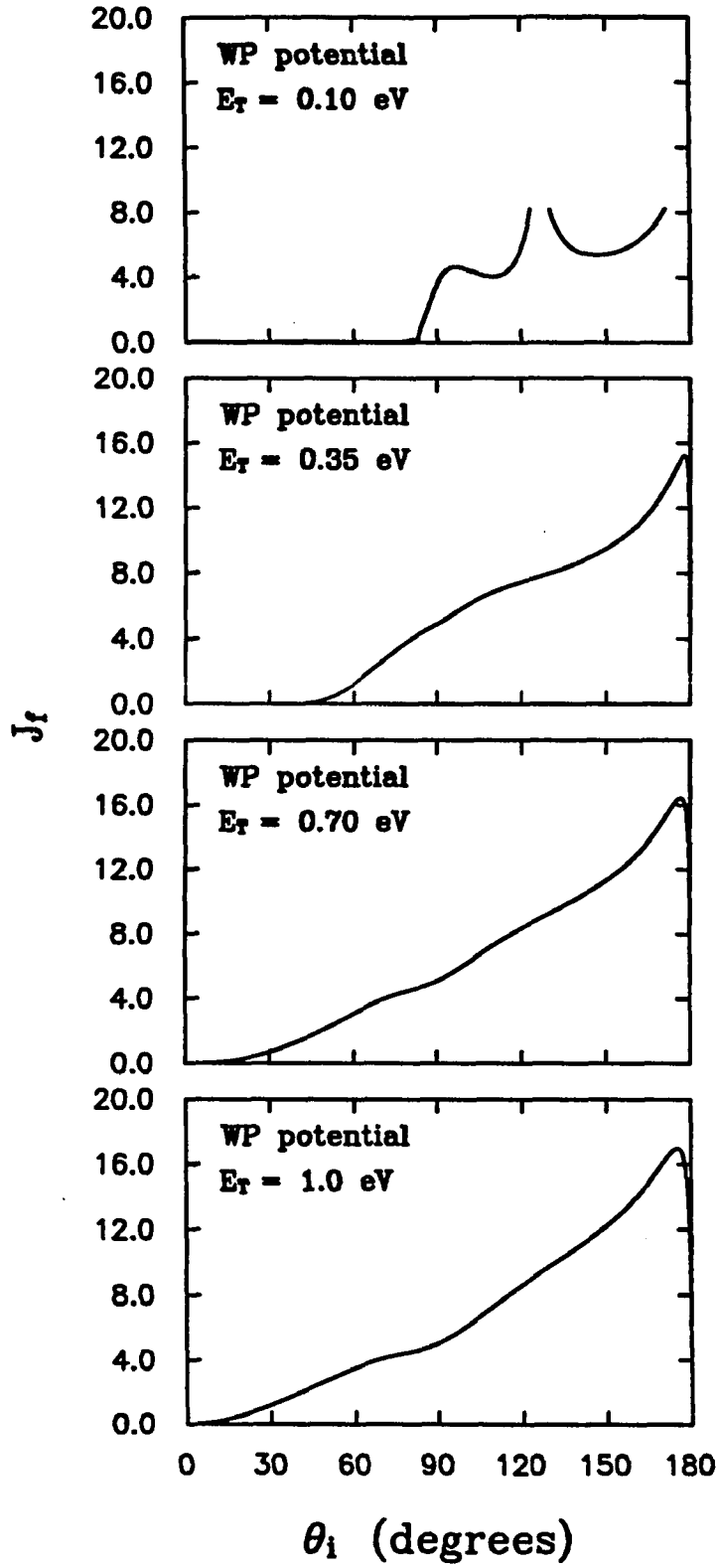

Figure 16. Excitation functions calculated using the WP potential.

the peaks at $E_R = 0$ in the Boltzmann plots at these energies, shown in Figure 17. The orientations contributing to $J_f = 0$ scattering at $E_T =$ 700 meV and 1 eV are those having θ_i less than 26° and 19°, respectively. The reasons that the range of orientations leading to elastic scattering steadily decreases as the incident energy increases are the same as for the SP calculations: orienting forces have less time to work as the incident energy increases, and more torque is exerted at higher collision energies for a given anisotropy.

The decreased strength and range of the short-range orienting forces in the WP potential manifest themselves by the relative smoothness of the final state distributions; absent are the abrupt peaks at higher values of J_f which appeared in the SP case. Those sharp features arose in the previous calculations because of the competing tendencies of the strong short-range forces of the SP potential to damp and excite rotation. In the present calculations, however, the weaker short-range forces contribute *only* to rotational excitation, for trajectories having initial orientation angles greater than the cutoff for scattering into $J_f = 0$. This occurs because outside of the $J_f = 0$ range, the short-range forces, which act less strongly over a shorter distance than in the previous case, cannot spin the molecule all the way to $\theta = 0$ degrees before it collides with the surface. Consequently, not only does the diatom strike the repulsive wall with a geometry that excites rotation toward the normal, but it continues to be rotated toward $\theta = 0$ by the short-range forces as it recedes from the surface (see the contour plot of the WP potential, Figure 4, in Chapter III). Even if the molecule passes the perpendicular configuration after the impact, the net effect

of the short-range forces is to enhance any rotational excitation created by the collision with the hard wall. The contributions to rotational excitation created by the orientational forces and by the impact with the repulsive wall both increase uniformly as the initial orientation increases, for all the incidence energies used except 100 meV; the shapes of the excitation functions for these energies reflect this fact. The result of this uniform behavior is a relatively smooth variation of the distribution of final J states. The maxima at intermediate J values are due both to the deviations of the excitation functions from linearity and to the fact that these states are produced from trajectories having initial orientations near $\theta = 90°$, where $\sin\theta$ is largest.

The considerations of the previous paragraph apply in general to the $E_T = 100$ meV case, although matters are complicated somewhat by the stronger influence of the orienting forces at this energy, as well as by the fact that trajectories starting with θ_i greater than about 130° are rotated past $\theta = 180°$ by the long-range orienting forces. The more pronounced structure in the $E_T = 100$ meV excitation function results from this added complexity. The two extrema in the excitation function between $\theta_i = 90°$ and $\theta_i = 120°$, which contribute to the peak in the distribution at $J_f = 4$ and 5, arise from competing excitation and damping of rotation as the molecule leaves the surface. The structure of the excitation function for $\theta_i \gtrsim 120°$ is due to the effect of the long-range orienting forces of the potential. As mentioned above, the short-range forces of the WP potential produce rotational excitation, the magnitude of which depends on the orientation of the diatom when these forces become dominant (at roughly 4 Å above the surface). As θ_i increases from

120°, the long-range forces have rotated the molecule to near $\theta = 180°$ by the time it reaches 4 Å, so that the rotational excitation increases dramatically, finally leading to rotational trapping. As θ_i continues to increase, J_f decreases to a minimum value (at $\theta_i = 148°$), since the molecule rotates past $\theta = 180°$ on approach, and has some smaller value of θ when it reaches 4 Å. Finally, as θ_i approaches 180°, the orienting forces at long range become very weak, so that again the molecule has θ nearer to 180° at 4 Å, and the rotational excitation increases. The large population in $J_f = 6$ is due to the minimum at $\theta_i = 148°$; the population in $J_f = 8$ is cut off by the rotational trapping, as it was for the SP potential at $E_T = 100$ meV.

Comparing the Boltzmann plots for the WP potential, in Figure 17, with the experimental results from Figure 7 shows a few similarities, particularly between the $E_T = 700$ meV plot in Figure 17 and the $E_T = 14.2$ kcal/mole (616 meV) plot in Figure 7. These are both relatively linear at higher rotational energy, and show a small peak near $E_R = 0$. Also, the WP result shows about the same number of populated states ($J_{max} = 16$) as the experiment ($J_{max} = 15$). However, the slope of the calculated plot is greater in magnitude than the experimental one, indicating that the overall rotational excitation is not as great for the calculated distribution. This is consistent with the fact that the plot of the average final rotational energy versus incident energy for the WP potential, given in Figure 18, shows that this interaction generally underestimates the rotaotational excitation produced by higher collision energies. Examination of the contours of the WP potential in Figure 4 shows that this underestimation occurs because the repulsive wall

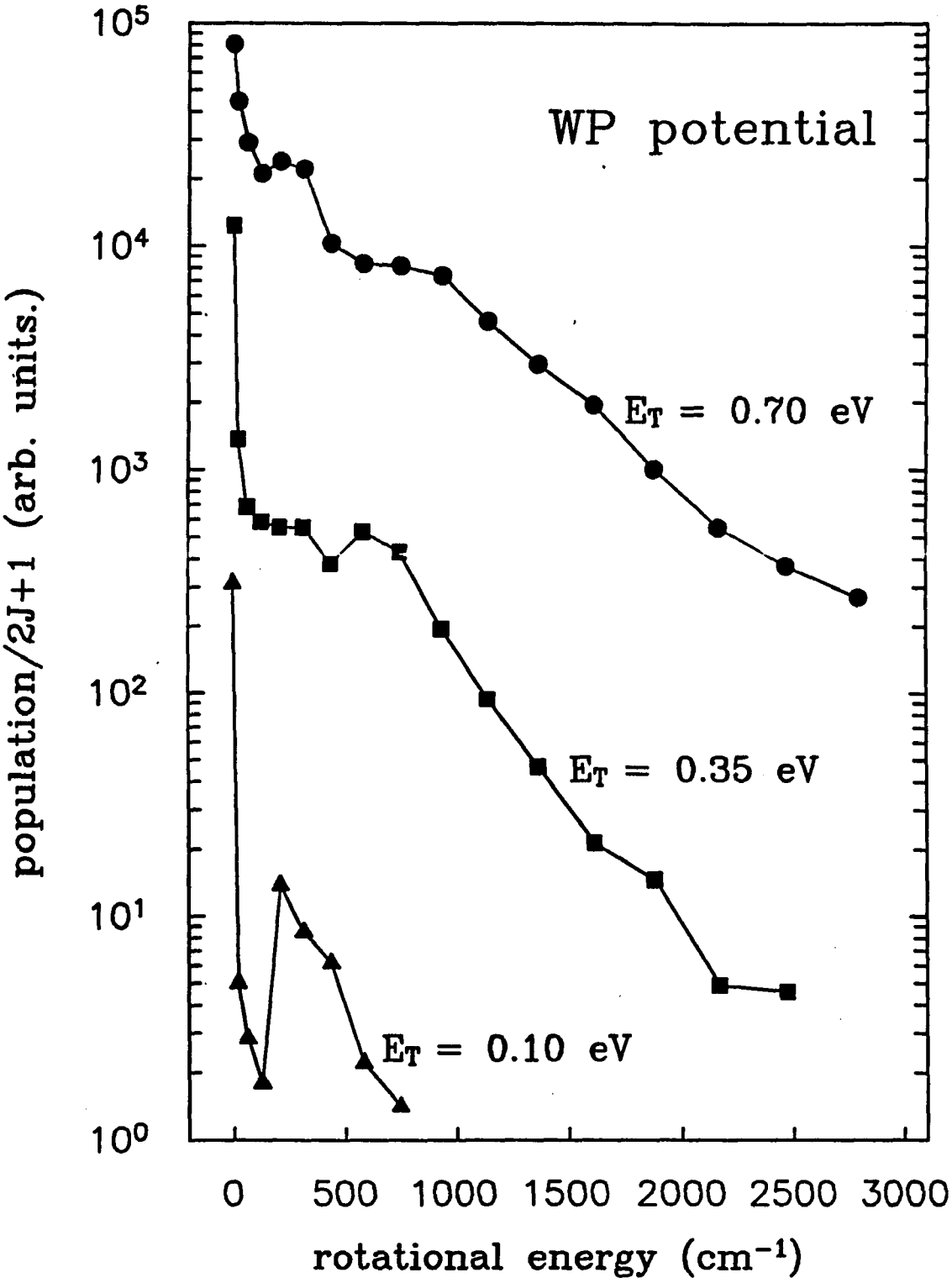

Figure 17. Rotational Boltzmann plots for the WP potential.

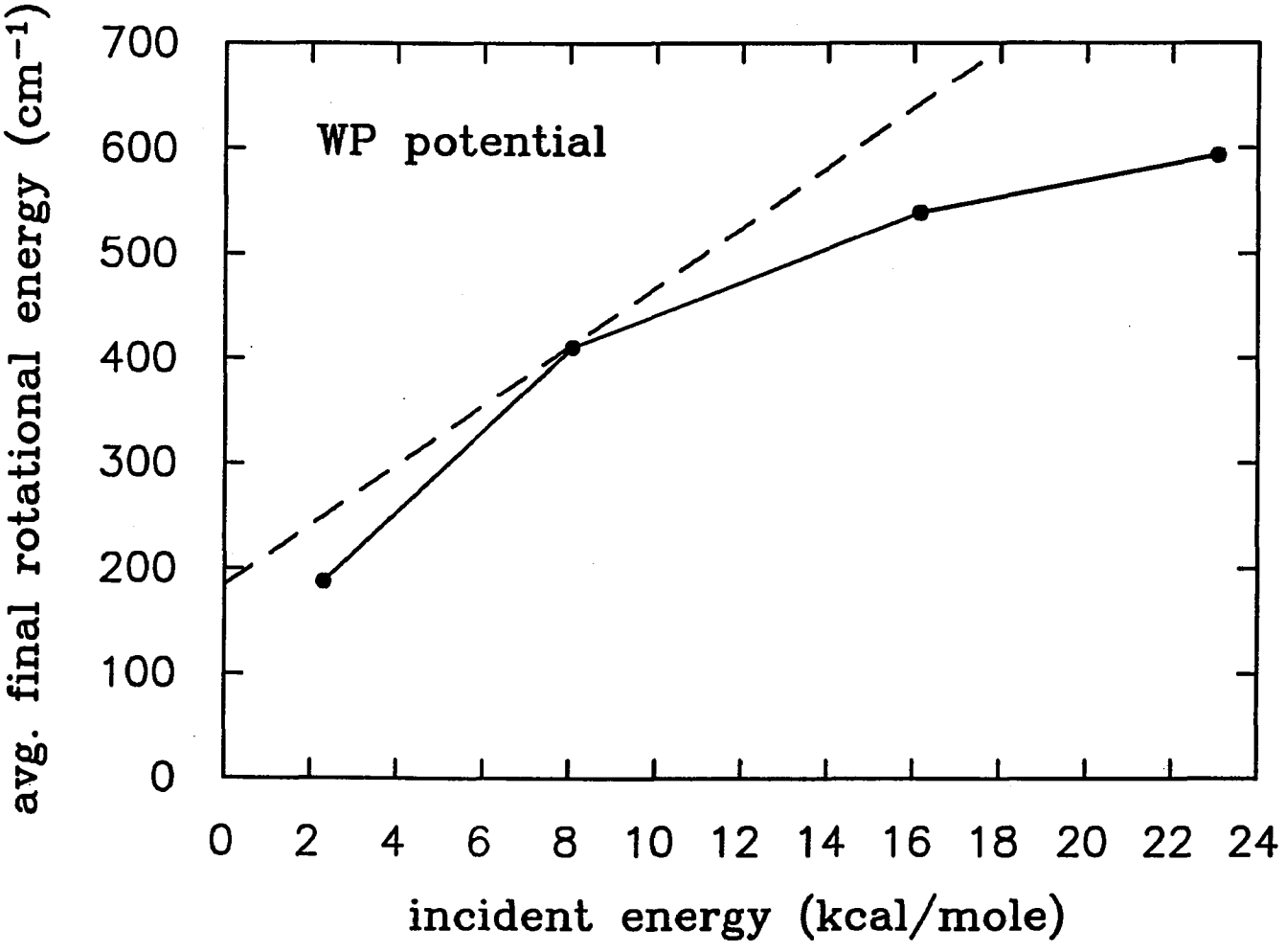

Figure 18. Dependence of the average final rotational energy on the incident translational energy for the WP potential. The broken line is the least-squares fit to the experimental data in Figure 8.

becomes more isotropic as the energy increases.

Boltzmann plots for the lower incident energies are less similar to the experimental results, most notably in the large zero-energy peak which appears in the calculated plots but not the experimental ones. Both the SP and WP potentials, for which the equilibrium geometry has the molecule normal to the surface with the chlorine end down, predict that the zero-energy peak should increase as the collision energy decreases; the same observation was made in the case of NH_3/gold scattering.[75] In each of these cases, this behavior occurs because the forces which orient the molecule into the low-torque perpendicular configurations become more influential as the collision energy decreases. The fact that the magnitude of the zero-energy peak in the experimental results for HCl decreases as the collision energy decreases suggests that the true potential may be one in which the equilibrium geometry is not the low-torque normal orientation. To test this possibility, the "almost parallel" (AP) potential was developed and applied in trajectory calculations.

4. Calculations Using the AP Potential

Probability distributions and excitation functions calculated using the AP potential are shown in Figures 19 and 20. For the three energies 350 meV, 700 meV and 1 eV the distributions are remarkably similar. Each has a slight peak at $J_f = 0$, a larger feature at low J_f and a large peak at high J_f. The qualitative similarity of the excitation functions for these three incident energies indicates that the dynamical origin of

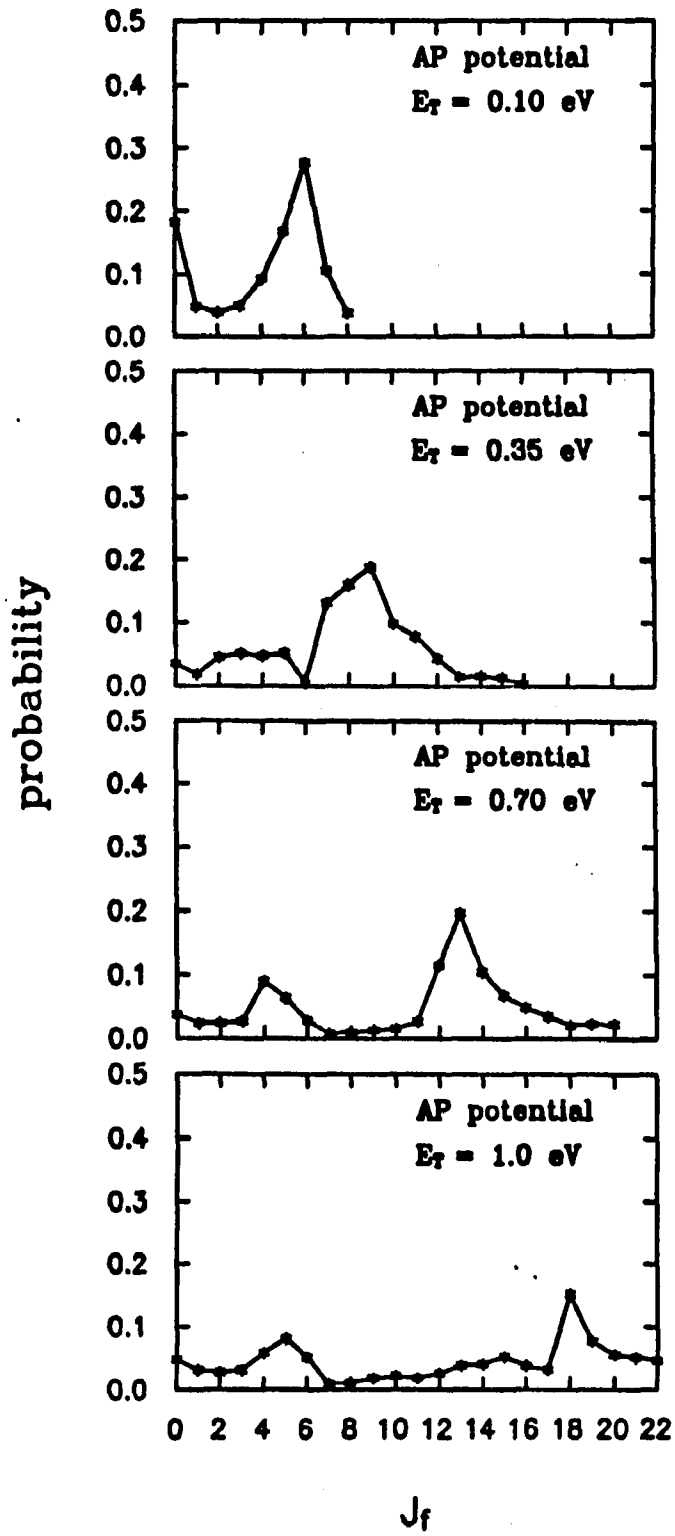

Figure 19. Final rotational state probability distributions calculated using the AP potential.

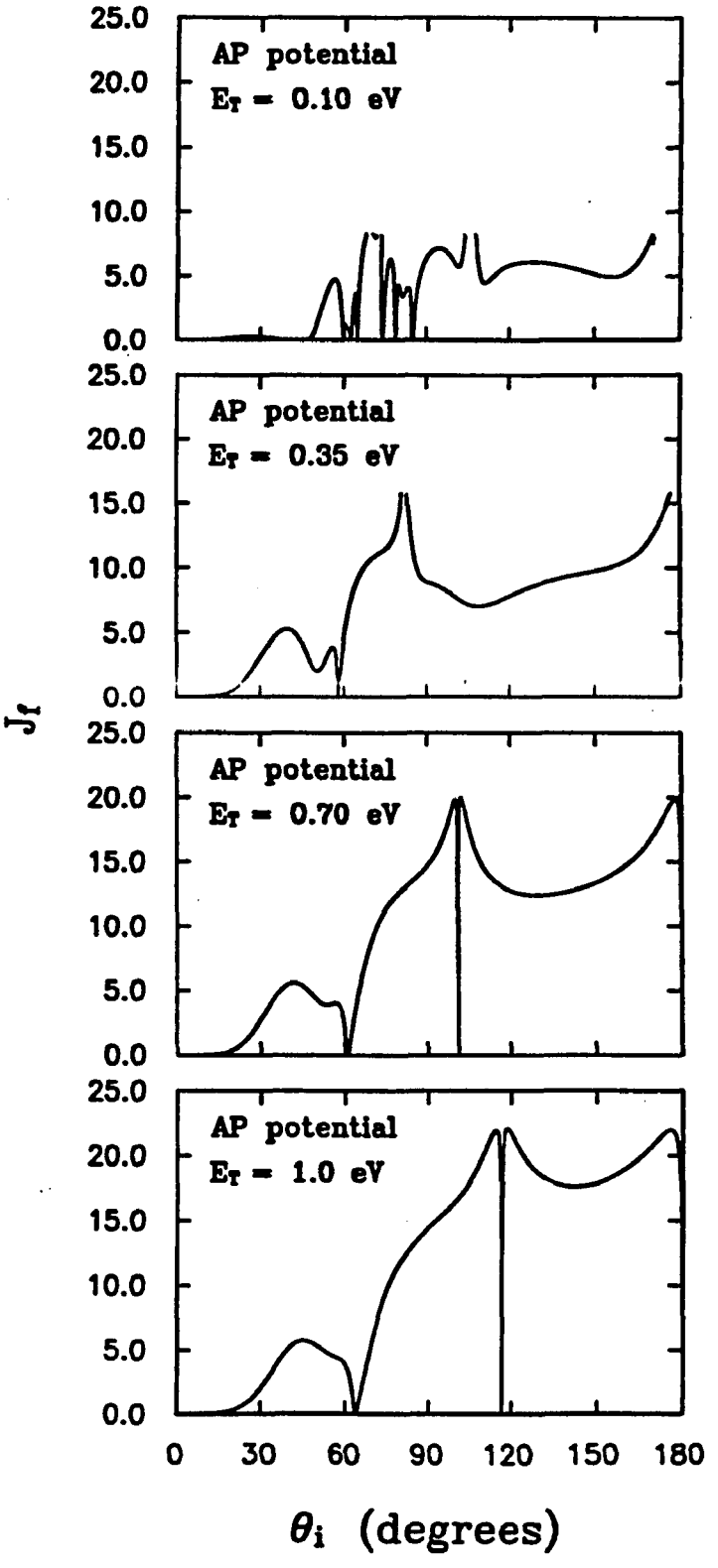

Figure 20. Excitation functions calculated using the AP potential.

each of these features is the same in each case. The dynamics at E_T = 100 meV, while similar in some ways to that at the higher energies, is again complicated by the increased effects of the attractive portion of the potential. In the following discussion, the behavior of the higher energy scattering will be considered first, then that at E_T = 100 meV.

For collision energies greater than or equal to 350 meV, the slight peak in the distributions at $J_f = 0$ reflects, as before, a zero-energy rotational rainbow at $\theta_i = 0°$. The excitation functions show that the largest contribution (82% on average) to the population in $J_f = 0$ is due to trajectories having $\theta_i \lesssim 21°$. As seen in the contour plot in Figure 5, the AP potential in this region is almost completely independent of angle (the contour lines are parallel to the θ axis). Thus, in these trajectories the molecules experience essentially no torque, and are not rotationally excited.

The structured hump at $21° \lesssim \theta_i \lesssim 60°$ in the excitation functions for each of these collision energies causes the rainbow feature in the probability distributions at low rotational energy (J_f = 4,5,6). This hump is due to the attractive part of the potential, as evidenced by the fact that the same rotational excitation is obtained for the different incident energies. As θ_i increases from 21°, the molecule receives a small amount of rotational excitation as it approaches the surface, because the potential rotates it toward larger θ at intermediate and short distances above the surface. Since the hard wall is still fairly isotropic in this angle range, the diatom gains essentially no angular momemtum from the collision with the surface. As it recedes from the surface it adds more rotational excitation as it passes over the deepest

part of the potential well. The maximum classical J_f acquired by the HCl through this process is about 5.5; this occurs for $\theta_i = 40°$ at 350 and 700 meV incident energy, and $\theta_i = 45°$ for 1 eV. For initial angles larger than those which lead to the maximum, the molecule receives enough angular momentum that it spins past 180° while still close enough to the surface that the deeper part of the potential well begins to slow the rotation. The shoulder on the hump in the excitation functions as θ_i approaches 60° occurs because the molecules begin to feel the anisotropy of the repulsive part of the potential. For trajectories having $\theta_i = 58°$, 61° and 64° at 350 meV, 700 meV and 1 eV, respectively, the approaching diatom is spun around by the orienting forces of the potential far enough that it strikes the repulsive wall with $\theta \approx 100°$. At this orientation, the anisotropy of the repulsive wall is sufficient to impart a torque in the direction opposite to the rotation of the molecule which is strong enough to stop the rotation. Thus a small range of initial orientations near 60° for each of these incident energies yields elastic scattering; this contribution makes up the rest of the peak at $J_f = 0$.

The rainbow peak at high J_f in the distributions for $E_T = 350$ meV and above is caused by trajectories having initial orientation angles greater than the range near 60° which leads to elastic scattering. These trajectories lead to relatively high rotational excitation because the HCl molecule strikes the surface with the hydrogen end down, that is, with orientations for which the repulsive wall of the potential is most anisotropic according to Figure 5. The shape of excitation functions for $\theta_i \gtrsim 60°$ bears a strong qualitative resemblance to that for $\theta_i \gtrsim 120°$ in

the E_T = 100 meV SP excitation function (see Figure 16); it has a broad minimum between two narrow maxima. In the SP case, this shape was due to how the long-range forces had oriented the molecule at the point where the short-range orienting forces take effect. For the AP potential, the structure is determined by how the long- and short-range orienting forces (both of which rotate the HCl toward θ = 180°) have oriented the molecule by the time it strikes the repulsive wall. Thus, as θ_i increases from 60°, the molecule is spun about on its approach to the surface, so that it strikes the repulsive wall with higher and higher values of θ and therefore receives increasing amounts of angular momentum from the collision. For some initial orientation range (81°-83° at 350 meV, 99°-103° at 700 meV and 113°-120° at 1 eV), the collision occurs with the H atom pointed almost directly at the surface. These trajectories impart the largest amount of angular momentum possible to the diatom and produce the largest values of J_f, namely 22 at 1 eV, 20 at 700 meV and 16 (the energy conservation limit) at 350 meV incident energy. In fact, at 350 meV so much rotation is excited that rotational trapping occurs. Past this small interval leading to the maximum excitation, the molecule on approach spins past 180° before striking the surface, so that as θ_i increases, the H atom is pointed less and less directly toward the surface on impact, resulting in decreasing values of J_f. This produces the broad minimum in the excitation function, which is the source of the large rainbow in the distributions. Finally, as θ_i approaches 180°, the molecule begins again to strike the surface with θ = 180°, since the orienting forces become weaker. The value of the minimum J_f obtained in this process decreases with decreasing collision energy, since the

orienting forces have more time to operate on the slower molecules, pushing them further past 180°. Consequently, the resulting rainbow feature is collision-energy dependent, and largely determines the magnitude of the mean rotational excitation as a function of collision energy. It should also be noted that the maxima which sandwich the minimum in the excitation function give rise to a rainbow at the highest rotational states in the distribution, when E_T = 700 meV or 1 eV; at E_T = 350 meV the trapping cutoff at J_f = 16 is clearly evident.

The probability distribution for E_T = 100 meV appears very regular in shape, but the various features in it are a much more complicated function of θ_i than those in the distributions for larger translational energy. The added complexity of the excitation function for this collision energy is a consequence of the lower velocity of the incoming molecule, which makes it more strongly influenced by the orientational forces of the potential well at both long and short range, and which enables multiple interactions with the hard wall of the potential. This latter behavior did not occur for the AP potential at the higher incident energies discussed above. Some parts of the E_T = 100 meV excitation function, namely the $\theta_i \leq 74°$ and $\theta_i \geq 104°$ regions, are qualitatively similar to those for the higher energies, and give rise to the same features in the probability distribution. The $\theta_i \leq 74°$ range contains a low-excitation region ($\theta_i < 49°$) which causes the zero-energy rainbow; a maximum due to excitation by the attractive part of the potential (at θ_i = 56°), which contributes to the population in J_f = 5; and a sharp increase in the rotational excitation, leading to rotational trapping. The $\theta_i \geq 104°$ part of the excitation function shows a broad region of

decreased excitation sandwiched by two narrow ranges of θ_i which lead to rotational trapping. All of these features have analogues in the E_T = 350 meV excitation function, and similar dynamical origins. The value of J_f in the $110° \lesssim \theta_i \lesssim 160°$ region ranges between 4.4 and 6; thus, the large peak at high J_f in the probability distribution for E_T = 100 meV represents a merging of the low- and high-J_f rainbows observed at the higher incident energies.

The complicated structure of the E_T = 100 meV excitation function between the rotational trapping features at θ_i = 74° and 108°, which has no analogue at the higher energies, arises from multiple encounters with the surface. For $\theta_i > 74°$, so much rotation is imparted to the diatom during the initial collision that before it moves away from the surface the hydrogen end grazes the surface again. The second contact with the surface is not sufficient to make the diatom chatter, but converts enough rotation back to translation that it is not rotationally trapped. This type of multiple interaction, in which the direction of rotation does not change, is called "cartwheeling".[62] For trajectories with initial orientation angles in the range 74° to 108°, the effects of cartwheeling collisions and excitation and damping of rotation by the potential well combine to make the value of J_f a complicated function of θ_i, having various maxima and minima. These trajectories contribute to scattering into essentially all the possible J_f values, including 7% of the scattering into J_f = 5 and 18% of that into J_f = 6. Cartwheeling and potential well effects also complicate the stucture of the excitation function in the broad "minimum" at high θ_i. At E_T = 100 meV, this feature is actually composed of two minima and a maximum, rather than a

single minimum as at higher collision energies.

In Figure 21 the plot of average final rotational energy versus incident energy for the AP potential is presented. The translational-to-rotational energy transfer is seen to be linear, but its magnitude of roughly 27% (the slope of the least-squares line) is considerably larger than that obtained from the SP and AP potentials, and is much too high compared to the experimental results in Figure 8. This is not surprising in view of the maximum values of J_f attained and the large peaks at high J_f in each of the distributions of Figure 19. The rotational state distributions calculated for the AP potential are markedly non-Boltzmann, as the Boltzmann plots in Figure 22 demonstrate, and bear little resemblance to the experimental distributions. As mentioned at the end of the discussion on the WP calculations, the AP potential was employed to see whether the magnitude of the zero-energy rainbow would be decreased if the equilibrium geometry has the HCl parallel to the surface. Comparison of the AP probability distributions in Figure 19 with those in Figures 10 and 15 shows that the zero-energy peak at E_T = 100 meV is halved in the AP results compared to the others; however, the peak still increases as the collision energy decreases. Furthermore, constraining the potential minimum to occur at a parallel geometry introduces short-range aligning forces which, for large numbers of initial orientations, cause the HCl to strike the surface with the hydrogen end down, in the maximum-torque configuration. This produces the significant overestimation of the average rotational excitation for the AP potential compared to the experimental results.

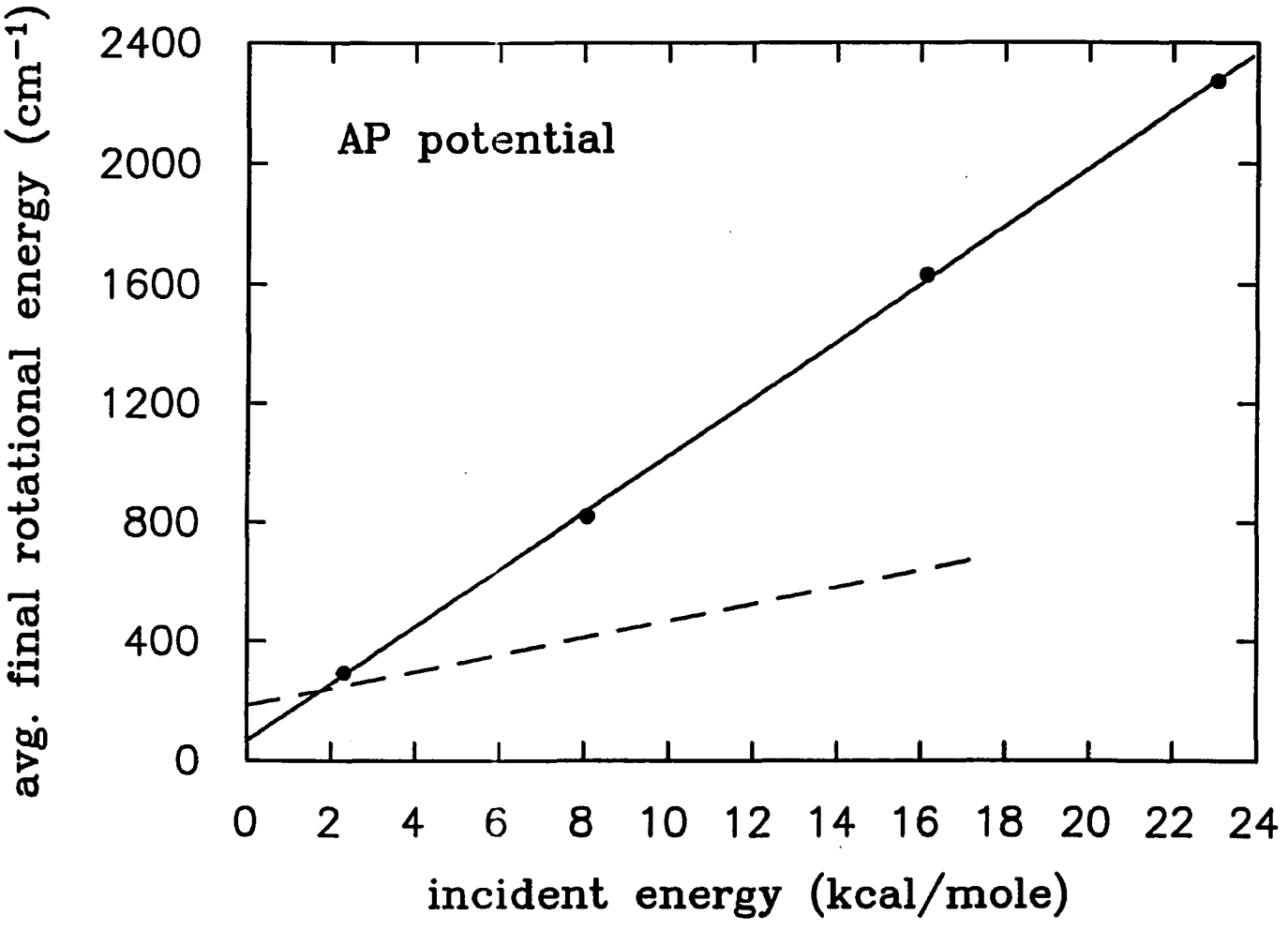

Figure 21. Dependence of the average final rotational energy on the incident translational energy for the AP potential. The solid line is a least-squares fit to the calculated results; the broken line is the least-squares fit to the experimental data from Figure 8.

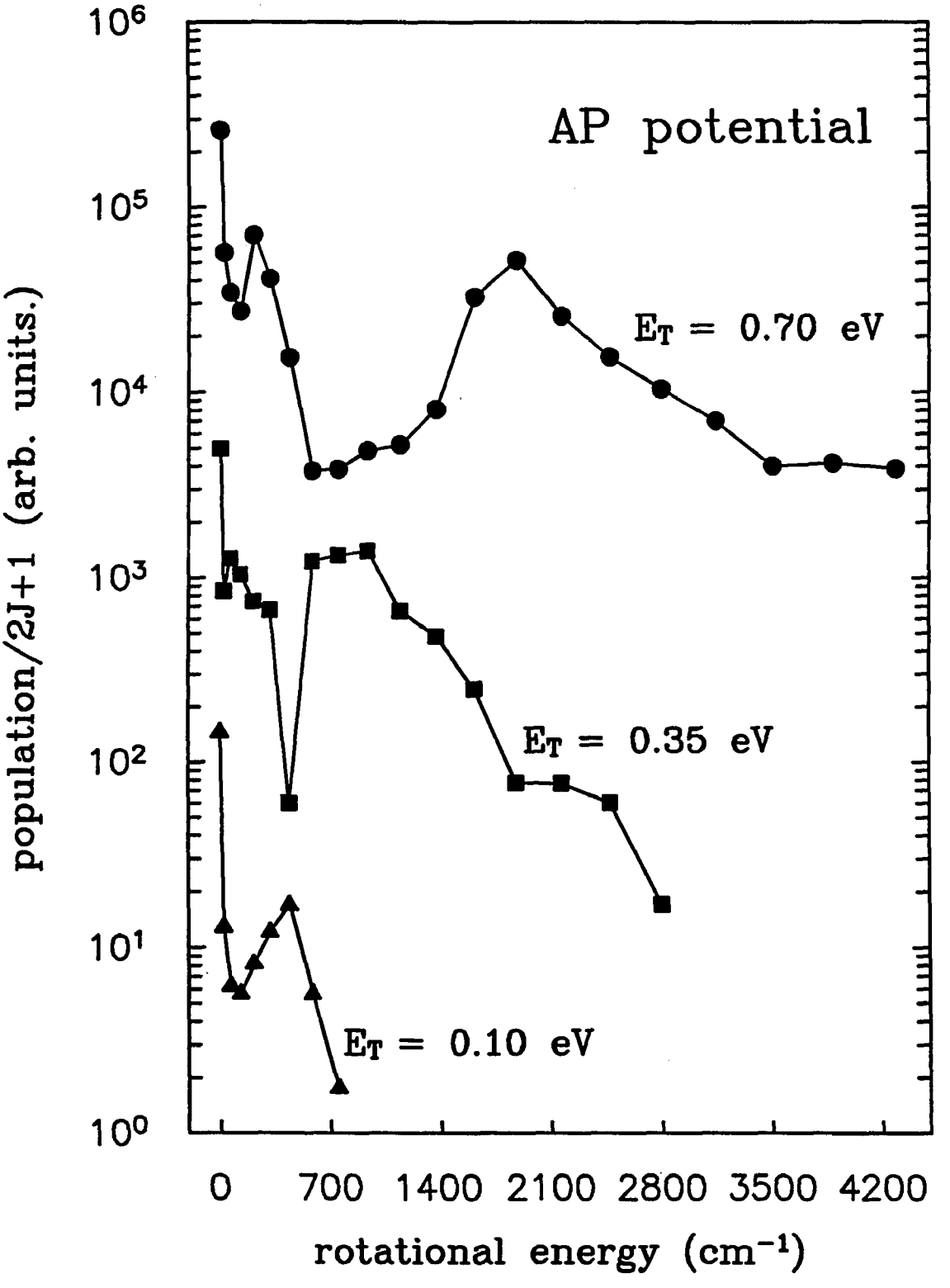

Figure 22. Rotational Boltzmann plots for the AP potential.

C. Discussion

Of the various potentials used in these calculations, the weakly perpendicular potential produced results that most closely resembled the experimental findings for HCl/gold scattering, particularly in the maximum value of J_f obtained and in the relative linearity of the Boltzmann plots at higher incident energy. If the WP interaction is at least qualitatively similar to the true HCl-gold interaction, then HCl binds to gold normal to the surface with the chlorine end down at equilibrium, and the anisotropy of the potential is fairly weak. This latter statement implies that the molecule appears to be relatively spherical. Such a conclusion is also suggested, for example, by the polarizabilty data for HCl. The ratio of its polarizability anisotropy to its orientationally-averaged (bulk) polarizability is only 12%, compared to 27% for CO, 39% for N_2, 48% for NO and 69% for O_2.[106] The picture of HCl that emerges is that of a roughly spherical chlorine atom having a small blister corresponding to the hydrogen atom. From this point of view, the shortcoming of the SP potential is that its anisotropy is much too large, due to the very strong repulsive interaction of the hydrogen atom with the surface (the pre-exponential constant A_H for the H-atom repulsion in the SP potential is 634 eV).

However, as the previous section pointed out, the WP potential predicts an increasingly large peak in the probability distributions at $J_f = 0$ as the incident energy decreases, which is the opposite of the experimental trend. In fact, all of the potentials used in this work, including the AP potential, give such a result. This occurs due to the

combined effect of forces that orient the molecule toward perpendicular, Cl-down collision geometries and kinematic constraints resulting from the large difference between the masses of H and Cl. The orienting forces, which exist at short and long range for the WP and SP potentials and at long range for the AP case, grow more influential as the collision energy decreases, so that increasing numbers of trajectories experience nearly end-on collisions. If the center of mass were at the geometric center of the molecule, these chlorine-end-down ($\theta = 0°$) collisions would produce large rotational excitation about the center of mass. However, due to the mass disparity, the center of mass lies essentially at the chlorine atom. In this case, the molecule appears almost spherical with respect to excitation of rotation about the center of mass for a relatively large θ interval near $\theta = 0°$. Thus, the increasing number of Cl-down collisions as E_T decreases create a larger $J_f = 0$ peak. If the WP potential is qualitatively correct, some explanation must be found for the decreasing magnitude of the zero-energy rainbow. A likely one is the effect that statistical averaging has on the final state distributions.

The results of a molecular beam-surface scattering experiment inherently reflect statistical averaging over the quantities which lie beyond the control of the experimenter. In the present case, such quantities include the initial orientation of the molecule, θ_i; the initial rotational quantum number J_i, for which some probability distribution in the incident beam exists; the impact site within the surface unit cell, since the actual surface is corrugated; and thermal motion of the atoms of the solid, which in the experiment is non-rigid and at non-zero

temperature. In the calculations reported in the preceding section, the first of these, θ_i, was averaged using the Monte Carlo procedure, while J_i was not averaged but simply set to zero, due to the preponderance of this state in the incident beam. In the rigid, flat surface approximation, neither corrugation nor surface motion were considered at all; as indicated in Section A, the experimental results suggest that this approximation is not a bad one for this system. To investigate the effect of averaging over the HCl rotational state distribution in the incident molecular beam, sets of trajectories were run at various incident energies using the WP potential, with Monte Carlo selection of J_i from the probability distribution given in Section A. The resulting final state distributions are compared in Figure 23 with those from Figure 15 for the WP potential with $J_i = 0$. Figure 23 shows that this averaging decreases the size of the zero-energy peak, while leaving the rest of the distribution relatively unchanged. The magnitude of the the peak decreases by slightly larger amounts (percentage-wise) as E_T decreases. This is the correct trend, but is far too small an effect to make up the discrepancy between the experimental and calculated results.

No calculations which include the effects of surface corrugation and thermal motion of the solid have been performed in this work on HCl/Au scattering. Based on the results of previous diatom-surface scattering calculations reported in the literature, one might conclude that the former of these would have the larger impact on the magnitude of the zero-energy rotational rainbow. Bowman and Park[64,68] have shown that trajectories producing low rotational excitation for a flat surface can produce high excitation in the presence of corrugation, due to trapping

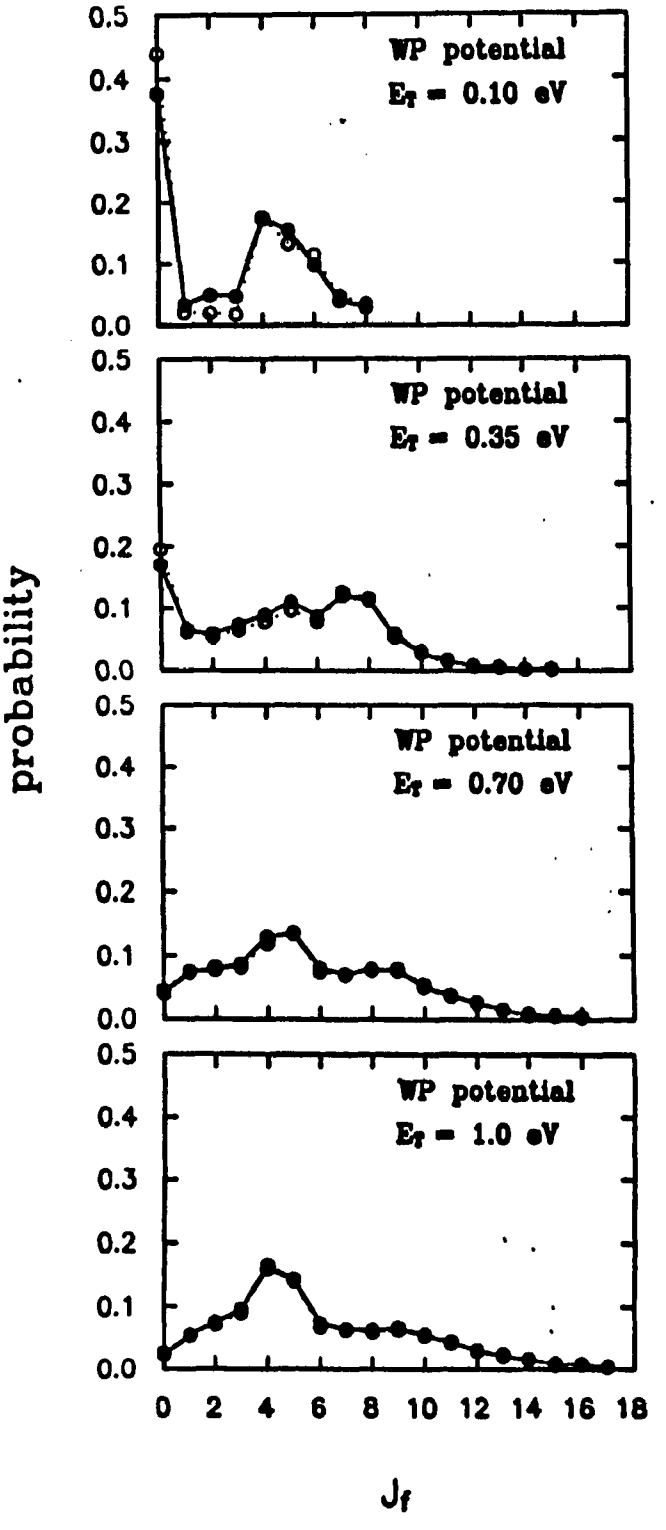

Figure 23. Effect on the WP final rotational state distributions due to statistical averaging over initial rotational state. The filled-circle results had J_i chosen from the experimental incident-beam distribution, while the open-circle results had $J_i = 0$ for all trajectories.

and multiple collision effects. Wolf *et al.*[65] demonstrated that sufficiently large corrugation can completely destroy the zero-energy rainbow. Brenig and coworkers[30,32,33] found that corrugation rather than surface vibration plays the major role in broadening rainbow features for NO collisions with the Ag(111) surface, whose corrugation is relatively small. Also, both Hurst *et al.*[61] and Muhlhausen and coworkers[86] have pointed out that the high-J_f rainbows produced by the repulsive part of the potential are more sensitive to thermal averaging than the zero-energy rainbow. It would be instructive to conduct further calculations which include corrugation and surface motion. A simple way to do the former would be to multiply the WP potential by a corrugation factor $[1 + \beta\ Q(X_{cm},Y_{cm})]$, as Wolken[11] and several others have done. The latter could be done, for example, using the one-dimensional simple harmonic oscillator (SHO) or generalized Langevin oscillator (GLO) prescriptions given by Polanyi and Wolf.[67]

CHAPTER V

THEORY AND IMPLEMENTATION OF NO/LiF CALCULATIONS

The third part of this dissertation, consisting of Chapters V and VI, describes the calculations done in this work on the scattering of NO from LiF(001). These calculations employ the reduced equations of motion (REOM) formalism developed by Diestler and Riley.[2] This theory, which includes the effects of the motion of a solid into a gas-surface scattering calculation which does not explicitly integrate equations of motion for the solid, is incorporated into the QCT procedure discussed in Chapter II via the velocity reset technique.[5] The object of this study is to test the performance of the REOM for the case of diatom-surface scattering. This assessment, which is the topic of Chapter VI, is made by comparing the REOM results with those of detailed stochastic trajectory calculations by Lucchese and Tully on the NO/LiF system.[3] The present chapter develops the theory required to do the calculations and explains how the theory was actually applied in the present case. Sections A and B discuss the theory of the REOM and of the velocity reset procedure, respectively. Section C describes the potential energy surface used to model the NO/LiF interaction. Finally, section D presents the details of the computational procedure.

A. Derivation of the Reduced Equations of Motion

In this section the formalism is derived for including energy transfer between a gas-phase molecule and a surface into a calculation in which equations of motion of the atoms of the solid are not considered. This is accomplished by replacing the full set of EOM, which involve coordinates of both the gas molecule and the solid, with a reduced set containing only the gas-molecule coordinates. The reduced equations contain a frictional damping term which accounts for the effects of the motion of the solid. The discussion in this section, which closely follows that given by Diestler and Riley in reference 2, is divided into two parts. The first part shows how the solid-atom EOM are replaced by the damping term in the gas-molecule EOM; the second part describes the approximations made to obtain the simplified damping matrix actually used in the calculations.

1. Derivation of the Damping Matrix

The starting point for the derivation is the set of Newton's equations of motion (NEOM) for the gas molecule and the solid, which is assumed to be harmonic. If the molecule has N_A atoms and the surface N_S atoms, then these EOM can be expressed in matrix form as

$$\underline{\underline{m}}\,\ddot{\underline{r}} = \underline{f}^{int}_{mol} + \underline{f}^{gs}_{mol}, \tag{5.1a}$$

$$\underline{\underline{M}}\,\ddot{\underline{u}} = \underline{f}^{harm}_{surf} + \underline{f}^{gs}_{surf}. \tag{5.1b}$$

In equation (5.1a), $\underline{r}$ is the column matrix containing the $3N_A$ Cartesian coordinates of the atoms in the gas molecule (the first element being the x coordinate of atom 1 and the last element the z coordinate of atom N_A); $\underline{\underline{m}}$ is the $3N_A \times 3N_A$ diagonal matrix of gas atom masses (the first three diagonal elements being the mass m_1 of atom 1, and so on); the column matrices $\underline{f}^{int}_{mol}$ and $\underline{f}^{gs}_{mol}$ contain the Cartesian components of the forces acting on the gas atoms due to the internal potential of the isolated molecule, V_{int}, and the gas-surface interaction potential, V_{gs}, respectively. In equation (5.1b), $\underline{u}$ is the column matrix of the $3N_S$ Cartesian displacements the atoms of the solid from their equilibrium lattice positions; $\underline{\underline{M}}$ is the diagonal matrix of surface atom masses; $\underline{f}^{harm}_{surf}$ and $\underline{f}^{gs}_{surf}$ contain the forces on the solid atoms due to the harmonic potential of the isolated solid and the gas-surface interaction potential, respectively. The force on the atoms of the solid due to the harmonic potential is given by

$$\underline{f}^{harm}_{surf} = -\underline{\underline{\Phi}}\,\underline{u}, \tag{5.2a}$$

in which $\underline{\underline{\Phi}}$ is the force-constant matrix ($3N_S \times 3N_S$) of the isolated solid. The other force matrices in equations (5.1) are found from the gradients of the appropriate potential functions:

$$f^{int}_{mol,i} = -\frac{\partial V_{int}}{\partial r_i}, \tag{5.2b}$$

$$f^{gs}_{mol,i} = -\frac{\partial V_{gs}}{\partial r_i}, \tag{5.2c}$$

$$f^{gs}_{surf,i} = -\frac{\partial V_{gs}}{\partial u_i}, \tag{5.2d}$$

where the i subscript denotes the ith element of the corresponding matrix.

Equation (5.1b) can be solved using Fourier transforms.[113] Of particular interest in this case is the transform between the time, t, and the frequency, ω. The Fourier transform $F[a(t)]$ of a function a(t) and its inverse, $F^{-1}[\hat{A}(\omega)]$, are for the purposes of this derivation defined by[113]

$$\hat{A}(\omega) = F[a(t)] = \int_{-\infty}^{+\infty} a(t) \exp(-i\omega t)\, dt, \tag{5.3a}$$

$$a(t) = F^{-1}[\hat{A}(\omega)] = (2\pi)^{-1} \int_{-\infty}^{+\infty} \hat{A}(\omega) \exp(i\omega t)\, dt. \tag{5.3b}$$

(Other definitions exist which differ from (5.3) in the constant multiplying the integral and in the sign of i in the exponential.[114a]) In what follows, an upper-case letter with a caret denotes the frequency representation of a function. The Fourier transform of equation (5.1b) is

$$\underline{\underline{M}}\, F[\, \ddot{\underline{u}}(t)\,] + \underline{\underline{\Phi}}\, F[\, \underline{u}(t)\,] = F[\, \underline{f}^{gs}_{surf}(t)\,]\,. \tag{5.4}$$

Using the differentiation property of the Fourier transform[114a], this becomes

$$\left[-\omega^2 \underline{\underline{M}} + \underline{\underline{\Phi}} \right] \hat{\underline{U}}(\omega) = \hat{\underline{F}}(\omega), \tag{5.5}$$

where the superscript and subscript on the force matrix have been dropped for convenience. To ensure that the time integrals for the Fourier transform converge and that the boundary terms involved in the differentiation property are zero at $t = \pm\infty$, two conditions are specified: that $\underline{u}(t)$ and its time derivative go to zero as t goes to $-\infty$, and that the frequency variable ω in equations (5.3) has a small *negative* imaginary part $-i\epsilon$. The former involves the limit at $t = -\infty$, and the latter that at $t = +\infty$. (The physical significance of these requirements will be discussed below.)

Solving equation (5.5) for $\hat{\underline{U}}(\omega)$ yields

$$\hat{\underline{U}}(\omega) = -\left[\omega^2 \underline{\underline{M}} - \underline{\underline{\Phi}} \right]^{-1} \hat{\underline{F}}(\omega) = -\hat{\underline{\underline{G}}}(\omega)\, \hat{\underline{F}}(\omega). \tag{5.6}$$

$\hat{\underline{\underline{G}}}(\omega)$ is the Fourier transform of the response function (Green's function) for the solid, $\underline{\underline{G}}(t-\tau)$, which appears in the formal solution[114b] of equation (5.1b),

$$\underline{u}(t) = -\int_{-\infty}^{t} \underline{\underline{G}}(t-\tau)\, \underline{f}(\tau)\, d\tau, \tag{5.7}$$

where $\underline{f}$ is the gas-surface force of equation (5.2d). Applying the convolution property of the Fourier transform[114a] to (5.6), one obtains (5.7), except that the upper limit on the integral is $+\infty$ rather than t. The upper limit in (5.7) is correct since the response function $\underline{\underline{G}}(t-\tau)$ is zero for $\tau > t$; otherwise the solid would be responding to forces

$f(\tau)$ which have not yet been applied. This is a manifestation of the principle of *causality*. To see this explicitly, one can invert equation (5.6) using (5.3b):

$$\underline{u}(t) = (2\pi)^{-1} \int_{-\infty}^{+\infty} \exp(i\omega t)\, \hat{\underline{\underline{G}}}(\omega - i\epsilon)\, \hat{\underline{F}}(\omega)\, d\omega. \qquad (5.8a)$$

In this expression, the negative imaginary part of the frequency is included explicitly in the argument of the response matrix, because $\hat{\underline{\underline{G}}}(\omega)$ is not well-defined along the real ω axis. As the definition of $\hat{\underline{\underline{G}}}(\omega)$ in equation (5.6) shows, it has poles at $\omega = \omega_{0i}$, where ω_{0i} is the frequency of the ith normal mode of the lattice.[113] The effect of including $-i\epsilon$ is to move these poles off the real axis into the *upper* half of the complex plane (to $\omega = \omega_{0i} + i\epsilon$), so that the integration along the real axis is well-defined. By virtue of equation (5.3a), equation (5.8a) becomes

$$\underline{u}(t) = (2\pi)^{-1} \int_{-\infty}^{+\infty} \exp(i\omega t)\, \hat{\underline{\underline{G}}}(\omega - i\epsilon) \int_{-\infty}^{+\infty} \exp(-i\omega\tau)\, \underline{f}(\tau)\, d\tau\, d\omega$$

$$= \int_{-\infty}^{+\infty} \left\{ (2\pi)^{-1} \int_{-\infty}^{+\infty} \exp[i\omega(t-\tau)]\, \hat{\underline{\underline{G}}}(\omega - i\epsilon)\, d\omega \right\} \underline{f}(\tau)\, d\tau. \qquad (5.8b)$$

The integral in braces in equation (5.8b) is $\underline{\underline{G}}(t-\tau)$. It may be evaluated using contour integration. When $t-\tau < 0$ (*i. e.* $\tau > t$), the contour can be closed in the lower half-plane [$\mathrm{Im}(\omega) < 0$]; since there are no poles in the lower half-plane, the integral yields zero. Thus the upper limit on the τ integration may be changed from $+\infty$ to t, as causality requires. When $t-\tau > 0$, the contour can be closed in the upper half-plane. Since

the poles of $\hat{\underline{\underline{G}}}(\omega - i\epsilon)$ lie in this region, the integral is nonzero, and (5.8b) thus reduces to (5.7). At this point the physical significance of the imaginary part $-i\epsilon$ is clear. Without its presence in the argument of $\hat{\underline{\underline{G}}}(\omega)$, the response function is not well-defined. Furthermore, the sign of the imaginary part is determined by causality. If the imaginary part were $+i\epsilon$ rather than $-i\epsilon$, the poles of $\hat{\underline{\underline{G}}}$ would lie in the lower half-plane, and the solutions $\underline{u}(t)$ would be anti-causal (that is, the solid would respond before the force is applied).

Before continuing with the derivation, one other point should be discussed. In equation (5.6) the only contributions to the displacements of the atoms of the solid come from the harmonic lattice interactions and the gas-surface interaction forces. However, if the lattice is not initially at zero temperature, then thermal motion of the free lattice also contributes to $\underline{u}(t)$, in the form of a "random force" originating from the initial conditions for the thermal motion.[2,4,79] In a Laplace transform approach[4,79] to solving equation (5.1b), this random force arises naturally from the boundary terms (involving $\underline{u}(t=0)$ and $\dot{\underline{u}}(t=0)$) which are generated when the differentiation property of the Laplace transform[114c] is applied. In the Fourier transform approach, the analogous boundary terms (involving $\underline{u}(t=-\infty)$ and $\dot{\underline{u}}(t=-\infty)$) are infinite, unless forced to be zero by imposing the aforementioned condition that $\underline{u}(t=-\infty) = \dot{\underline{u}}(t=-\infty) = 0$. Physically, these conditions on $\underline{u}$ and $\dot{\underline{u}}$ mean that the solid is initially at zero surface temperature. This means that an additional term must be added on the right-hand side of equation (5.6) to account for the effects of thermal motion.[2,113] The derivation which follows assumes that no such extra term is present, which imposes the

condition that the lattice is initially at T = 0. Effects due to the thermal motion of a lattice at nonzero temperature will be incorporated using the velocity-reset technique to be discussed in section B below.

To proceed, then, one makes a crucial assumption:[2] that the surface adjusts *adiabatically* to the motion of the gas molecule. That is, one assumes that the forces on the solid atoms due to the presence of the gas molecule vary slowly on the time scale of the vibrational motion of the solid; the solid thus is assumed to respond instantaneously to the collisional force. In general, one would expect this to be the case when the gas atoms are large and massive, the solid atoms small and light and the collision energies not too great. If the adiabatic approximation holds, then the high frequency motion of the solid will not respond to the presence of the gas molecule; only frequencies near $\omega = 0$ will contribute to the response. Thus the response function $\hat{\underline{\underline{G}}}(\omega)$ is approximated by a Taylor expansion truncated after the linear term. In particular, one expands $\hat{\underline{\underline{G}}}$ around $\omega = -i\epsilon$ (at which point ω_r, the real part of the frequency, equals zero) to find

$$\hat{\underline{\underline{G}}}(\omega) = \hat{\underline{\underline{G}}}(-i\epsilon) + \lambda\, \hat{\underline{\underline{G}}}'(-i\epsilon)\, (\omega + i\epsilon) + O(\omega^2), \qquad (5.9)$$

where the prime denotes the derivative with respect to ω. Looking ahead to the perturbative treatment which follows, an ordering parameter λ also has been inserted into equation (5.9). Dropping the quadratic and higher terms from (5.9) and substituting into equation (5.6) yields

$$\hat{\underline{U}}(\omega) = -\left[\hat{\underline{\underline{G}}}(-i\epsilon) + \lambda\, \omega\, \hat{\underline{\underline{G}}}'(-i\epsilon) + i\epsilon\, \lambda\, \hat{\underline{\underline{G}}}'(-i\epsilon) \right] \hat{\underline{F}}(\omega). \qquad (5.10)$$

To find the displacement matrix $\underline{u}(t)$, one applies the inverse Fourier transform to equation (5.10), and then takes the $\epsilon \to 0$ limit. Noting that $\hat{\underline{\underline{G}}}(-i\epsilon)$ and $\hat{\underline{\underline{G}}}'(-i\epsilon)$ are constants, the inversion gives

$$\underline{u}(t) = -\left[\hat{\underline{\underline{G}}}(-i\epsilon) + i\epsilon\,\lambda\,\hat{\underline{\underline{G}}}'(-i\epsilon)\right]\underline{f}(t) - \lambda\,\hat{\underline{\underline{G}}}'(-i\epsilon)\,F^{-1}\left[\omega\,\hat{\underline{F}}(\omega)\right]. \quad (5.11)$$

Applying the differentiation property of the Fourier transform to the second term on the right hand side of equation (5.11), and taking the limit $\epsilon \to 0$, one finds

$$\underline{u}(t) = -\hat{\underline{\underline{G}}}(0)\,\underline{f}(t) + i\,\lambda\,\hat{\underline{\underline{G}}}'(0)\,\dot{\underline{f}}(t). \quad (5.12)$$

Since the surface is initially at $T = 0$, the elements of the force matrix $\underline{f}(t)$ are given by equation (5.2d); the chain rule thus shows the total time derivative of the kth element to be

$$\dot{f}_k(t) = -\sum_{i=1}^{N_S} \frac{\partial V_{gs}}{\partial u_k \partial u_i}\,\dot{u}_i(t) - \sum_{j=1}^{N_A} \frac{\partial V_{gs}}{\partial u_k \partial r_j}\,\dot{r}_j(t). \quad (5.13)$$

This can be expressed in matrix notation as

$$\dot{\underline{f}}(t) = -\underline{\underline{K}}^{SS}\,\dot{\underline{u}}(t) - \underline{\underline{K}}^{SA}\,\dot{\underline{r}}(t), \quad (5.14a)$$

in which the elements of the coupling matrices $\underline{\underline{K}}^{SS}$ and $\underline{\underline{K}}^{SA}$ are specified by

$$K^{SS}_{mn} = \frac{\partial V_{gs}}{\partial u_m \partial u_n}, \qquad K^{SA}_{mn} = \frac{\partial V_{gs}}{\partial u_m \partial r_n}. \tag{5.14b}$$

The S and A superscripts denote partial differentiation with respect to solid and gas atom coordinates, respectively, and therefore specify the dimensionality of the matrix. Thus $\underline{\underline{K}}^{SS}$ is a $3N_S \times 3N_S$ matrix and $\underline{\underline{K}}^{SA}$ is a $3N_S \times 3N_A$ matrix. Both these matrices are time-dependent, since the coordinates u_i and r_i depend on time.

To proceed with the derivation using equation (5.12), expansions of $\underline{u}(t)$ and $\underline{f}(t)$ in terms of λ are required. Formally one can write

$$\underline{u}(t) = \underline{u}^{(0)}(t) + \lambda\, \underline{u}^{(1)}(t) + \lambda^2\, \underline{u}^{(2)}(t) + \cdots, \tag{5.15}$$

where $\underline{u}^{(k)}$ is the correction of order k. The zeroth-order term $\underline{u}^{(0)}(t)$ gives the zero-frequency displacements of the lattice atoms due to the presence of the gas molecule (see equation (5.17a) below). The other terms reflect the frequency-dependent response of the solid; of particular interest in what follows will be the first-order correction $\underline{u}^{(1)}(t)$. Considering $\underline{f}(t)$ as a function of $\underline{u}(t)$ and expanding it around $\underline{u} = \underline{u}^{(0)}$ yields

$$\begin{aligned} \underline{f}(t) &= \underline{f}^{(0)}(t) - \underline{\underline{K}}^{SS(0)}[\underline{u}(t) - \underline{u}^{(0)}(t)] + \cdots \\ &= \underline{f}^{(0)}(t) - \lambda\, \underline{\underline{K}}^{SS(0)}\, \underline{u}^{(1)}(t) + O(\lambda^2), \end{aligned} \tag{5.16}$$

where equation (5.15) was used. The (0) superscript on $\underline{f}$ and $\underline{\underline{K}}^{SS}$ means that they are evaluated using $\underline{u}^{(0)}$. Substituting equations (5.14a), (5.15) and (5.16) into equation (5.12) and equating coefficients of

powers of λ results in the following expressions for $\underline{u}^{(0)}$ and $\underline{u}^{(1)}$:

$$\underline{u}^{(0)}(t) = -\hat{\underline{\underline{G}}}(0)\,\underline{f}^{(0)}(t), \tag{5.17a}$$

$$\underline{u}^{(1)}(t) = \hat{\underline{\underline{G}}}(0)\,\underline{\underline{K}}^{SS(0)}\,\underline{u}^{(1)}(t) - i\,\hat{\underline{\underline{G}}}'(0)\,\underline{\underline{K}}^{SS(0)}\,\dot{\underline{u}}^{(0)}(t) - i\,\hat{\underline{\underline{G}}}'(0)\,\underline{\underline{K}}^{SA(0)}\,\dot{\underline{r}}(t). \tag{5.17b}$$

As mentioned above, $\underline{u}^{(0)}$ gives the zero-order displacement of the solid atoms due to the presence of the diatom. In particular, since in the adiabatic approximation the solid adjusts instantaneously to the presence of the gas molecule, the zero-order response $\underline{u}^{(0)}$ describes the distortion of the lattice to its new equilibrium geometry in the presence of the force field of the *fixed* diatom. To see this, one can consider a one-dimensional harmonic oscillator (with force constant k) under the influence of a fixed force of magnitude f. The potential energy of this oscillator is $V(x) = \frac{1}{2}kx^2 + ax$, and the value of x which minimizes V(x) is easily shown to be $x_{min} = -a/k$. Equation (5.17a) is a many-dimensional generalization of this expression for x_{min}, since $\hat{\underline{\underline{G}}}(0) = \underline{\underline{\Phi}}^{-1}$ is the just the inverse of the force-constant matrix of the solid. As will be shown next, the first-order term $\underline{u}^{(1)}$ gives a correction to the zero-order result due to the motion of the diatom (note the presence of $\dot{\underline{r}}$ in equation (5.22) below).

To obtain a simplified expression for $\underline{u}^{(1)}$, one begins by finding $\dot{\underline{u}}^{(0)}(t)$ from the time derivative of equation (5.17a), using equation (5.14a):

$$\begin{aligned}
\dot{\underline{u}}^{(0)}(t) &= -\hat{\underline{\underline{G}}}(0)\,\dot{\underline{f}}^{(0)}(t) \\
&= -\hat{\underline{\underline{G}}}(0)\left[-\underline{\underline{K}}^{SS(0)}\,\dot{\underline{u}}^{(0)}(t) - \underline{\underline{K}}^{SA(0)}\,\dot{\underline{r}}(t)\right] \\
&= \left[\underline{\underline{1}} - \hat{\underline{\underline{G}}}(0)\,\underline{\underline{K}}^{SS(0)}\right]^{-1}\hat{\underline{\underline{G}}}(0)\,\underline{\underline{K}}^{SA(0)}\,\dot{\underline{r}}(t). \qquad (5.18)
\end{aligned}$$

The third line in (5.18) follows from the second after collecting terms in $\dot{\underline{u}}^{(0)}$. If the $3N_S \times 3N_S$ matrix $\underline{\underline{D}}$ is defined as

$$\underline{\underline{D}} = \left[\underline{\underline{1}} - \hat{\underline{\underline{G}}}(0)\,\underline{\underline{K}}^{SS(0)}\right]^{-1}, \qquad (5.19)$$

then substituting equation (5.18) into equation (5.17b) and rearranging terms yields

$$\underline{u}^{(1)}(t) = -i\,\underline{\underline{D}}\,\hat{\underline{\underline{G}}}'(0)\left[\underline{\underline{1}} + \underline{\underline{K}}^{SS(0)}\,\underline{\underline{D}}\,\hat{\underline{\underline{G}}}(0)\right]\underline{\underline{K}}^{SA(0)}\,\dot{\underline{r}}(t). \qquad (5.20)$$

The factor in parentheses on the right hand side of equation (5.20) can be simplified as follows:

$$\begin{aligned}
\left[\underline{\underline{1}} + \underline{\underline{K}}^{SS(0)}\,\underline{\underline{D}}\,\hat{\underline{\underline{G}}}(0)\right] &= \underline{\underline{K}}^{SS(0)}\,\underline{\underline{D}}\left\{\underline{\underline{D}}^{-1}\,(\underline{\underline{K}}^{SS(0)})^{-1} + \hat{\underline{\underline{G}}}(0)\right\} \\
&= \underline{\underline{K}}^{SS(0)}\,\underline{\underline{D}}\left\{\left[\underline{\underline{1}} - \hat{\underline{\underline{G}}}(0)\,\underline{\underline{K}}^{SS(0)}\right](\underline{\underline{K}}^{SS(0)})^{-1} + \hat{\underline{\underline{G}}}(0)\right\} \\
&= \underline{\underline{K}}^{SS(0)}\,\underline{\underline{D}}\,(\underline{\underline{K}}^{SS(0)})^{-1} \\
&= \left[\underline{\underline{K}}^{SS(0)}\left[\underline{\underline{1}} - \hat{\underline{\underline{G}}}(0)\,\underline{\underline{K}}^{SS(0)}\right](\underline{\underline{K}}^{SS(0)})^{-1}\right]^{-1} \\
&= \left[\underline{\underline{1}} - \underline{\underline{K}}^{SS(0)}\,\hat{\underline{\underline{G}}}(0)\right]^{-1} \\
&= \underline{\underline{D}}^{T}, \qquad (5.21)
\end{aligned}$$

where the T superscript denotes the transpose of the matrix. The last equality in (5.21) follows from (5.19), since $\underline{\underline{K}}^{SS(0)}$ and $\hat{\underline{\underline{G}}}(0)$ are symmetric matrices. Thus equation (5.20) may be written

$$\underline{u}^{(1)}(t) = -i \, \underline{\underline{D}} \, \hat{\underline{\underline{G}}}'(0) \, \underline{\underline{D}}^T \, \underline{\underline{K}}^{SA(0)} \, \dot{\underline{r}}(t). \tag{5.22}$$

To complete the derivation of the reduced EOM, one must consider the EOM for the gas molecule, which are given in equation (5.1a). It is apparent that the only term in (5.1a) containing any dependence on the surface atom displacements $\underline{u}(t)$ is the gas-surface force, $\underline{f}_{mol}^{gs}$. This can be expanded around $\underline{u} = \underline{u}^{(0)}$ to obtain, by analogy with equation (5.16),

$$\underline{f}_{mol}^{gs} = \underline{f}_{mol}^{(0)} - \lambda \, \underline{\underline{K}}^{AS(0)} \, \underline{u}^{(1)}(t) + O(\lambda^2), \tag{5.23}$$

where $\underline{\underline{K}}^{AS}$ is the transpose of $\underline{\underline{K}}^{SA}$. Setting $\lambda = 1$ and substituting equations (5.22) and (5.23) into equation (5.1a) gives

$$\underline{\underline{m}} \, \ddot{\underline{r}} = \underline{f}_{mol}^{int} + \underline{f}_{mol}^{(0)} - \underline{\underline{m}} \, \underline{\underline{\beta}} \, \dot{\underline{r}}, \tag{5.24}$$

with the damping matrix $\underline{\underline{\beta}}$ identified as

$$\underline{\underline{\beta}} = -i \, \underline{\underline{m}}^{-1} \, \underline{\underline{K}}^{AS(0)} \, \underline{\underline{D}} \, \hat{\underline{\underline{G}}}'(0) \, \underline{\underline{D}}^T \, \underline{\underline{K}}^{SA(0)}. \tag{5.25}$$

Given the dimensions of the various matrices on the right hand side of equation (5.25), $\underline{\underline{\beta}}$ is evidently a $3N_A \times 3N_A$ matrix. Thus, the result of the above derivation has been to replace the original set of $3N_A + 3N_S$

NEOM, equations (5.1), with the set of $3N_A$ NEOM, equations (5.24), which differ in form from (5.1a) due to the inclusion of the damping term $-\underline{\underline{m}}\,\underline{\underline{\beta}}\,\dot{\underline{r}}$. This term includes, in an approximate manner, the effects of the omitted NEOM (5.1b).

As it stands, equation (5.24) is not independent of the surface coordinates, since both $\underline{f}_{mol}^{(0)}$ and $\underline{\underline{\beta}}$ depend on the zeroth-order displacements $\underline{u}^{(0)}(t)$ of equation (5.17a). Diestler and Riley[2] have named the set of coupled equations (5.17a) and (5.24) the "full adiabatic" or "FA" approximation. To completely eliminate the surface-motion dependence and so obtain a set of reduced EOM for the gas molecule, the further assumption is made that the effects of the zeroth-order displacement on the gas molecule are are minimal. This allows $\underline{u}^{(0)}(t)$ to be set to zero for all t, that is, for the atoms of the solid to be "frozen" at their equilibrium positions. In this "zero-displacement adiabatic" or "ZDA" approximation,[2] $\underline{f}_{mol}^{(0)}$ and $\underline{\underline{\beta}}$ now depend only on the degrees of freedom $\underline{r}(t)$ of the gas atoms and the positions of the atoms of the frozen solid. All of the effects of the surface dynamics on the motion of the gas molecule in equation (5.24) are included in the damping matrix, $\underline{\underline{\beta}}$. Diestler and Riley[2] have used both the FA and ZDA approximations to simulate the dynamics of atom-surface collisions. The present work contains the first application of the ZDA to study energy transfer between a surface and a diatomic molecule, for which internal degrees of freedom exist.

2. Simplified Expression for the Damping Matrix

In order to use equation (5.25), one must evaluate the various matrices it contains. The coupling matrices $\underline{\underline{K}}^{SA}$ and $\underline{\underline{K}}^{SS}$ involve partial derivatives of the gas-surface interaction potential, which are not difficult to compute. However, evaluating the elements of the response matrix $\hat{\underline{\underline{G}}}$ and its derivative $\hat{\underline{\underline{G}}}'$ is, in general, very involved, and not practical except for certain idealized cases,[2] such as the one-dimensional harmonic chain[115] and the three-dimensional Rosenstock-Newell lattice[116]. Thus it remains to approximate these matrices in order to obtain a workable expression for the damping matrix.

One approximation that results in considerable computational simplification is to assume that the atoms of the solid respond independently of each other. In this case, the response matrix and its derivative become block-diagonal, each block being 3 × 3 and involving a particular atom s of the solid. If the further approximation is made that the response is isotropic (in the same direction as the applied force), then each of these 3 × 3 blocks is also diagonal, with each of the diagonal elements of a given block having the same value. This is essentially the "weak-coupling approximation" previously used by Diestler and Riley[87] in gas-surface scattering calculations. The following expression for the diagonal matrix elements of the sth block of $\hat{\underline{\underline{G}}}(\omega)$, denoted $\hat{g}_s(\omega)$, can be found from the Debye approximation:[87]

$$\hat{g}_s(\omega) = -\frac{3}{M_s \omega_D^2}\left[1 + \frac{x}{2}\ln\frac{(1-x)}{(1+x)} - \frac{i\pi x}{2}\right], \qquad (5.26)$$

where M_s is the mass of atom s, ω_D is the Debye frequency of the solid, and $x = \omega / \omega_D$. For LiF, $\omega_D = 502\ cm^{-1} = 94.65$ radians/psec.[3] In the low-frequency regime where the adiabatic approximation holds, x approaches zero and equation (5.26) becomes

$$\hat{g}_s(0) = -\frac{3}{M_s \omega_D^2} . \tag{5.27}$$

Taking the low-frequency limit of the derivative with respect to frequency of equation (5.26) yields

$$\hat{g}_s'(0) = \frac{3\pi i}{2M_s \omega_D^3} . \tag{5.28}$$

With this approximation for the response matrix, one can proceed to find the matrix $\underline{\underline{D}}$. If the gas-surface interaction is dominated by pairwise interactions between the gas molecule and the surface, then the coupling matrix $\underline{\underline{K}}^{SS}$, whose elements are second partial derivatives of V_{gs} with respect to surface coordinates, must be block-diagonal with each block being 3 × 3 (this is not true for $\underline{\underline{K}}^{SA}$, however). Since $\underline{\underline{1}}$ is diagonal and $\hat{\underline{\underline{G}}}(0)$ is approximated as diagonal, $\underline{\underline{D}}$ must also be block-diagonal. Replacing each of these 3 × 3 blocks in $\underline{\underline{D}}$ with a scalar multiple of $\underline{\underline{1}}$ would simplify the computation of the damping matrix $\underline{\underline{\beta}}$; calculations on an idealized atom-surface scattering system[2] have shown that doing so is not a bad approximation. The definition of $\underline{\underline{K}}^{SS}$ suggests[117] approximating $\underline{\underline{D}}_s$ (the block corresponding to atom s of the solid) by

$$\underline{\underline{D}}_s = (1 - \hat{g}_s(0)\, \nabla_s^2\, V_{gs})^{-1}\, \underline{\underline{1}}. \tag{5.29}$$

Thus the matrix product $\underline{\underline{D}}\, \hat{\underline{\underline{G}}}'(0)\, \underline{\underline{D}}^T$ is, in this approximation, a diagonal matrix; the sth 3×3 block along its diagonal is given by

$$\left[\underline{\underline{D}}\, \hat{\underline{\underline{G}}}'(0)\, \underline{\underline{D}}^T \right]_s = \frac{\hat{g}_s'(0)}{(1 - \hat{g}_s(0)\, \nabla_s^2\, V_{gs})^2}\, \underline{\underline{1}} = W_s\, \underline{\underline{1}} \tag{5.30}$$

Finally, using equation (5.30), one can write down the expression used for the damping matrix $\underline{\underline{\beta}}$ in these calculations. If the rows and columns of $\underline{\underline{\beta}}$ and $\underline{\underline{K}}^{SA}$ are labeled by the atom (lower case Roman) and Cartesian component (lower case Greek) to which each corresponds, then use of equation (5.30) in equation (5.25) yields for the elements of the damping matrix

$$\beta_{a\alpha,a'\alpha'} = m_a^{-1} \sum_s -iW_s \sum_\gamma K^{AS}_{a\alpha,s\gamma}\, K^{SA}_{s\gamma,a'\alpha'} \tag{5.31}$$

with W_s defined in (5.30). The matrix elements of $\underline{\underline{\beta}}$ are real numbers, since, from (5.30) and (5.28), the product $(-iW_s)$ is real. The sum over s in equation (5.31) includes those atoms of the solid with which the gas molecule has a significant interaction. One should note that because the elements of the coupling matrix $\underline{\underline{K}}^{SA}$ are, according to (5.14b), just mixed second partial derivatives of the gas-surface interaction potential with respect to the gas and surface atom Cartesian coordinates, the matrix $\underline{\underline{\beta}}$ whose elements are given by equation (5.31) can be expressed in

the form $\underline{\beta} = \underline{\underline{m}}^{-1} \underline{\beta}^{sym}$, where $\underline{\beta}^{sym}$ is a *symmetric* matrix whose elements are given by (5.31) without the factor m_a^{-1}. This fact is important in developing a partial velocity reset scheme which can employ the damping given by equation (5.31).

To conclude this section, it should be pointed out that vibrational energy transfer directly to the lattice is not very efficient when the frequency of the vibrational mode in question is much greater than the Debye frequency for the lattice. Thus one expects that in such cases the damping of the vibrational motion derived from the adiabatic approximation used in these calculations will be too great. As Chapter VI will show, the calculations on the NO/LiF system, for which the diatom vibrational frequency is about four times the lattice Debye frequency, bear out this statement. This situation can be remedied by applying the damping in such a way that the vibrational mode in question is not affected, so that any vibrational energy transfer happens via coupling to translational and rotational motion.[2] The procedure used here to accomplish this modified damping, which is easily implemented with the velocity reset technique, is explained in section D of this chapter.

B. Partial Velocity Reset Procedure

As discussed in the previous section, the derivation of the reduced equations of motion is valid if the lattice is initially at temperature $T = 0$. Clearly, it would be desirable to somehow account for the effects of the thermal motion of a lattice having a nonzero temperature T. This has been done in these calculations using the partial velocity reset

technique developed by Riley, Coltrin and Diestler (RCD),[5] who modified Andersen's method for performing molecular dynamics simulations at constant temperature.[89] RCD implemented the procedure to simulate energy transfer (damping and thermal agitation) between a dynamical subset of lattice atoms ("P zone") and a surrounding reservoir ("Q zone") in molecular dynamics calculations by applying the reset to the P zone atoms along the P-Q interface.[5] The discussion in this section is divided into three parts. The first part offers a general overview of the velocity reset procedure and how it is used in the present work. The second part discusses the behavior of the procedure in the limit that the resets are frequent and weak. The final part presents a derivation of the form of the reset procedure actually employed in the NO/LiF scattering calculations described in the next chapter.

1. General Considerations

The velocity reset method in general involves replacing the velocities of some or all of the atoms whose equations of motion are being integrated with new velocities, chosen by some algorithm, at various intervals during the integration. Andersen's procedure[89] sequentially reset the velocity of each atom at random intervals to a value selected from a Maxwellian distribution at temperature T; this, in effect, served as a "thermostat" to keep the system at a constant temperature. RCD's method[5] involves simultaneously replacing the velocities of some or all the atoms, at regular intervals, with new velocities given by the following expression:

$$v_i^{new}(t_n) = (1 - \theta_{i,n})^{1/2} v_i^{old}(t_n) + \theta_{i,n}^{1/2} v_i^T(\xi), \qquad (5.32)$$

in which the reset parameter $\theta_{i,n}$ ($0 \le \theta_{i,n} \le 1$) governs the strength of the reset for the velocity of atom i at the time t_n of the nth reset. $v_i^T(\xi) = (kT/m_i)^{1/2} \xi$, where k is Boltzmann's constant, is a velocity chosen randomly from a one-dimensional Maxwellian velocity distribution at temperature T, according to a Gaussianly-distributed random number from the sequence ξ. The i subscript on $v^T(\xi)$ emphasizes that the randomly-selected Maxwellian velocity is uncorrelated for different components i. When $\theta_{i,n}$ is set equal to unity for all i and n, one obtains essentially the Andersen reset procedure (the only differences being the simultaneous reset and the regular reset interval); any other value of $\theta_{i,n}$ yields what RCD have labeled the *partial* velocity reset, in which the atoms retain some "memory" of their old velocities.[5]

As discussed in reference 5, the full ($\theta = 1$) and partial velocity reset procedures described in the preceding paragraph may be employed to facilitate a molecular dynamics simulation of a solid at temperature T. The full reset is useful before the start of a trajectory as a thermostat to select initial conditions for the motion of the P zone. The thermostating procedure consists of integrating the EOM for one reset interval, resetting the velocities of all the atoms, and then repeating this cycle many times. During the course of the trajectory, the partial reset may be used to account for energy transfer between the P and Q zones by applying it to the atoms along the P-Q interface. This application is justified by the fact that the partial reset becomes

equivalent to explicit inclusion of damping and Gaussian random force terms in the EOM, in the limit that the reset is frequent and weak. This equivalence is demonstrated in subsection 2 below.

As mentioned earlier, RCD have incorporated the velocity reset method into molecular dynamics calculations.[5] In that work, both the full and partial resets were used, in the manner described in the previous paragraph. In the present work, however, only the partial reset is needed. The full reset is not employed because in the calculations performed here, which involve the ZDA approximation derived in section A, the atoms of the solid are fixed at their equilibrium positions; consequently, no thermostating procedure to determine their initial conditions is required. Conceptually speaking, in the ZDA approximation the gas molecule comprises the P zone and the entire solid constitutes the reservoir. Thus, in this work the partial velocity reset is applied to the atoms of the gas molecule, to account for energy transfer between the molecule and the solid. The reset is linked to the ZDA model through the relationship of the reset parameter $\theta_{i,n}$ to the damping matrix $\underline{\beta}$.

2. Limiting Behavior of the Reset

The form of the velocity reset algorithm in equation (5.32) ensures that the reset procedure has the following important property:[5] in the limit that the velocity resets are frequent and weak, the procedure reduces to inclusion of damping and random force terms in the EOM (equivalent to the GLE formalism of Lucchese and Tully[82]), provided that the reset parameter $\theta_{i,n}$ and the damping coefficient β are correctly

related. This may be shown as follows.[5] Newton's equation of motion for the ith atom is

$$m_i \dot{v}_i = F_i, \tag{5.33}$$

where m_i is the mass of and F_i the total force on atom i. After integrating from time t_n to time t_{n+1}, the velocity before resetting at t_{n+1} is given in terms of the velocity after resetting at t_n by equation (5.33) as

$$v_i^{old}(t_{n+1}) = v_i^{new}(t_n) + m_i^{-1} F_i \Delta t + O(\Delta t_r^2), \tag{5.34}$$

where the reset interval $\Delta t_r = t_{n+1} - t_n$ is small, since the reset is frequent. Subtracting $v_i^{old}(t_n)$ from both sides of equation (5.32) and combining with equation (5.34) gives

$$v_i^{old}(t_{n+1}) - v_i^{old}(t_n) - m_i^{-1} F_i \Delta t_r = \left[(1 - \theta_{i,n})^{1/2} - 1 \right] v_i^{old}(t_n) + \theta_{i,n}^{1/2} v_i^T(\xi) + O(\Delta t_r^2). \tag{5.35}$$

Since the reset is weak, $\theta_{i,n}$ is small and the binomial expansion can be used on the first term on the right hand side of equation (5.35). After doing so and then dividing through by Δt_r one obtains

$$\left[v_i^{old}(t_{n+1}) - v_i^{old}(t_n) \right] / \Delta t_r = m_i^{-1} F_i - (\theta_{i,n} / 2\Delta t_r) v_i^{old}(t_n) + (\theta_{i,n}^{1/2} / \Delta t_r) v_i^T(\xi) + O(\Delta t_r) + O(\theta_{i,n}^2 / \Delta t_r). \tag{5.36}$$

If β is defined by

$$\beta_{i,n} = \theta_{i,n} / 2\,\Delta t_r, \tag{5.37}$$

then in the limit that $\theta_{i,n}$ and Δt_r approach zero at fixed $\beta_{i,n}$, equation (5.36) becomes

$$\begin{aligned} \dot{v}_i &= m_i^{-1} F_i - \beta_i(t)\, v_i + (2\,\beta(t) / \Delta t_r)^{1/2}\, v_i^T(\xi) \\ &= m_i^{-1} F_i - \beta_i(t)\, v_i + m_i^{-1} F_i^R(t), \end{aligned} \tag{5.38a}$$

where

$$F_i^R(t) = \left[\frac{2\beta(t)}{\Delta t_r} \right]^{1/2} v_i^T(\xi) = \left[\frac{2\beta kT}{m_i \Delta t_r} \right]^{1/2} \xi \tag{5.38b}$$

is the random force. The n dependence of β becomes time dependence in the limit. The expression for the random force, equation (5.38b), is precisely the same[118] as that used in Tully's "ghost atom" GLE model;[4] the Lucchese-Tully model[82] eliminates the ghost atoms and attaches the damping and random force terms from the ghost atoms to the atoms along the P-Q interface. Thus, the limit of the velocity reset procedure, as specified by equation (5.38a), is indeed equivalent to the Lucchese-Tully approach, since the reset is applied only to the atoms along the P-Q interface.

Two items should be noted at this point. First, equation (5.37) is very important in the partial velocity reset scheme because it provides the connection between the reset parameter $\theta_{i,n}$ and the damping coefficient β, which allows the reset to be parametrized in terms of available

damping theories.[2,79,87] In particular, for these calculations the damping coefficient is given by equation (5.31) in the previous section. Second, it should be recognized that the partial velocity reset takes Brownian form as the reset interval goes to zero because the factor $A_{i,n} = (1 - \theta_{i,n})^{\frac{1}{2}}$, which multiplies $v_i^{old}(t_n)$ in equation (5.32), has the limiting value

$$\lim_{\Delta t_r \to 0} A_{i,n} = 1 - \Delta t_r \, \beta_{i,n}. \tag{5.39}$$

If this were not so, one could not go from equation (5.35) to equation (5.36). The limit (5.39) will be useful in the generalization of equation (5.32) which follows.

3. Generalization of the Velocity Reset Procedure

When RCD used the partial velocity reset in reference 5, they employed an approximation in which each component of the velocity of each atom is damped independently. If equation (5.32) is expressed in matrix form as

$$\underline{v}^{new} = (\underline{\underline{1}} - \underline{\underline{\theta}})^{\frac{1}{2}} \underline{v}^{old} + \underline{\underline{\theta}}^{\frac{1}{2}} \underline{v}^{T}(\xi), \tag{5.40}$$

in which the velocities are column vectors of length 3N, and the identity and $\underline{\underline{\theta}}$ matrices are of dimension 3N × 3N, where N is the number of atoms involved in the reset, then this independent damping implies that the matrices $\underline{\underline{\theta}}^{\frac{1}{2}}$ and $(\underline{\underline{1}} - \underline{\underline{\theta}})^{\frac{1}{2}}$ are diagonal. This must be true, since from

equation (5.37)

$$\underline{\underline{\theta}} = 2\,\Delta t_r\,\underline{\underline{\beta}}, \tag{5.41}$$

and the damping matrix $\underline{\underline{\beta}}$ is diagonal for the independent damping case. In general, however, $\underline{\underline{\beta}}$ is not diagonal; in particular, the damping matrix given by equation (5.31), which is used in these calculations, is not diagonal. Thus, a more general form for the velocity reset, which reduces to equation (5.40) when $\underline{\underline{\beta}}$ is diagonal, is required. This takes the form

$$\underline{v}^{new} = \underline{\underline{A}}\,\underline{v}^{old} + \underline{\underline{B}}\,\underline{v}^{T}(\xi). \tag{5.42}$$

Riley[119] has derived expressions for the matrices $\underline{\underline{A}}$ and $\underline{\underline{B}}$, using the conditions that the reset preserve a canonical velocity distribution and that the limit as $\Delta t_r \to 0$ of the matrix $\underline{\underline{A}}$, by analogy with equation (5.39), be given by

$$\lim_{\Delta t_r \to 0} \underline{\underline{A}} = \underline{\underline{1}} - \Delta t_r\,\underline{\underline{\beta}}, \tag{5.43}$$

The following discussion sets forth this derivation.

The condition that the velocity reset is to preserve a canonical distribution means that the ensemble-averaged probability distribution after the reset, $P_{new} \equiv P$, must be canonical if the probability distribution before the reset, $P_{old} \equiv P'$, was canonical.[119] Mathematically this can be expressed as:

$$P(\underline{p},\underline{q}) = \int d^{3N}p^{\xi} \int d^{3N}p' \int d^{3N}q' \; P'(\underline{p}',\underline{q}') \; \eta_p \exp[-(\underline{p}^{\xi})^T \underline{\underline{M}}^{-1} \underline{p}^{\xi} / 2kT) \times \delta^{3N}(\underline{q} - \underline{q}') \; \delta^{3N}(\underline{p} - \underline{\underline{A}}_p \underline{p}' - \underline{\underline{B}}_p \underline{p}^{\xi}). \quad (5.44)$$

In equation (5.44), the ξ superscript refers to a quantity randomly chosen from a Maxwellian at temperature T; the T superscript denotes the transpose of a vector or matrix. $\underline{\underline{M}}$ is the 3N × 3N diagonal matrix of masses m_i for the atoms whose velocities are being reset, k is Boltzmann's constant, and $\eta_p = \Pi (2\pi m_i kT)^{-\frac{1}{2}}$ is a normalization factor for the Maxwellian momentum distribution in the integrand. The matrix $\underline{\underline{A}}_p = \underline{\underline{M}} \, \underline{\underline{A}} \, \underline{\underline{M}}^{-1}$ is the matrix corresponding to $\underline{\underline{A}}$ when equation (5.42) is expressed in terms of momenta rather than velocities; $\underline{\underline{B}}_p$ is defined similarly. Equation (5.44) is expressed in terms of momenta $\underline{p}$ rather than velocities $\underline{v}$, as is customary when dealing with ensembles in classical mechanics. The exponential and the 3N-dimensional delta functions with matrix arguments are a shorthand notation for products of exponentials and delta functions.

The integrals over the coordinates $\underline{q}'$ can be done trivially using $\delta^{3N}(\underline{q} - \underline{q}')$. This reflects the fact that the reset only affects the velocities (momenta), while leaving the coordinates unchanged. Equation (5.44) then becomes (upon changing from momenta to velocities)

$$P(\underline{v},\underline{q}) = \int d^{3N}v^{\xi} \int d^{3N}v' \; P'(\underline{v}',\underline{q}) \; \eta_v \exp[-(\underline{v}^{\xi})^T \underline{\underline{M}} \, \underline{v}^{\xi} / 2kT) \times \delta^{3N}(\underline{v} - \underline{\underline{A}} \, \underline{v}' - \underline{\underline{B}} \, \underline{v}^{\xi}), \quad (5.45)$$

where $\eta_v = \Pi (m_i/2\pi kT)^{\frac{1}{2}}$. In changing dp^{ξ} and dp' to dv^{ξ} and dv', two factors $\mu = \Pi \, m_i$ are produced; one of these converts η_p to η_v, while the

other is canceled by a factor μ^{-1} generated by changing the argument of the delta function. For the sake of clarity, it should be pointed out that the shorthand notation $\underline{v}^{\xi}$ represents the same quantity as the symbol $\underline{v}^{T}(\xi)$ appearing in equation (5.42).

If now the pre-reset probability distribution P' is chosen to be of canonical form, that is,

$$P'(\underline{v}',\underline{q}) = \exp\{-(\underline{v}')^{T}\ \underline{\underline{M}}\ \underline{v}' / 2kT\} \times P_{Q}(\underline{q}), \tag{5.46}$$

then the desired form for the post-reset distribution P is

$$P(\underline{v},\underline{q}) = \exp\{-\underline{v}^{T}\ \underline{\underline{M}}\ \underline{v} / 2kT\} \times P_{Q}(\underline{q}), \tag{5.47}$$

which requires that $\underline{\underline{A}}$ and $\underline{\underline{B}}$ satisfy

$$\exp\{-\underline{v}^{T}\ \underline{\underline{M}}\ \underline{v} / 2kT\} = \int d^{3N}v^{\xi} \int d^{3N}v'\ \exp\{-(\underline{v}')^{T}\ \underline{\underline{M}}\ \underline{v}' / 2kT\}$$
$$\times\ \eta_{v} \exp\{-(\underline{v}^{\xi})^{T}\ \underline{\underline{M}}\ \underline{v}^{\xi} / 2kT\}\ \delta^{3N}(\underline{v} - \underline{\underline{A}}\ \underline{v}' - \underline{\underline{B}}\ \underline{v}^{\xi}). \tag{5.48}$$

Making the change of variable $\underline{s} = (2kT)^{-\frac{1}{2}}\ \underline{\underline{M}}^{\frac{1}{2}}\ \underline{v}$, with similar definitions for $\underline{s}'$ and $\underline{s}^{\xi}$, equation (5.48) can be written more compactly as

$$\exp\{-\underline{s}^{T}\ \underline{s}\} = \int d^{3N}s^{\xi} \int d^{3N}s'\ \exp\{-(\underline{s}')^{T}\ \underline{s}'\}\ \eta_{s} \exp\{-(\underline{s}^{\xi})^{T}\ \underline{s}^{\xi}\}$$
$$\times\ \delta^{3N}(\underline{s} - \underline{\underline{A}}_{s}\ \underline{s}' - \underline{\underline{B}}_{s}\ \underline{s}^{\xi}), \tag{5.49}$$

in which $\eta_{s} = \pi^{-3N/2}$, $\underline{\underline{A}}_{s} = \underline{\underline{M}}^{\frac{1}{2}}\ \underline{\underline{A}}\ \underline{\underline{M}}^{-\frac{1}{2}}$ and $\underline{\underline{B}}_{s} = \underline{\underline{M}}^{\frac{1}{2}}\ \underline{\underline{B}}\ \underline{\underline{M}}^{-\frac{1}{2}}$.

The solution of equation (5.49) for $\underline{\underline{A}}_s$ and $\underline{\underline{B}}_s$ is in general difficult, but fairly straightforward in the special case that $\underline{\underline{A}}_s$ and $\underline{\underline{B}}_s$ can be diagonalized by the *same orthogonal transformation* T,[119] that is,

$$\underline{\underline{A}}_s^d = \underline{\underline{T}}^T \underline{\underline{A}}_s \underline{\underline{T}}, \tag{5.50a}$$

$$\underline{\underline{B}}_s^d = \underline{\underline{T}}^T \underline{\underline{B}}_s \underline{\underline{T}}, \tag{5.50b}$$

$$\underline{\underline{T}}^T \underline{\underline{T}} = \underline{\underline{1}}. \tag{5.50c}$$

where the d superscript denotes that the matrix is diagonal. As will be shown below, this case applies for the damping matrix specified by equation (5.31). Given this extra condition on $\underline{\underline{A}}_s$ and $\underline{\underline{B}}_s$, making the change of variable $\underline{s} = \underline{\underline{T}}\,\underline{x}$ (and similarly for $\underline{s}'$ and $\underline{s}^\xi$) changes equation (5.49) to

$$\exp(-\underline{x}^T \underline{x}) = \int d^{3N}x^\xi \int d^{3N}x' \exp(-(\underline{x}')^T \underline{x}') \eta_s \exp(-(\underline{x}^\xi)^T \underline{x}^\xi) \times \delta^{3N}(\underline{x} - \underline{\underline{A}}_s^d \underline{x}' - \underline{\underline{B}}_s^d \underline{x}^\xi). \tag{5.51}$$

Because the matrices in the argument of the delta function are diagonal, equation (5.51) is the product of 3N equations of the form

$$\exp(-x_j^2) = \int dx_j^\xi \int dx_j' \exp(-x_j'^2) \pi^{-\frac{1}{2}} \exp(-x_j^{\xi 2}) \times \delta(x_j - a_j x_j' - b_j x_j^\xi), \tag{5.52}$$

where $a_j = (\underline{\underline{A}}_s^d)_{jj}$ and b_j is similarly defined. One of the two integrals in equation (5.52) can be performed immediately using the delta function; the remaining integral can be easily evaluated after

completing the square in the exponent of the integrand. The result is

$$\exp\{-x_j^2\} = (a_j^2 + b_j^2)^{-\frac{1}{2}} \exp\{-x_j^2 / (a_j^2 + b_j^2)\}, \qquad (5.53)$$

which demands that $a_j^2 + b_j^2 = 1$, or, in matrix form,

$$(\underline{\underline{A}}_s^d)^2 + (\underline{\underline{B}}_s^d)^2 = \underline{\underline{1}}. \qquad (5.54a)$$

This condition is equivalent to the following two expressions:

$$\underline{\underline{A}}_s^2 + \underline{\underline{B}}_s^2 = \underline{\underline{1}}, \qquad (5.54b)$$

$$\underline{\underline{A}}^2 + \underline{\underline{B}}^2 = \underline{\underline{1}}. \qquad (5.54c)$$

Equation (5.54b) follows from (5.54a) by doing the inverse of the transformation (5.50), since $\underline{\underline{A}}_s$ and $\underline{\underline{B}}_s$ are both diagonalized by $\underline{\underline{T}}$; equation (5.54c) follows from (5.54b) using the definitions of $\underline{\underline{A}}_s$ and $\underline{\underline{B}}_s$ in terms of $\underline{\underline{A}}$ and $\underline{\underline{B}}$, which were given after equation (5.49). Fulfilment of the condition (5.54) will ensure that the velocity reset of equation (5.42) preserves a canonical distribution, provided that (5.50) is valid. Thus, for example, a canonical distribution is maintained by the velocity reset used in reference 5, since $\underline{\underline{A}}$ and $\underline{\underline{B}}$ in equation (5.40) satisfy (5.54c) and (5.50) (with $\underline{\underline{T}} = \underline{\underline{1}}$).

It remains to choose a form for $\underline{\underline{A}}$ and $\underline{\underline{B}}$ which satisfies the conditions given by equations (5.43), (5.50) and (5.54). From equation (5.43) and the definition of $\underline{\underline{A}}_s$ in terms of $\underline{\underline{A}}$, one can see that in the $\Delta t_r \to 0$ limit,

$$\underline{\underline{A}}_s = \underline{\underline{1}} - \Delta t_r \, \underline{\underline{M}}^{\frac{1}{2}} \, \underline{\underline{\beta}} \, \underline{\underline{M}}^{-\frac{1}{2}}, \tag{5.55}$$

Since the damping matrix whose elements are given by equation (5.31) is of the form $\underline{\underline{\beta}} = \underline{\underline{M}}^{-1} \, \underline{\underline{\beta}}^{sym}$, where $\underline{\underline{\beta}}^{sym}$ is a symmetric matrix, for this case one can express (5.55) as

$$\underline{\underline{A}}_s = \underline{\underline{1}} - \Delta t_r \, \underline{\underline{M}}^{-\frac{1}{2}} \, \underline{\underline{\beta}}^{sym} \, \underline{\underline{M}}^{-\frac{1}{2}}, \tag{5.56}$$

Thus, as Δt_r approaches zero, $\underline{\underline{A}}_s$ is a symmetric matrix and can be diagonalized by an orthogonal transformation. In light of this, $\underline{\underline{T}}$ of equation (5.50) is chosen[119] as the orthogonal matrix which diagonalizes $\underline{\underline{A}}_s$ of equation (5.56):

$$\underline{\underline{T}}^T \left[\underline{\underline{M}}^{-\frac{1}{2}} \, \underline{\underline{\beta}}^{sym} \, \underline{\underline{M}}^{-\frac{1}{2}} \right] \underline{\underline{T}} = \underline{\underline{\beta}}^d, \tag{5.57}$$

whence

$$\lim_{\Delta t_r \to 0} \underline{\underline{A}}_s^d = \underline{\underline{1}} - \Delta t_r \, \underline{\underline{\beta}}^d. \tag{5.58}$$

If now, by analogy to equation (5.41), one defines the diagonal matrix $\underline{\underline{\theta}}^d$ by

$$\underline{\underline{\theta}}^d = 2 \, \Delta t_r \, \underline{\underline{\beta}}^d, \tag{5.59}$$

then choosing $\underline{\underline{A}}_s^d$ and $\underline{\underline{B}}_s^d$ to be of the form

$$\underline{\underline{A}}_s^d = \left[\underline{\underline{1}} - \underline{\underline{\theta}}^d \right]^{1/2} \tag{5.60a}$$

$$\underline{\underline{B}}_s^d = \left[\underline{\underline{\theta}}^d \right]^{1/2} \tag{5.60b}$$

ensures that equation (5.54a) is valid. Equation (5.60a) also satisfies the limiting condition (5.58), as is easily shown using (5.59) and the binomial expansion. A consequence of the relation (5.59) is that the strength of the reset, governed by $\underline{\underline{\theta}}$, will vary over the course of the trajectory if the damping matrix $\underline{\underline{\beta}}$ is time dependent. Such is the case for the ZDA damping matrix, by virtue of its dependence on the gas-surface interaction potential.

All that remains is to recover from equations (5.60) the original matrices $\underline{\underline{A}}$ and $\underline{\underline{B}}$. Inverting the orthogonal transformation in (5.60) gives for $\underline{\underline{A}}_s$ and $\underline{\underline{B}}_s$

$$\underline{\underline{A}}_s = \underline{\underline{T}} \left[\underline{\underline{1}} - \underline{\underline{\theta}}^d \right]^{1/2} \underline{\underline{T}}^T \tag{5.61a}$$

$$\underline{\underline{B}}_s = \underline{\underline{T}} \left[\underline{\underline{\theta}}^d \right]^{1/2} \underline{\underline{T}}^T. \tag{5.61b}$$

Equations (5.61) evidently satisfy (5.50) and (5.54b); (5.61a) also must fulfill (5.56), since (5.60a) meets the requirement (5.58). Finally,

$$\underline{\underline{A}} = \underline{\underline{M}}^{-1/2} \underline{\underline{T}} \left[\underline{\underline{1}} - \underline{\underline{\theta}}^d \right]^{1/2} \underline{\underline{T}}^T \underline{\underline{M}}^{1/2} = \underline{\underline{S}} \left[\underline{\underline{1}} - \underline{\underline{\theta}}^d \right]^{1/2} \underline{\underline{S}}^{-1} \tag{5.63a}$$

$$\underline{\underline{B}} = \underline{\underline{M}}^{-1/2} \underline{\underline{T}} \left[\underline{\underline{\theta}}^d \right]^{1/2} \underline{\underline{T}}^T \underline{\underline{M}}^{1/2} = \underline{\underline{S}} \left[\underline{\underline{\theta}}^d \right]^{1/2} \underline{\underline{S}}^{-1}, \tag{5.63b}$$

where $\underline{\underline{S}} = \underline{\underline{M}}^{-1/2} \underline{\underline{T}}$. Equations (5.63) satisfy (5.43) and (5.54c) for a damping matrix of the form given in equation (5.31), as desired. They also reduce to equation (5.40) when $\underline{\underline{\beta}}$ is diagonal, for which case $\underline{\underline{T}} = \underline{\underline{1}}$.

The remainder of Chapter V discusses the implementation of the theory presented in this and the previous section. The next section is devoted to a description of the potential energy surface used in the calculations for NO scattering from lithium fluoride. Section D outlines the computational procedure for applying the reduced equations of motion via the partial velocity reset.

C. Potential Energy Surface

The potential energy surface for the gas-surface interaction in these studies is the same one employed by Lucchese and Tully[3] to investigate the scattering of NO from the (001) face of LiF. It consists of three parts: a long-range dispersion, an ion-dipole interaction and a short-range repulsion. The LiF crystal is modeled as a lattice of 128 ions (two layers of eight rows of eight ions each) sitting atop a bulk continuum. The various terms in the gas-surface potential include pair-wise interactions of the gas diatom with each ion in the lattice, plus integral approximations for the interactions with the bulk. This particular potential was chosen because it affords the opportunity to compare the results of calculations using the reduced equations of motion (ZDA approximation) for the NO/LiF(001) system with the extensive calculations of Lucchese and Tully in reference 3. This section defines the coordinate system used in the calculations and describes the functional form of each term of the potential.

The laboratory coordinate frame for this work is established as shown in Figure 24. The origin is placed in the plane of the surface

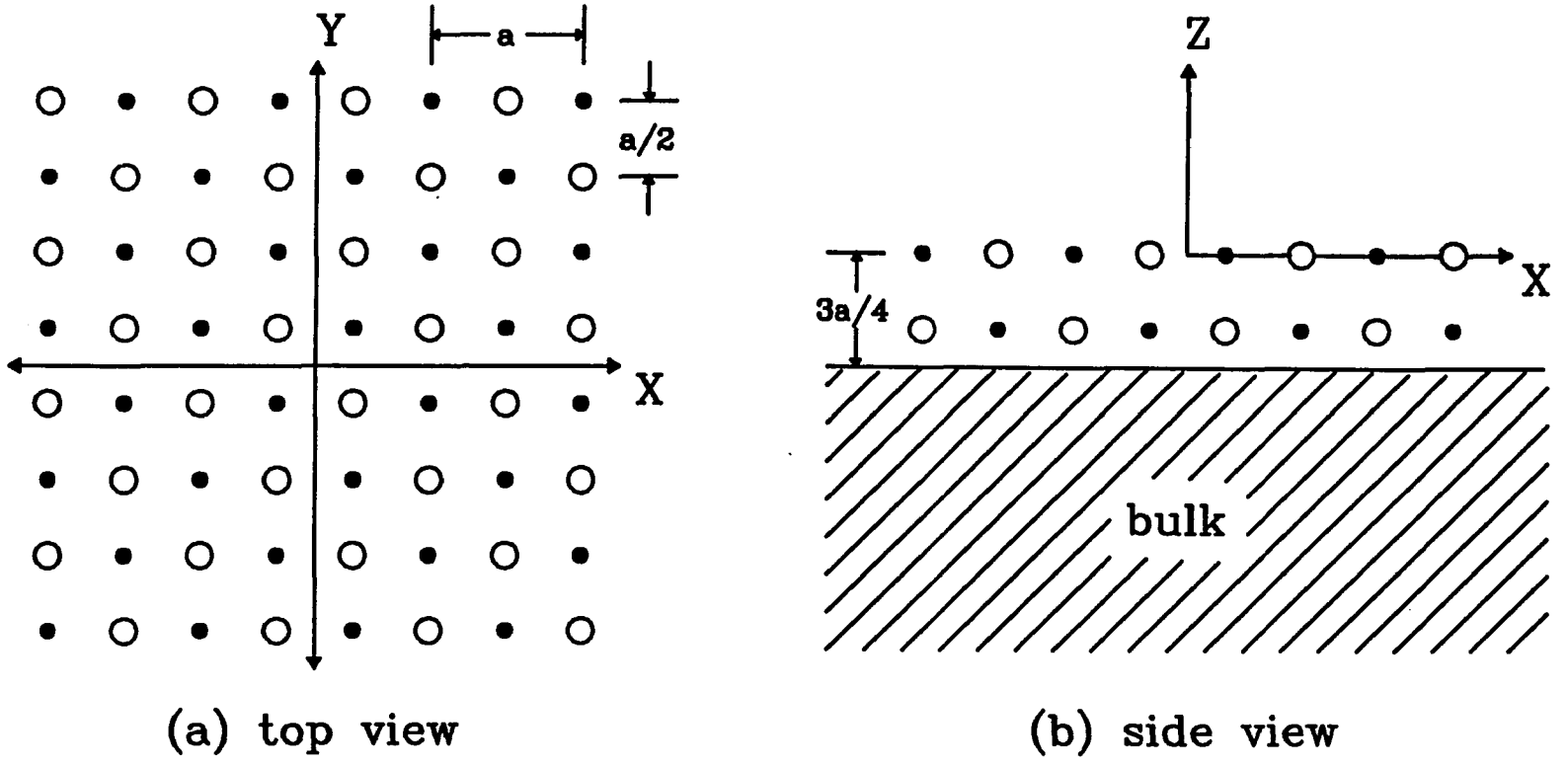

Figure 24. Surface model and coordinate system for NO/LiF calculations.

layer of the crystal, at the center of the square formed by the four central ions of the layer. The XY plane is taken to be the surface plane, with the positive Z axis pointing upward. The X and Y axes lie parallel to the rows of surface atoms in the lattice. Since there are eight rows of eight ions each in a given plane of the surface lattice, this choice of origin and orientation of the coordinates means that the lattice extends a distance $\pm 7a/4$ from the origin in both the X and Y directions, where a is the lattice constant (the distance between ions of the same type in a given row of the lattice). The row spacing, which equals the nearest-neighbor distance, is a/2. Since the lattice contains only two layers, the surface of the bulk continuum is assumed to lie at $Z_{bulk} = -3a/4$, which would be halfway between the second and third layers if the latter were present. The bulk extends to $\pm\infty$ in the X and Y directions and to $-\infty$ in the Z direction, and is assumed to contain a number density n_{bulk} of ions of each type. For LiF, a = 4.02 Angstroms[104b] and $n_{bulk} = 0.061297$ atoms/Å^3.[3]

The expression used for the long-range dispersion potential between the gas diatom and an ion s in the surface lattice is[3]

$$V_{disp} = \frac{-3\, U_{mol}\, U_s}{2(U_{mol} + U_s)R^6} \left\{ \alpha_{mol}\alpha_s + \frac{1}{3}\alpha_s(\alpha_{\parallel} - \alpha_{\perp})_{mol}\, P_2(\cos\theta) \right\}, \quad (5.64)$$

where U_{mol} and U_s are the ionization potentials of the gas diatom and the surface ion, respectively, α_{mol} and α_s their total polarizabilities, $(\alpha_{\parallel} - \alpha_{\perp})_{mol}$ is the polarizability anisotropy of the diatom, and $P_2(\cos\theta)$ is the Legendre polynomial $\frac{1}{2}(3\cos^2\theta - 1)$. R denotes the

magnitude of the distance vector $\vec{R}$ from the surface ion to the diatom center of mass, and θ is the angle between $\vec{R}$ and the diatom relative position vector $\vec{r}$. Equation (5.64) arises as the first term in the dispersion part of the multipole expansion of the long-range interaction potential between an atom and a linear molecule in the gas phase.[120]

Calculation of $\vec{R}$ and $\cos\theta$ is straightforward. One obtains $\vec{R}$ as the difference between the laboratory frame position vectors $\vec{R}_{cm}$ of the diatom center of mass and $\vec{R}_s$ of the surface ion, while $\cos\theta$ is found from the definition of the dot product of two vectors, expressed as[86]

$$\cos\theta = \frac{\vec{r} \cdot \vec{R}}{r\,R} = \frac{x\,X + y\,Y + z\,Z}{r\,R}, \qquad (5.65)$$

where x,y,z and X,Y,Z are the Cartesian components of $\vec{r}$ and $\vec{R}$, respectively, and r, the diatom internuclear distance, is the magnitude of $\vec{r}$. The dependence of the diatom total polarizability upon r is included using the expression[3]

$$\alpha(r) = \alpha(r_e) + \frac{d\alpha}{dr}(r - r_e), \qquad (5.66)$$

where r_e is the equilibrium separation of the diatom. A similar expression is used for the variation of the polarizability anisotropy. Since the perpendicular component $\alpha_\perp$ of the polarizability does not change very much as r changes, one can approximate the derivative of the anisotropy as the derivative of the parallel component $\alpha_\parallel$ of the polarizability. From the definition $\alpha = (\alpha_\parallel + 2\alpha_\perp) / 3$, it is apparent that $(d\alpha_\parallel/dr) = 3(d\alpha/dr)$ if $\alpha_\perp$ is taken to be a constant. Thus it is easy to

estimate the derivative of $\alpha_{\parallel}$ from that of α. To get the total dispersion potential due to the surface lattice, equation (5.64) is summed over the surface ions s.

To evaluate the contribution to the dispersion energy due to the ions in the bulk, one can integrate equation (5.64) over the extent of the bulk. The resulting expression is[3]

$$V^{b}_{disp} = \frac{-\pi\, n_{bulk}\, U_{mol}\, U_s}{4(U_{mol} + U_s)(Z_{cm} - Z_{bulk})^3} \times \left\{ \alpha_{mol}\alpha_s + \frac{1}{6}\alpha_s(\alpha_{\parallel} - \alpha_{\perp})_{mol}\, P_2(\cos\theta_n) \right\}, \qquad (5.67)$$

where Z_{cm} is the distance of the diatom center of mass above the crystal and θ_n is the angle between $\vec{r}$ and the surface normal (laboratory Z axis).

If the gas diatom has a dipole moment, this dipole will interact with the ions in the surface. The form of the ion-dipole potential V_{id} used here[3] treats the dipole as two equal and opposite charges separated by a distance r, each of which interacts with each ion in the surface via a Coulomb potential:

$$V^{j,s}_{Coul} = \frac{q_j\, q_s}{R_{js}}, \qquad (5.68)$$

where q_j is the charge (in esu) on atom j in the diatom (j = 1 or 2), q_s the charge of ion s in the surface lattice, and R_{js} the magnitude of the distance vector $\vec{R}_{js}$ from ion s to atom j. The charges q_1 and q_2 of the atoms in the dipole are found from $q_{1,2} = \mp\, \mu(r) / r$, in which the

dipole moment $\mu(r)$ as a function of r is given by an expression analogous to equation (5.66). The ion-dipole potential due to the surface lattice is calculated by summing equation (5.68) over both j and s. In the integral approximation, the contribution of the positive ions in the bulk of the crystal exactly cancels that of the negative ions, so that the contribution of the bulk to the ion-dipole interaction is zero.

The short-range potential used here is based on a pairwise repulsive interaction of the form[3]

$$V_{rep}^{j,s} = \frac{C_{12}^{js}}{R_{js}^{12}}, \tag{5.69}$$

where the C_{12}^{js} are constants. Since there are two atoms in the molecule and two types of ion in the surface, four such C_{12}^{js} are required. Recalling that the Lennard-Jones C_{12} coefficient is proportional to σ^{12}, where σ is the Lennard-Jones distance parameter, one can relate any pair of these constants by the expression[3]

$$\frac{C_{12}^{j's'}}{C_{12}^{js}} = \left[\frac{\sigma_{j's'}}{\sigma_{js}}\right]^{12}, \tag{5.70}$$

where σ_{js} is the Lennard-Jones distance parameter for the repulsive interaction of atom j in the diatom and ion s in the lattice. The various σ_{js} can be estimated from the arithmetic combining rule[105] $\sigma_{js} = \frac{1}{2}(\sigma_j + \sigma_s)$, using for σ_j the van der Waals radius of gas atom j and for σ_s the ionic radius of surface ion s. This work, following reference 3,

uses $\sigma_{Li^+} = 0.68$ Å and $\sigma_{F^-} = 1.33$ Å, and assumes $\sigma_N = \sigma_O = 1.8$ Å. This latter assumption means that each atom in the diatom interacts identically with a given surface ion, thus reducing to two the number of repulsive constants to be determined. Since these are related by equation (5.70), there is only one independent parameter, which is chosen using a nonlinear least-squares fit so that the overall potential has the desired well depth.[3] The contribution to the repulsive potential due to the surface lattice is calculated by summing equation (5.69) over j and s. Integrating (5.69) shows the contribution from the bulk to be[105]

$$V_{rep}^{b} = \sum_{j} \frac{\pi\, n_{bulk} \left\{ C_{12}^{j+} + C_{12}^{j-} \right\}}{45\, (Z_j - Z_{bulk})^9}, \tag{5.71}$$

where Z_j is the distance of atom j above the crystal, and +/− designates the type of surface ion.

In addition to the gas-surface interaction, a potential for the free diatom must be chosen to completely describe the overall potential energy surface. In these calculations the diatom potential selected is a Morse function, using the experimentally-determined gas-phase values of the equilibrium separation r_e and the dissociation energy D_0^0. The Morse well depth D_e and exponential parameter β are found from these values using the standard formulae[93d]

$$D_e = D_0^0 - \tfrac{1}{2}\omega_e, \tag{5.72}$$

$$\beta = \omega_e \left[\frac{2\pi^2 c\mu}{\hbar\, D_e}\right]^{1/2} = 0.121821 \frac{(\text{cm}^{-1}\ \text{amu})^{1/2}}{\text{Å}}\, \omega_e \sqrt{\frac{\mu}{D_e}}, \tag{5.73}$$

where ω_e is the vibrational frequency of the diatom, μ is its reduced mass, c is the speed of light and $\hbar$ is Planck's constant divided by 2π. Equation (5.73) produces β in $Å^{-1}$ if ω_e and D_e are in cm^{-1} and μ is in amu. These two equations provide an easy means for calculating D_e and β for a given ω_e. This proves useful in sets of calculations that vary ω_e.

Table 4 contains the values of the various parameters used in the gas-surface interaction potential. The sources from which these quantities were obtained are given in reference 3. Lucchese and Tully[3] fit their NO/LiF potential to a well depth of 90 meV, and observed that this minimum occurred when the NO molecule was lying nearly parallel to the surface, in a plane containing the surface normal and the two Li^+ ions nearest the origin, with the center of mass at a height Z_{cm} = 1.6 Å above the surface. These observations were confirmed in this work as a check.

D. Computational Details

This section completes Chapter V with a discussion of the computational procedure actually used in the calculations. First, an outline of the structure of the trajectory code is presented, and then specific details within that framework are given.

In general, calculations are performed in sets of 100 trajectories, in order to allow direct comparison with the results of Lucchese and Tully.[3] At the start of a set of trajectories, the spectroscopic constants[121] and masses for the NO molecule and the parameters for the gas-surface interaction potential are input to the trajectory code, along

Table 4. Parameters for the NO/LiF interaction potential.

Potential Term	Parameter	Value
V_{disp}	U_{Li^+}	75.619 eV
	U_{F^-}	3.465 eV
	U_{NO}	9.26436 eV
	α_{Li^+}	0.0286 Å
	α_{F^-}	0.759 $Å^3$
	α_{NO} [a]	1.74 $Å^3$
	$(\alpha_{\parallel} - \alpha_{\perp})_{NO}$ [a]	0.759 $Å^3$
	$d\alpha_{NO} / dr$	3.0 $Å^2$
V_{id}	q_{Li^+} [b]	0.97 e [c]
	μ_{NO} [a]	− 0.1474 D
	$d\mu_{NO} / dr$	2.19 D/Å
V_{rep}	$C_{12}^{(N,O-Li^+)}$	8.5083 eV [d]
	$C_{12}^{(N,O-F^-)}$	139.00 eV [d]

Table 4 (continued)

NO Morse potential	r_e	1.15077 Å
	D_0^0	6.496 eV
	ω_e^e	1904.20 cm^{-1}

[a] value at $r = r_e$.

[b] $q_{F^-} = -q_{Li^+}$.

[c] $e = 4.803 \times 10^{-10}$ esu.

[d] the corresponding value in reference 3 is larger by a factor of 12, due to an error.

[e] this is the experimental value; in some calculations, other values of ω_e are employed - see Chapter VI.

with the initial values of quantum numbers v and J, collision energy E_T and incidence angle θ_i which characterize that set. In some cases, J and/or θ_i for a set is determined by Monte Carlo selection. The coordinates of the atoms of the surface lattice are also established at the start of the set. After this set-up procedure, the trajectories are run. To calculate a single trajectory, the following scheme is applied. The initial conditions for the trajectory are selected using the procedures given in section B of Chapter II, based on the supplied values of v, J, E_T and θ_i; the other necessary quantities needed for the initialization are selected randomly, except for the initial height Z_{in}, which is always 9.5 Å, following reference 3. In sets of trajectories in which J is randomly selected, the required cumulative probability distribution is constructed from a Boltzmann rotational distribution at temperature T_{rot}; the value of T_{rot} is input to the code. After the initialization procedure, Hamilton's equations of motion (2.28) are integrated, using the potential energy function discussed in section C, for a time Δt_r. At this point, the velocities are reset by calling a subroutine which is described in the next paragraph.

The reset subroutine performs the following algorithm. The Laplacian of the gas-surface potential with respect to the coordinates of each surface atom is calculated, and the weight factors W^S are found using equation (5.30). The elements of the coupling matrix $\underline{\underline{K}}^{SA}$, given by equation (5.14b), are also evaluated. (In the calculations reported in Chapter VI, all 128 ions of the surface lattice are included in the calculation of the weight factors and coupling-matrix elements, unless explicitly stated otherwise.) From these quantities the matrix elements

of the symmetric matrix $\underline{\underline{\beta}}^{sym}$ are calculated using (5.31) (without the factor of m_a^{-1}). Then the matrix product $\underline{\underline{M}}^{-\frac{1}{2}}\underline{\underline{\beta}}^{sym}\underline{\underline{M}}^{-\frac{1}{2}}$ is diagonalized to obtain the matrices $\underline{\underline{\beta}}^{d}$ and $\underline{\underline{T}}$, according to (5.57). Using these, equation (5.59) yields $\underline{\underline{\theta}}^{d}$ and equation (5.63) $\underline{\underline{S}}$ and $\underline{\underline{S}}^{-1}$. The atom velocities are obtained from the center-of-mass and relative momenta (the integration variables) using (2.6b), and reset according to equations (5.42) and (5.63). The Maxwellian velocities used in the reset are found from $v^{\xi} = (kT/m)^{\frac{1}{2}}\,\xi^{G}$, where ξ^{G} is a Gaussian random number generated from an inverse-error-function approximation subroutine supplied by J. C. Tully.[122] Finally, the new velocities are converted back to momenta using equations (2.4c-d).

After the resetting is complete, the EOM are integrated for another reset interval and again reset. This cycle is repeated until the end of the trajectory has been reached. A trajectory is considered over either when the center of mass of the gas molecule reaches a height of 10 Å above the surface in less than 10 picoseconds (a "direct" trajectory by the definition of Lucchese and Tully[3]), or when the trajectory has been integrated for 15 picoseconds. In the latter case the trajectory is flagged as a "trapped" trajectory[3] after 10 picoseconds, but the integration is continued for up to five picoseconds more, in order to obtain final quantities of interest for at least some of these instances. If a trajectory does not reach 10 Å within 15 picoseconds, no final analysis is performed. Quantities of interest include the final quantum numbers v and J, the final scattering angles Θ_f and Φ_f, and the final energies of translation, vibration and rotation. After the entire set of trajectories has been run, it is analyzed in terms of final average energies and

Table 5. Final energies for various Runge-Kutta integrator step sizes in the absence of the gas-surface potential. Initial energies were E_T = 217.000 meV, E_V = 349.504 meV and E_R = 0.739850 meV.

h (psec)	E_T^f (meV)	E_V^f (meV)	E_R^f (meV)
0.00050	217.000	348.652	0.739845
0.00033	217.000	349.392	0.739850
0.00025	217.000	349.478	0.739850
0.00020	217.000	349.495	0.739850

accommodation coefficients for the various degrees of freedom, for direct comparison with the results of reference 3. Procedures for the final analysis of each trajectory and for the set of trajectories are outlined in section D of Chapter II.

The reset interval for these calculations was chosen to be 0.001 picoseconds, in order to give a maximum value for the matrix elements of $\underline{\underline{\theta}}^d$ of about 0.25. For this small a step size, the computational overhead in the DEROOT integrator subroutine package[99] used for the vibrational quantum number initialization procedure makes it too slow to use for integrating the trajectories. Thus a simple fourth-order classical Runge-Kutta integrator[100a] was employed. The routine is coded to make n steps per reset interval, where $n \geq 1$ can be chosen as desired to minimize the error. The integrator was tested in several ways. First,

Hamilton's equations were integrated for 1.65 picoseconds in the absence of the gas-surface potential for several step sizes h, to test energy conservation. Based on the results, which are contained in Table 5, further tests were performed only on the two smallest values of h, 0.00025 and 0.00020 picosecond. Next a single trajectory with a typical set of initial conditions ($v = 1$, $J = 1.5$, $E_T = 217$ meV, $\theta_i = 30°$) was integrated in the presence of the gas-surface interaction to test against exact results. Table 6 shows the result without application of the velocity reset, for which the exact result is the initial energy, which should be conserved; Table 7 contains results with resetting, for which the "exact" result is taken as integration by DEROOT, since the damping is non-conservative. For a Runge-Kutta algorithm of order r, the global error is $O(h^r)$,[100b] so that the ratio of errors for the two step sizes considered here should be approximately $(25/20)^4 \approx 2.4$; the error ratios from Tables 6 and 7 are ~1.7 and ~4.3, indicating that the integrator works properly. Based on the results of Tables 6 and 7, the 0.00020 picosecond step size (5 steps per reset) was chosen. With this value of h, the integrator is roughly forty to fifty percent faster than DEROOT for the 0.001 picosecond reset interval used here. The calculations were performed on the Cray X-MP at Sandia National Laboratories in Albuquerque, New Mexico, and the Cray X-MP at the Ohio Supercomputer Center in Columbus, Ohio. A typical direct trajectory took 28 seconds of CPU time; a typical trapped trajectory took 131 seconds.

Since the model used for the LiF surface is a lattice of only 128 ions sitting atop a bulk continuum, some provision must be made to keep the gas molecule above the center of the lattice. In particular, the

Table 6. Comparison of integrators for trajectories without velocity resetting.

Trial[a]	E_{TOT}^{f} (meV)	Error[b] (10^{-6} eV)	CPU minutes[c]
Exact[d]	567.003	———	———
DEROOT	566.984	19	294
0.00020	566.981	22	160
0.00025	566.966	37	127

[a] numerical entries are step sizes in picoseconds.

[b] Error = (exact result) − (result for this trial).

[c] for a VAX 11/750.

[d] exact result is the initial value of E_{TOT}.

Table 7. Comparison of integrators for trajectories with velocity resetting.

Trial[a]	E^{f}_{TOT} (meV)	Error[b] (10^{-6} eV)	CPU minutes[c]
Exact[d]	266.266	———	612
0.00020	266.263	3	377
0.00025	266.253	13	301

[a]numerical entries are step sizes in picoseconds.

[b]defined as in Table 6.

[c]for a VAX 11/750.

[d]exact result is the DEROOT calculation.

center of mass of the diatom is constrained to lie above the square formed by the four ions nearest the origin (the "central square"). In order to do this, the location of the center of mass is checked once per reset interval; if the center of mass has moved out of the central square, the code calls a subroutine which adjusts the coordinates and momenta of the diatom accordingly. Since there are two types of ion in the lattice, at alternating lattice sites, there are two distinct cases which must be considered.

The first case is shown in part (a) of Figure 25. Here the diatom moves in such a way that it crosses boundaries in both the X and Y directions in the same reset interval, so that the new square over which it moves is identical to the central square. Thus, to return the molecule to the central square, the row spacing a/2 is added to or subtracted from each of the coordinates X_{cm} and Y_{cm} as necessary. No adjustments of the momenta are necessary in this case.

Part (b) of Figure 25 depicts the more common situation, in which the gas molecule only crosses one boundary of the central square. Now the new square is not identical to the central square, but rather to the central square *rotated by ninety degrees*. Therefore, to return the diatom to the central square, the relative and center-of-mass position and momentum vectors are rotated around the Z axis by $(-1)^n \times 90°$, where $n \geq 0$ is the number of previous rotations, after which either X_{cm} or Y_{cm} is adjusted by $\pm a/2$ as necessary to obtain the required positioning. For example, in the figure the molecule has moved out of the central square in the X direction, to point A. To correct this, the position and momentum vectors are first rotated by +90° (that is, counterclockwise)

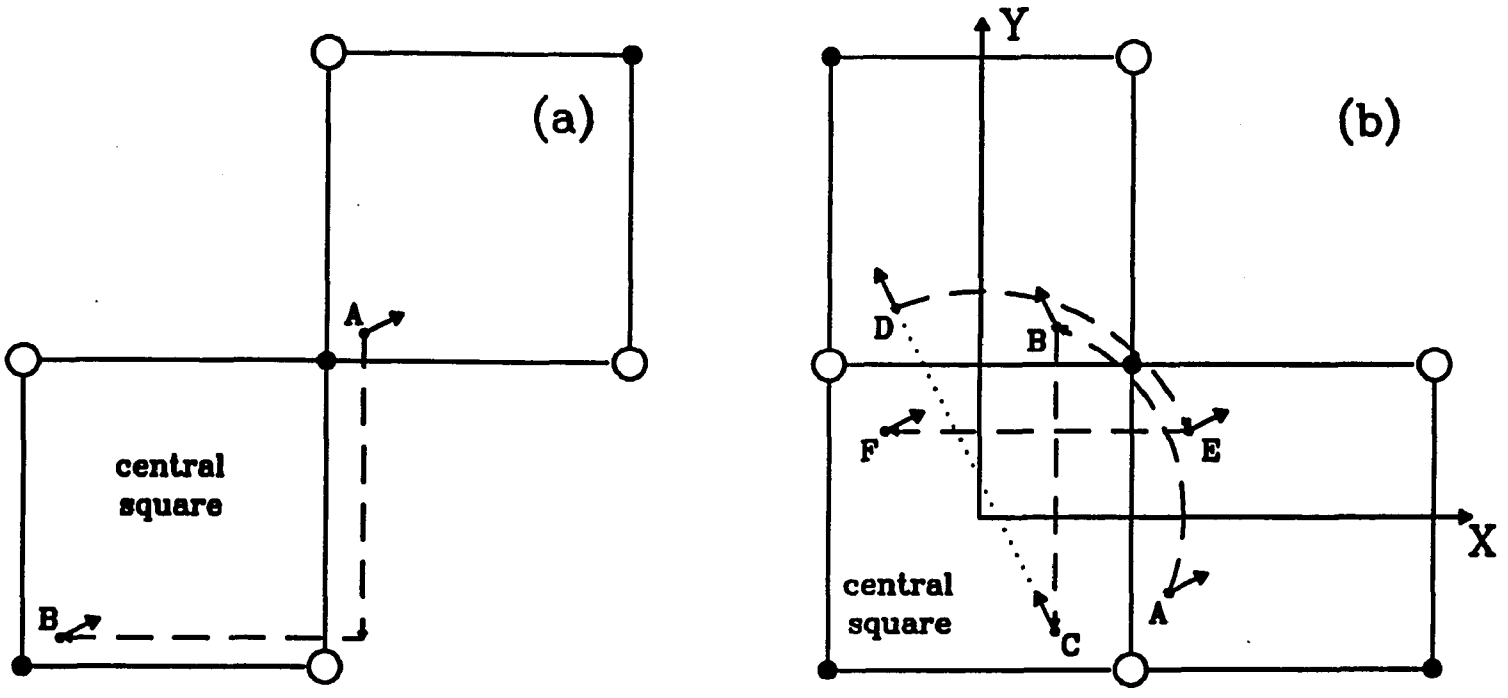

Figure 25. Illustration of the procedure for keeping the diatom above the central square of the lattice for (a) the case that boundaries in both the X and Y directions are crossed, and (b) the case that only one boundary is crossed. Solid arrows represent diatom positions and velocities. Straight dashed arrows denote displacement of position vectors by a/2 in the specified direction; curved dashed arrows denote rotation of position and momentum vectors by 90° in the specified direction.

around Z, to point B. The relative as well as center-of-mass vectors must be rotated since both sets are used to calculate the atom position and momentum vectors. At this point, what was X motion now lies along Y, and the Y motion lies along −X. To get back to the central square at point C, a/2 is subtracted from the new value of Y_{cm}. From here the integration can be continued. Eventually the molecule will again cross a boundary, say at point D. To return to the central square, the vectors are this time rotated by −90° (that is, clockwise) to reach point E, and then a/2 subtracted from X_{cm} to reach point F, from which the integration continues. As a consequence of using this procedure, one can see that the coordinates and momenta which are being integrated do not necessarily represent the actual coordinates and momenta in the lab frame, which are in some cases useful to have. Thus, a record is maintained by the computer program of how many times a/2 has been added to or subtracted from each center-of-mass coordinate, so that the actual coordinates and momenta can be extracted from the integrated set, using another subroutine provided for this purpose.

The final topic to be discussed is the implementation of a modified velocity reset procedure which may be used for rigid-rotor trajectories or in cases for which the vibrational frequency of the gas diatom is much larger than the Debye frequency of the surface. In these situations one desires to ensure that the component of the relative momentum along the internuclear axis is the same after the velocity reset as it was before. In these calculations this is done in a very straightforward way. Before the center-of-mass and relative momenta are converted to atom velocities in the reset procedure, the vector component of the

relative momentum along the internuclear axis, $\vec{p}_r^{old}$, is calculated according to the following equation:

$$\vec{p}_r^{old} = (\hat{u} \cdot \vec{p}^{old}) \hat{u}, \tag{5.74}$$

where $\vec{p}^{old}$ is the relative momentum before the reset and $\hat{u} = \vec{r} / r$ is a unit vector along the internuclear axis. Next the velocities are reset as usual, and converted back to center-of-mass and relative momenta. Then the component of the new relative momentum perpendicular to the internuclear axis, $\vec{p}_p^{new}$, is found from

$$\vec{p}_p^{new} = \vec{p}^{new} - (\hat{u} \cdot \vec{p}^{new}) \hat{u}, \tag{5.75}$$

where $\vec{p}^{new}$ is the relative momentum after the reset. Finally, the relative momentum in the modified reset scheme, $\vec{p}^{mod}$, is calculated as

$$\vec{p}^{mod} = \vec{p}_r^{old} + \vec{p}_p^{new}, \tag{5.76}$$

thus ensuring that the component of $\vec{p}$ along the axis is not changed by the velocity reset.

CHAPTER VI

EVALUATION OF THE REDUCED EQUATIONS OF MOTION FORMALISM

This chapter presents an evaluation of the reduced equations of motion model for the case of diatom-surface scattering, based on the results of applying the REOM (in the ZDA approximation) to the scattering of NO from LiF(001). Extensive calculations on this system have been performed by Lucchese and Tully (LT) using the stochastic trajectory method;[3] these calculations provide a reliable standard by which to measure the accuracy of the REOM results. Section A of this chapter compares the ZDA and LT results and section B discusses the evaluation of the ZDA approximation.

A. Comparison of ZDA and LT Results

As discussed in Chapter I, the NO/LiF study by LT had a twofold purpose: to evaluate the experimental results of Zacharias and coworkers,[84] who reported measurements of the vibrational deactivation probability of NO(v=1) scattering from LiF(001), and to investigate general features of vibrational energy transfer in molecule-surface collisions. In their calculations, LT employed a shell model[123] for the forces among the ions of the LiF lattice. They used a P-zone of 32 ions, four rows of four ions in each of two layers, and included in the gas-surface interaction

potential contributions from the 96 ions encircling the P-zone, 48 in each of the first and second layers. Their gas-surface interaction for the resulting lattice of 128 ions (eight rows of eight ions in two layers) is the one described in section C of Chapter V; the only difference is that in LT the central sixteen ions of each layer are not frozen at their equilibrium positions. LT chose their initial conditions for the internal motion of the NO molecule using different procedures than those described in Chapter II. Consequently the initial energies reported in the following discussion in some cases differ slightly from those given by LT.

Six sets of calculations (labeled I through VI in the present discussion) have been performed in this work for direct comparison to the corresponding sets in reference 3. Calculation I involves initial conditions to match those in the experiments of Zacharias *et al*. Calculation II examines rotational and translational energy accommodation of the NO molecule to the surface. Calculations III through VI probe the dependence of the energy transfer in a diatom-surface collision upon the diatom vibrational frequency, the temperature of the surface and the initial translational and vibrational energies of the diatom, respectively.

Listed in Table 8 is a comparison of ZDA and LT results for calculation I. In these sets of trajectories, the initial translational energy is 217 meV and the initial incidence angle 30°. The initial NO vibrational energy is 349.5 meV, corresponding to $v = 1$. The initial rotational quantum number was selected from a Boltzmann distribution at 8.5

Table 8. Comparison of LT, ZDA and MZDA results for Calculation I.

(a) vibrational accommodation coefficients α_v

T (K)	LT	ZDA	MZDA
300	0.0044 ± 0.002	0.73 ± 0.03	0.0093 ± 0.002
600	———	0.76 ± 0.04	0.019 ± 0.003
900	0.014 ± 0.007	0.73 ± 0.04	0.025 ± 0.007

(b) average final translational energy $\langle E_T^f \rangle$ (meV)

T (K)	LT	ZDA	MZDA
300	107 ± 6	87 ± 6	87 ± 6
600	———	149 ± 11	137 ± 10
900	161 ± 9	186 ± 14	181 ± 14

Table 8 (continued)

(c) average final rotational energy $\langle E_R^f \rangle$ (meV)

T (K)	LT	ZDA	MZDA
300	26 ± 2	21 ± 3	25 ± 3
600	———	35 ± 4	32 ± 4
900	57 ± 6	60 ± 7	49 ± 7

Kelvin, which resulted in an average initial rotational energy for the direct trajectories of 0.6 meV. Sets of trajectories were performed with these initial conditions at surface temperatures of 300, 600 and 900 K. The important result from part (a) of Table 8 is that the ZDA greatly overestimates the vibrational energy accommodation of the NO to the surface, indicating much too great a degree of damping of the vibrational motion. This occurs because the vibrational frequency of NO (1904.20 cm^{-1}) is very much larger than the Debye frequency for LiF (502 cm^{-1}); as mentioned at the end of section A of Chapter V, in this case the adiabatic approximation is inappropriate. For this reason, Calculation I was also performed using the modified velocity-reset procedure outlined in Chapter V, and the results included in Table 8, under the heading "MZDA". It is apparent that the MZDA is a much better approximation than the ZDA when the vibrational frequency is much greater than the Debye frequency; however, in a range of vibrational frequencies comparable to the Debye frequency, where the adiabatic approximation is not valid but appreciable damping of the vibration should occur, neither the ZDA nor the MZDA work very well. Both the MZDA and LT results show an approximately threefold increase of α_v, the vibrational energy accommodation coefficient (EAC), as T_s changes from 300 K to 900 K.

Parts (b) and (c) of Table 8 show the LT, ZDA and MZDA values for the average final translational and rotational energies of the NO molecule from Calculation I. Both of the ZDA results show a stronger dependence of the final translational energy on the surface temperature than that of LT. The (M)ZDA result at 900 K is unusual compared to the calculations discussed below, in which the ZDA consistently overestimates

the damping of the translational motion, resulting in a smaller value of $\langle E_T^f \rangle$ compared to LT. The ZDA calculations of $\langle E_R^f \rangle$ agree with those of LT to within the standard error at both temperatures.

Figure 26 presents angular distributions for NO scattered from LiF, for the Calculation I initial conditions with a surface temperature of 300 K. Part (a) shows the LT distribution of the final polar scattering angle θ_f, while (b) through (d) contain the MZDA results for θ_f for various ranges of the azimuthal scattering angle Φ_f. For the purposes of Figure 4, Φ_f is referenced to either the positive or negative X axis, whichever is nearer; forward scattering is then indicated by positive values of θ_f and backward scattering by negative θ_f. The LT result has $|\Phi_f| \leq 15°$; the distribution is broad but definitely peaked around the specular angle (+30°). Of the 94 direct trajectories[124] from which the LT distribution is taken, 47 of them fell within the ±15° acceptance window on Φ_f.[125] In contrast, only eight of the 76 direct trajectories from the MZDA calculation fell within this window, while a window of ±30° contained 23 trajectories (an increase of 15) and the ±45° window 35 (an increase of 12, and 46% of the total). From this it is clear that the MZDA predicts much more out-of-plane scattering than LT's method. In fact, Figures 26(b-d) indicate that the MZDA result favors forward scattering, but both the forward and backward scattering are evenly distributed in the azimuthal angles. Similar results are obtained for the ZDA calculation. This uniformity reflects randomization, due to the use of the velocity reset technique, of the Y component of the center-of-mass momentum, which was originally zero since the initial motion is in the XZ plane.

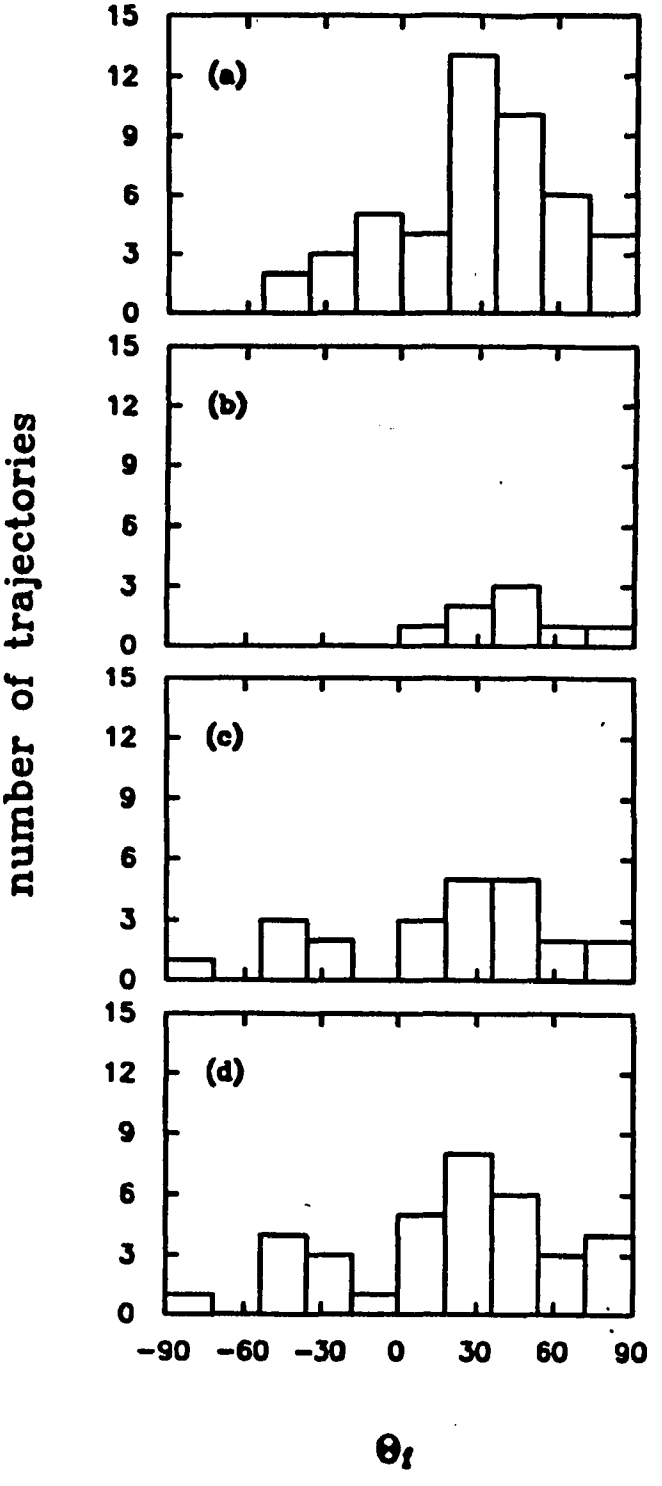

Figure 26. Comparison of LT and MZDA angular distributions (Calculation I). Part (a) is the LT result, which has an out-of-plane acceptance of $|\Phi_f| \leq 15°$. Parts (b)-(d) are MZDA results with $|\Phi_f| \leq 15°$, 30° and 45°, respectively. The specular angle is $\theta_f = +30°$.

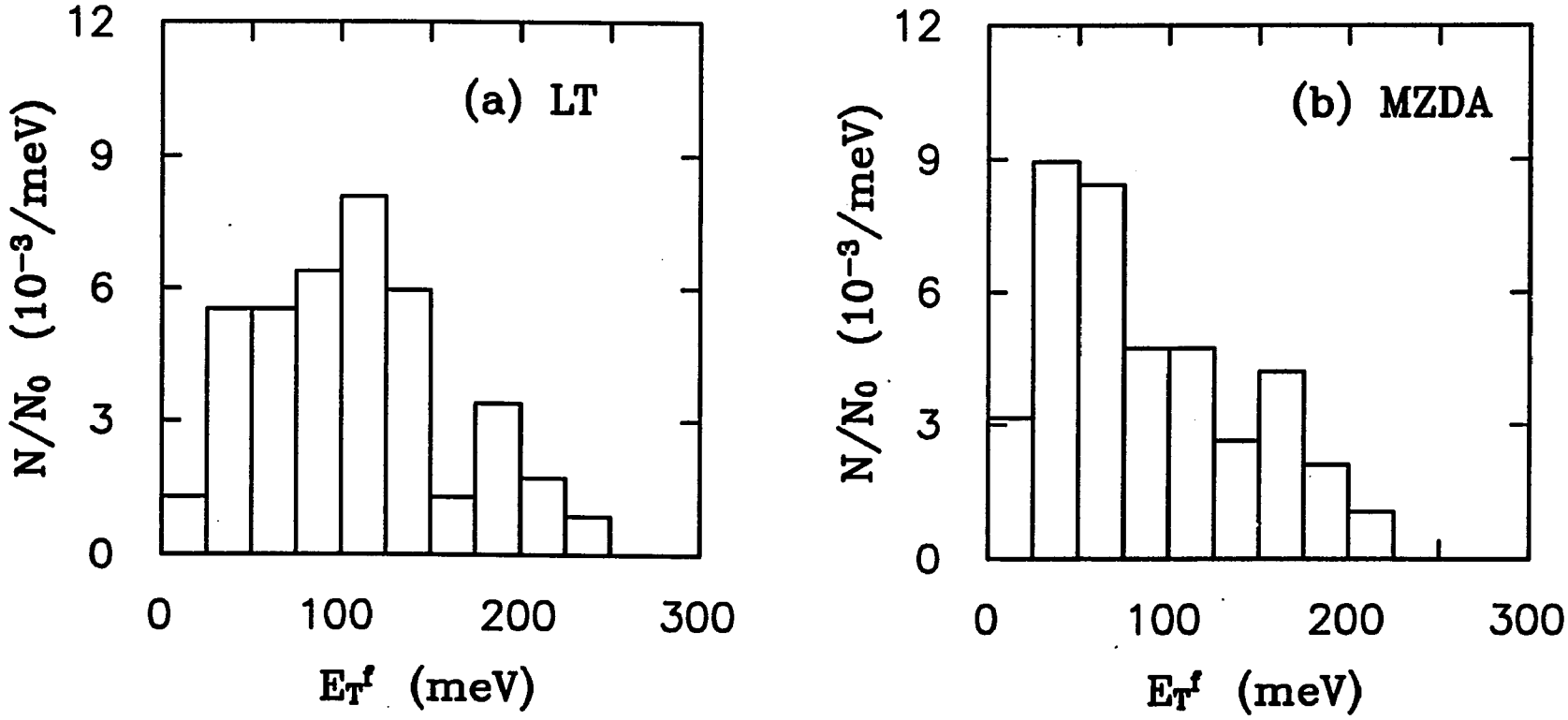

Figure 27. Comparison of LT and MZDA final translational energy distributions (Calculation I). The distributions are normalized to integrate to unity.

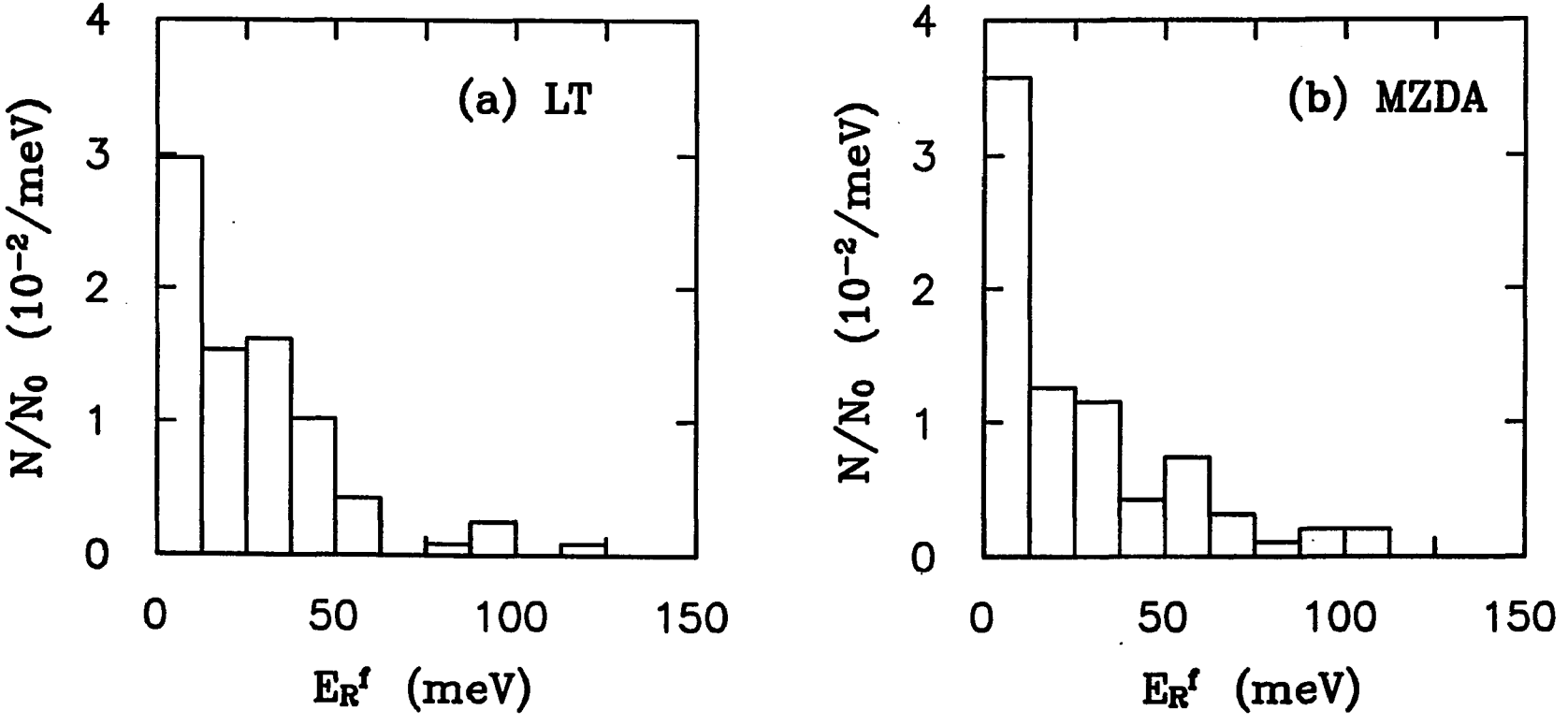

Figure 28. Comparison of LT and MZDA final rotational energy distributions (Calculation I). The distributions are normalized to integrate to unity.

Figures 27 and 28 display the computed final translational and rotational energy distributions, respectively, from Calculation I with a surface temperature of 300 K. In each figure, part (a) is the LT result and part (b) is the MZDA result. The distributions are normalized so that they integrate to unity,[126] which accounts for the units of meV^{-1}. In both figures the MZDA distribution is cooler than that given by LT. A cooler translational energy distribution indicates that the damping of the translational energy is too great, since the molecule started with an initial translational energy, 217 meV, which is greater than the average energy of an equilibrium translational distribution, $2kT_s$ = 51.7 meV. A cooler rotational distribution in this context means that the MZDA underestimates the rotational excitation produced by the collision with the surface, since the initial rotational energy is small. This underestimation is due to excessive damping of the rotational motion by the surface and/or loss to the surface of some translational energy that otherwise would have contributed to rotational excitation via T → R energy transfer in the collision. As the ensuing paragraphs will show, these results are typical of most of the calculations performed here, for which the initial conditions are large translational energies (compared to $2kT_s$) with nearly zero rotational energies.

Calculation II investigates the degree of NO translational and rotational energy accommodation to the LiF surface. To do this, two sets of rigid-rotor trajectories were run with the surface temperature set to 900 K. One of these sets had the initial translational energy set equal to twice the thermal average value, that is, $E_V^i = 4kT_s$ = 310 meV, while

Table 9. Comparison of LT and ZDA results for Calculation II.

quantity	LT	ZDA
α_T	0.43 ± 0.06	0.64 ± 0.09
α_R	0.62 ± 0.08	0.40 ± 0.11

the rotational energies (quantum numbers) were selected from a Boltzmann distribution at 900 K; from this a translational EAC, α_T, was extracted. The other set of trajectories had the initial translational energy set to the average value of 155 meV, and the initial rotational quantum number chosen to be J = 26.5, to give a rotational energy of 154 meV, which is roughly twice the thermal average value, $2kT_s$. This yielded a rotational EAC, α_R. In both calculations the initial incidence angle θ_i was selected from a cosθ distribution. The accommodation coefficients from LT and from this work are given in Table 9. It is evident that the translational motion is damped too much by the ZDA, since the accommodation coefficient α_T is larger than the LT value. This is in accord with the result of Calculation I mentioned above. Table 9 also shows that the ZDA noticeably underestimates the rotational energy accommodation to the surface. It is not immediately obvious why this is the case, but it does suggest, at least, that the more important cause of the underestimation of the rotational excitation by the ZDA in calculation I and elsewhere

Table 10. Initial conditions for vibrational motion in Calculation III.

ω_e (cm^{-1})	E_V^i (meV)[a]	quantum number
500	92.7	1.00
625	144.9	1.38
750	208.5	1.76
875	284.4	2.15
1000	371.6	2.54

[a]energies differ from LT's by less than 0.7 meV at each ω_e.

is the decreased T → R energy transfer due to the overdamping of translational motion by the surface.

Calculation III is a study of the effect on the vibrational energy accommodation of varying the NO vibrational frequency. To do this, sets of trajectories were run with an initial translational energy of 217 meV, incidence angle of 30° and rotational quantum number $J = \frac{1}{2}$. The vibrational frequency and initial vibrational energy were given the values listed in Table 10; also shown are the values of the vibrational quantum number v used to obtain the energy at each frequency. These energies were chosen such that the classical vibrational amplitude was

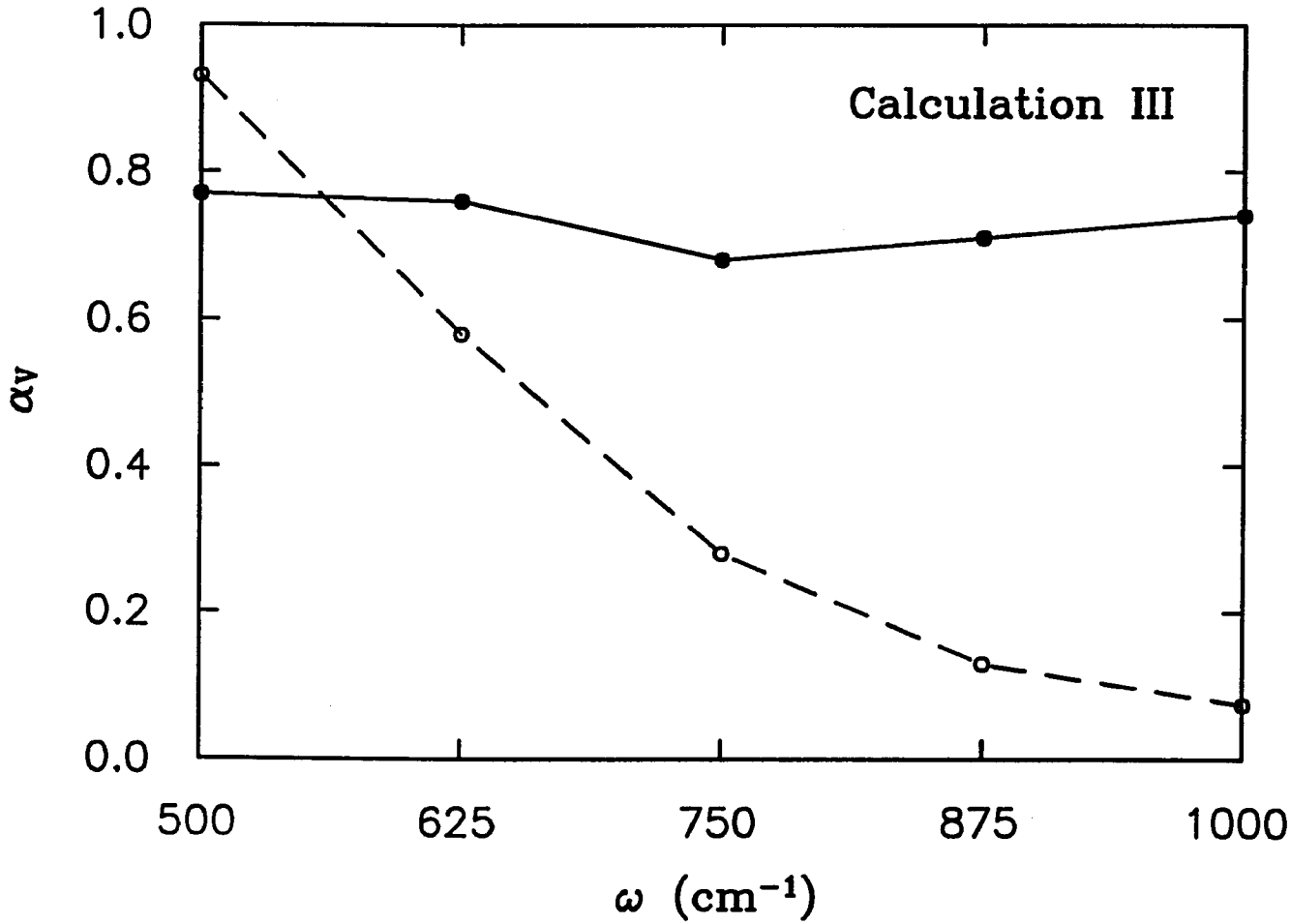

Figure 29. Vibrational EAC as a function of diatom vibrational frequency (Calculation III). Filled circles are MZDA results, open circles are LT results.

the same in all five sets of trajectories.[3] Since the vibrational accommodation is of interest here, the ZDA rather than the MZDA approximation was used. The resulting vibrational accommodation coefficients are plotted in Figure 29. This calculation clearly shows the breakdown of the ZDA approximation in treating the vibrational motion. The plot of the LT values shows an exponential decay of the vibrational relaxation rate with increasing frequency,[3] while the ZDA plot is insensitive to the vibrational frequency. Also, the ZDA values for the vibrational accommodation are too large. This behavior can be traced to the failure of the adiabatic approximation used to derive the ZDA model, due to the relative sizes of the surface and gas molecule vibrational frequencies. Calculation III also reveals that the final average translational and rotational energies of the scattered NO molecules, computed by both LT and ZDA, are insensitive to the diatom frequency, although the ZDA again overestimates the translational damping and underestimates the rotational excitation.

Calculation IV illustrates the effect on the energy transfer of varying the surface temperature. The initial translational energy was again chosen to be 217 meV, the incidence angle was 30°, and the initial rotational quantum number was $J = \frac{1}{2}$. The ZDA approximation was used, with the diatom vibrational frequency set at 750 cm^{-1} and the initial vibrational energy fixed at 209 meV (as in the third set of trajectories in Calculation III). Four sets of trajectories were computed. For the first of these the ions of the surface were, in the LT case, frozen at their equilibrium positions; for the present calculations this means that the velocity reset was not applied during the trajectory. The other

Table 11. Comparison of LT and ZDA values of the average final energies for various degrees of freedom, from the set of fixed-surface trajectories in Calculation IV.

average energy	LT	ZDA
$\langle E_T^f \rangle$	168 ± 6	171 ± 6
$\langle E_V^f \rangle$	201 ± 4	197 ± 4
$\langle E_R^f \rangle$	56 ± 5	57 ± 5

three sets of trajectories set the surface temperature at zero, 300 and 900 Kelvin, respectively. The "frozen surface" results, as contained in Table 11, show clearly that the integration procedures used in these calculations and in LT's work were equivalent, since for each degree of freedom the final average energies from each method were within one standard error of each other. The outcome of the surface temperature variation is plotted in Figure 30. The ZDA does very well for both the translational and rotational motion as far as reproducing the trend shown in the LT calculations. In fact, the ZDA average final rotational energy lies within one standard error of the LT result at each of the surface temperatures, although the deviations indicate that the ZDA again underestimates the rotational excitation. The damping of the translational motion by the ZDA at lower temperatures is overestimated, as before, although at 900 K the values are identical.

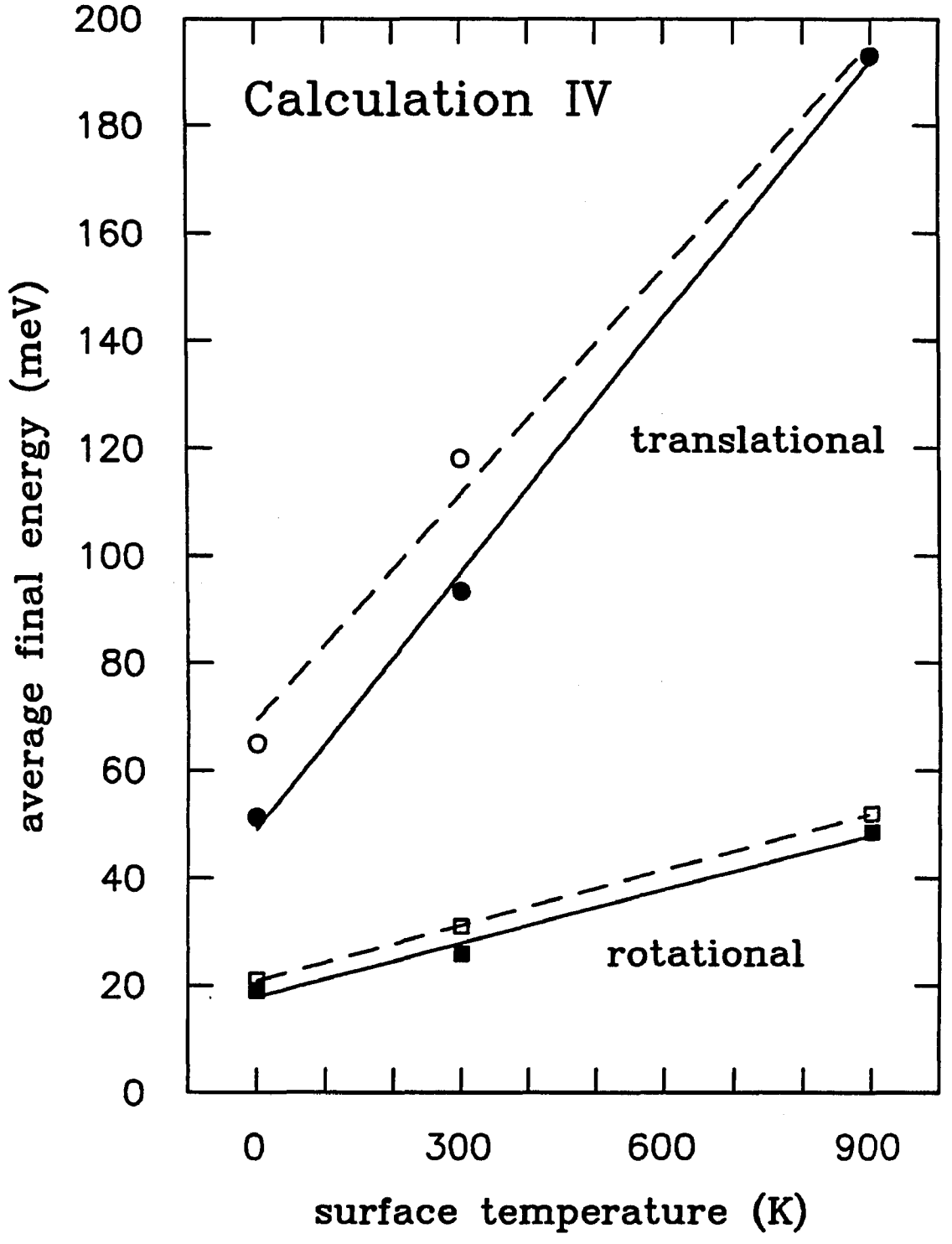

Figure 30. Comparison of ZDA and LT results for the surface-temperature dependence of the average final translational and rotational energies (circles and squares, respectively), from Calculation IV. Filled symbols are the ZDA results; open symbols are the LT results. The solid and dashed lines are least-squares fits to the ZDA and LT data, respectively.

Figures 31 and 32 present comparisons of results for Calculation V, which investigates the initial translational energy dependence of the energy transfer. The four sets of trajectories run in this calculation all had a surface temperature of 300 K, an incidence angle of 30°, an initial rotational quantum number of $\frac{1}{2}$ and vibrational frequency and initial vibrational energy of 750 cm^{-1} and 209 meV, respectively. The initial translational energy had the values 217, 434, 650 and 867 meV. As Figure 31 demonstrates, the ZDA reproduces the LT trend of insensitivity of the final translational energy to changes in the initial translational energy, but overestimates the damping of translation by about 30%. The final rotational energies are within one standard error of each other for all these initial translational energies, although just barely so at 434 meV, as Figure 32 shows. Figure 32 also indicates that the rotational excitation is underestimated (slightly) by the ZDA calculation in this case as well.

Calculation VI looks at the effect of varying the initial vibrational energy of the diatom while holding its frequency fixed (which is complementary to Calculation III). The initial conditions for the trajectories were the same as those in Calculation V, except that the initial translational energy was fixed at 217 meV and the initial vibrational energy set at 209, 371 and 742 meV. Figure 33 shows that the same behavior of the ZDA approximation as observed in the previous calculations manifests itself here as well. The ZDA reproduces the LT trend of insensitivity to the initial vibrational energy, but overestimates the damping of translation and underestimates the rotational excitation. The average final rotational energy from the ZDA calculation matches the LT

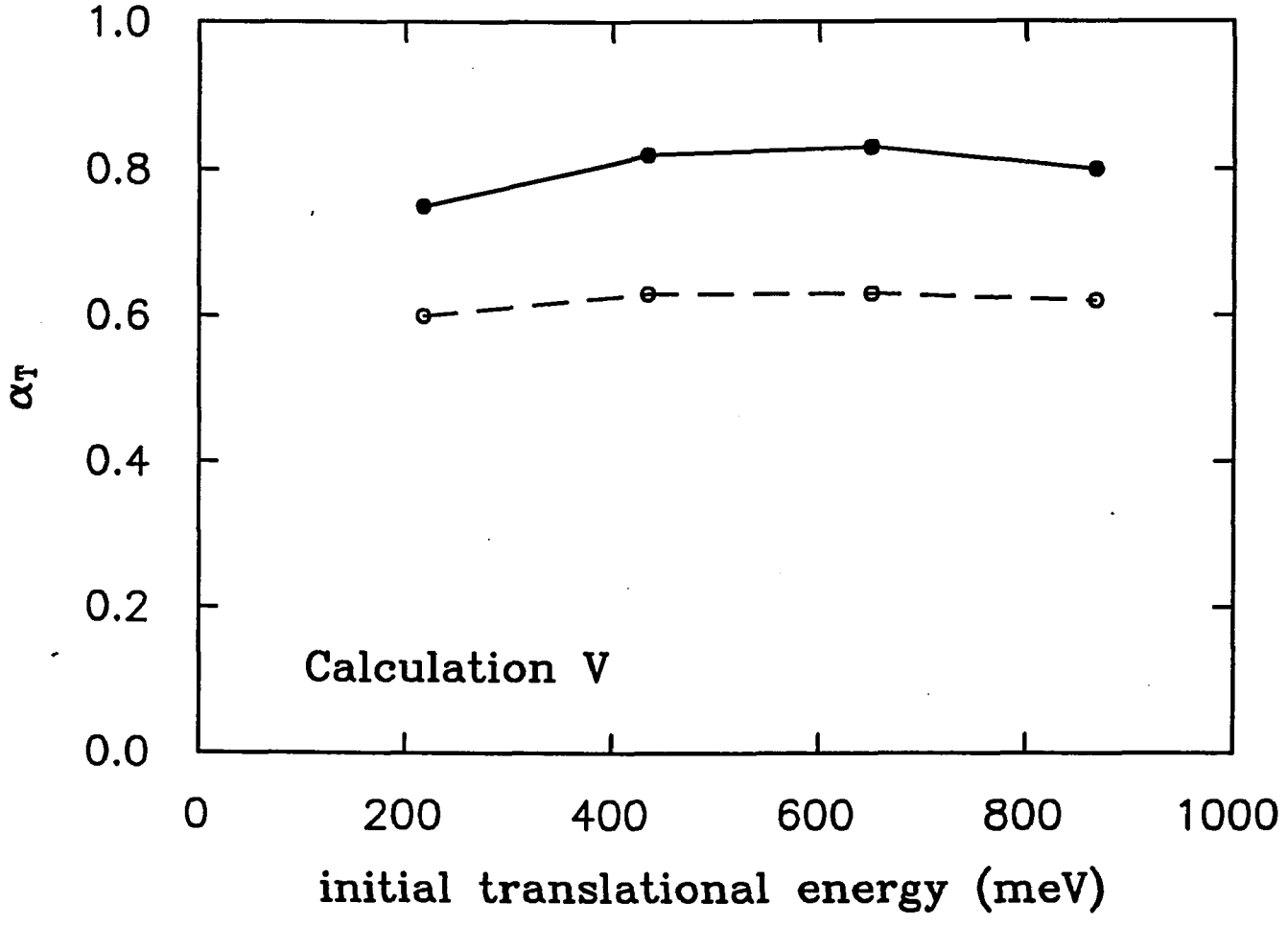

Figure 31. Translational EAC as a function of initial translational energy (Calculation V). Filled and open symbols are ZDA and LT results, respectively.

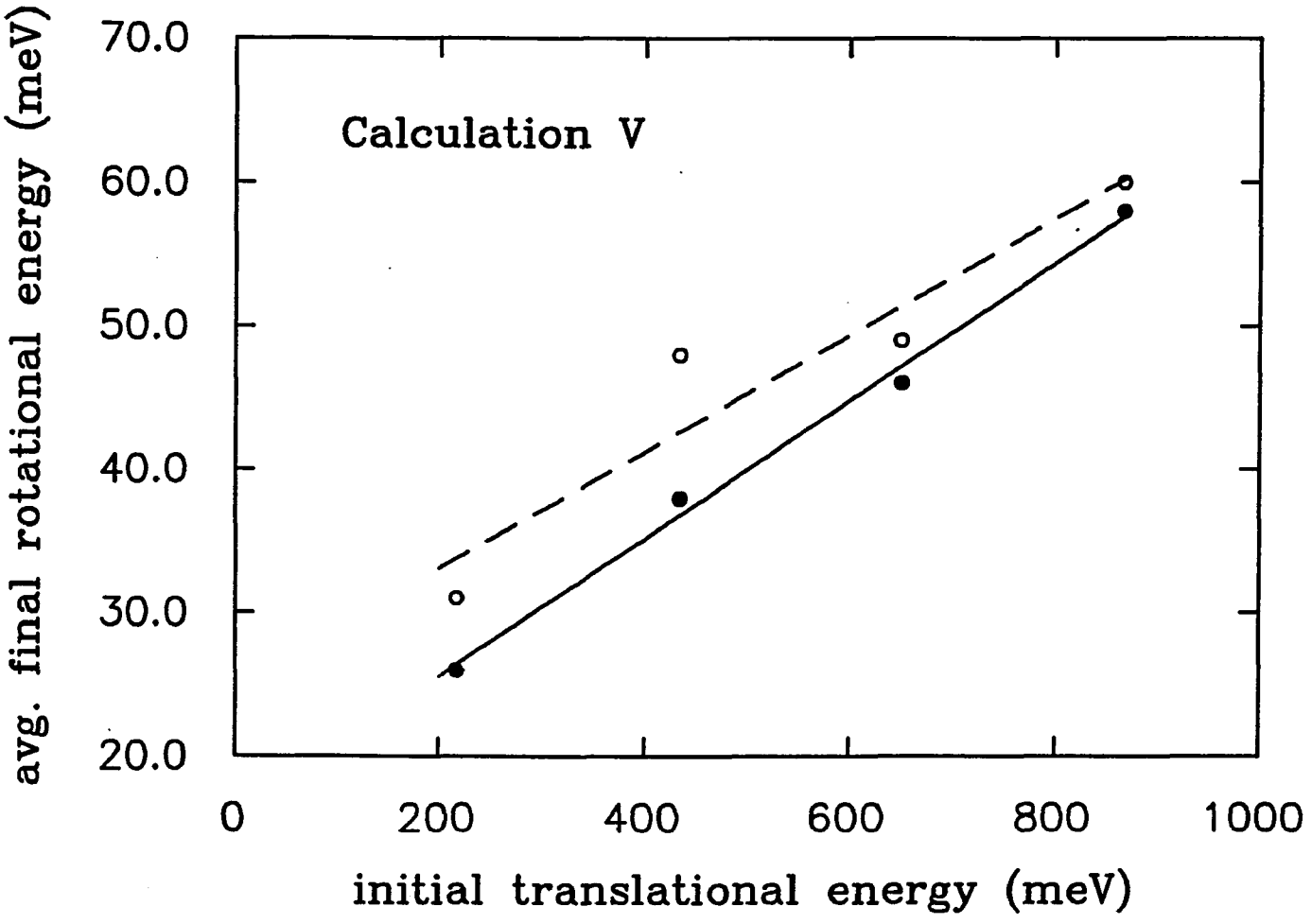

Figure 32. Comparison of ZDA and LT results for the dependence of the average final rotational energy on the initial translational energy (Calculation V). Filled and open circles represent ZDA and LT results, respectively, and the lines are least-squares fits to the data.

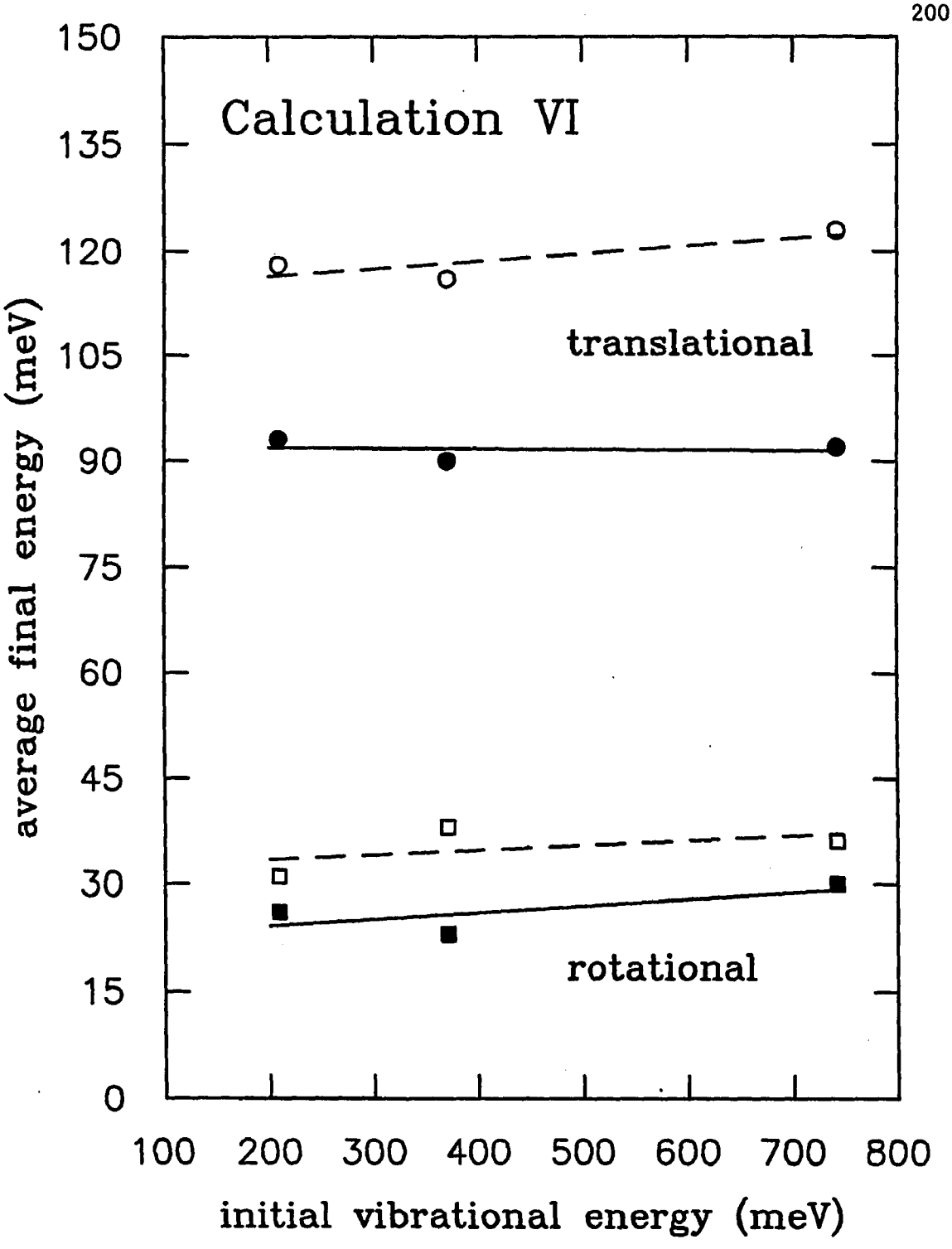

Figure 33. Comparison of ZDA and LT results for the initial-vibrational-energy dependence of the average final translational and rotational energies (circles and squares, respectively), from Calculation IV. Filled and open symbols are the ZDA and LT results, respectively, and the lines are least-squares fits to the data.

result to within one standard error, except at 371 meV.

B. Discussion and Evaluation of the Reduced Equations of Motion Model

In assessing the ZDA reduced equations of motion model as applied in this work several points can be discussed. These include the ability of the ZDA approximation to reproduce trends seen in the more exact LT calculation; the inability to handle vibrational motion accurately when the vibrational frequency is on the order of the Debye frequency of the solid; the tendency of the ZDA results to overestimate damping of the translational motion and underestimate rotational excitation, compared to the LT results; and the amount of CPU time required for a typical calculation of 100 trajectories using the ZDA approximation as compared to using the stochastic trajectory method of LT. The following paragraphs address these issues.

As noted in the preceding section, the ZDA calculations did very well in reproducing the trends observed in the LT results with respect to the dependence of the average final translational and rotational energies on the various initial conditions. In fact, the agreement in the results for the rotational motion is remarkably good, often within the standard error of the computations. The rotational period τ_{rot} for an NO molecule having a rotational energy of 50 meV, which is typical of the largest values of the final average rotational energy presented in section A, is roughly ten times the vibrational period τ_{vib} of LiF (as estimated from the Debye frequency). Thus one could expect that the adiabatic approximation is valid with respect to the rotational motion.

This suggests that the ZDA approximation should do a good job on the rotational motion, which appears to be the case. In a similar vein, one can estimate whether the translational motion should be adiabatic by comparing the collision time t_c to the vibrational period τ_{vib}. In particular, if the ratio t_c/τ_{vib} (called the *adiabaticity parameter* ξ) has a value $\xi \geq 1$, then the collision is adiabatic.[127] For E_T = 217 meV, which was most commonly used in these calculations, and assuming the "range" of the gas-surface interaction to be 3 Å, one finds that $\xi \sim 4$. This suggests that the adiabatic approximation should hold for the translations as well.

Another way to evaluate the performance of the ZDA approximation with respect to the translational motion is to use the results of Diestler and Riley,[2] who applied the FA and ZDA models to scattering from a Rosenstock-Newell lattice via a Morse interaction potential, and compared them to their numerically exact results[88] for the same system. Table 1 of reference 2 contains "figures of merit" for judging the approximations against the exact results for wide ranges of the collision parameters (the ratio E^* of the incident energy to the well depth, the ratio m^* of the gas species mass to the surface species mass, and the ratio k^* of the force constant of the gas-surface interaction to that of the lattice interaction). For all the calculations done in this work, the energy ratio lies in the range $1 \leq E^* \leq 10$; the ratio of the mass of NO to the mass of the surface species is $m^* \approx 2$ or 4, depending on whether the average or reduced mass of LiF is used. To find a rough estimate of k^*, the second derivative of the gas-surface interaction potential with respect to Z_{cm} at the minimum was calculated as an

estimate of the gas-surface force constant. The lattice force constant was estimated from[128] $k_{lat} = \frac{1}{2} \mu \omega_L^2$, where μ is the reduced mass of LiF, by setting the cutoff frequency ω_L equal to the Debye frequency. The above expression for k_{lat} reduces to that used in reference 2 when all the surface atoms have the same mass. The resulting estimate for k^* is 0.23. The corresponding figures of merit from reference 3 for these E^*, k^* and two m^* are "+/0" or "+", where "+" indicates an error of between 10% and 25%, "0" an error of between 25% and 200%, and the / indicates a change in the figure of merit as E^* varies over its range. Thus one can see that the error in the translational energies for the ZDA calculation done here, which are typically around 30% compared to the "exact" LT results, is about as good as could be expected for the set of collision parameters corresponding to the NO/LiF system. It is interesting to note, however, that in reference 2 the FA and ZDA approximations underestimate the loss of translational energy to the surface; this is not the case in the present work.

As well as the reduced equations of motion seem to do for the translation and rotation, the results of the preceding section also show that this model breaks down for diatom vibrational frequencies which are on the order of or larger than the Debye frequency. This, again, is due to the fact that the adiabatic approximation used to derive the ZDA model is not valid for the vibrational motion in such situations. It has been shown in this work that when the vibrational frequency is very much larger than the Debye frequency, in which case direct transfer of vibrational energy to the solid is expected to be minimal, the ZDA approximation can be "repaired" in a rather ad hoc fashion by applying the

velocity reset in such a way that the vibrational momentum is unchanged. Calculation I shows that this procedure works fairly well for the NO/LiF system, but it may be difficult to predict *a priori* when such a procedure is applicable. In the regime where the diatom and surface frequencies are comparable, no such convenient method to fix the reduced equations of motion presents itself. The REOM should handle the vibrational motion acceptably for cases in which the vibrational frequency is small compared to the Debye frequency. However, at least for diatomic molecules, such cases almost never occur, since LiF has one of the highest Debye frequencies of solids of practical interest,[104c] and most diatomic molecules of interest have vibrational frequencies on the order of or larger than that of NO. It should be noted that because the vibrational mode is only very weakly coupled to the translational and rotational modes in this system,[3] the fact that the ZDA calculation does poorly on the vibrational motion does not have a significant effect on its performance for the rotational and translational motion.

One trend that persisted throughout the discussion of section A was that the ZDA calculation overestimated the damping of translational motion and underestimated the rotational excitation. This implies that for this model the surface is too "soft", so that too much of the translational energy is absorbed by the surface during the collision, instead of remaining in translation or being transformed into rotational energy. In other words, the motion of the gas molecule is too strongly damped by the solid in this model. The reason for this behavior is that the "weak-coupling approximation" (WCA) used to reduce the ZDA damping matrix, equation (5.25), to the computationally more tractable form used here,

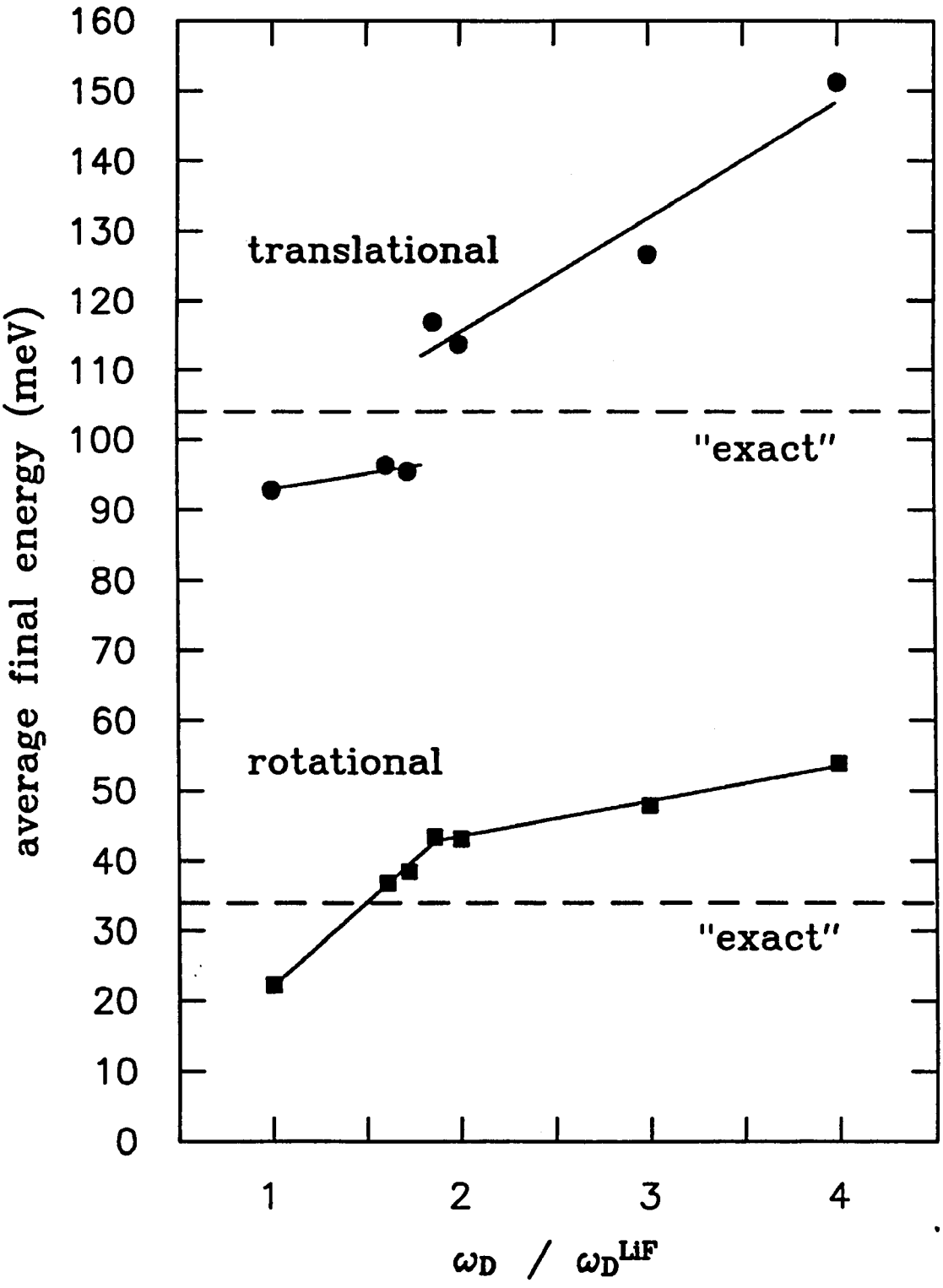

Figure 34. Dependence of final average energies on the lattice Debye frequency (ω_D^{LiF} = 502 cm^{-1}). Lines marked "exact" are LT results from set 1 of Calculation III.

equation (5.31), is not a very accurate approximation for an ionic crystal. The WCA assumes that the atoms of the lattice are only weakly coupled to each other and essentially respond independently in the presence of the gas molecule. However, in an ionic solid the Coulomb forces between the various ions are strong, long-range forces. Thus the result of invoking the WCA in this application is to underestimate the stiffness of the crystal, or, in other words, to make the lattice seem too soft. Since the Debye frequency serves as a measure of the stiffness of the crystal, a simple way to verify this diagnosis would be to treat the Debye frequency as an adjustible parameter and to look at the final translational and rotational energies as ω_D increases. The results of such a procedure are plotted in Figure 34. The calculations all had initial conditions identical to those in the first set of trajectories for calculation III, except that here the value of ω_D was varied. The abscissa in Figure 34 is labeled in units of $\omega_D^{NO} = 502\ cm^{-1}$, the experimental Debye frequency for LiF. The figure clearly shows that less energy is absorbed by the lattice as the stiffness is increased. As the stiffness is initially increased, the final average rotational energy increases rapidly while the final average translational energy increases slowly; for solid frequencies greater than $2\omega_D^{NO}$ the translational energy rises more rapidly and the rotational energy less quickly. The initial behavior suggests that the underestimation of rotational excitation by the ZDA model is due to absorption of energy by the lattice that otherwise would have gone into T → R energy transfer. As the stiffness increases more, some constraint limits the amount of T → R transfer, and the amount of translational energy lost to the surface steadily

decreases as well. The lines marked "exact" in Figure 34 indicate the energies calculated by LT for these initial conditions. From these it is apparent that this simple adjustment of the Debye frequency does not make the ZDA result match that of LT, although it is a step in the right direction. Perhaps applying the damping matrix (5.25) would do a better job, although this would be a much more difficult computational task.

In addition to the above considerations about the strength of the damping, one might also ask which parts of the potential and which atoms of the lattice contribute most significantly to $\underline{\underline{\beta}}$. To answer the first of these questions, sets of trajectories were run in which various parts of the potential were not included in the calculation of the damping matrix in equation (5.31). The initial conditions for these trajectories were the same as the T_s = 600 K ZDA set from Calculation I, and the results of the calculations for the various sets of contributions to $\underline{\underline{\beta}}$ are presented in Table 12. The results clearly show that the most important contribution to the damping of the NO motion comes from V_{id}, the ion-dipole part of the potential. When this term is included in $\underline{\underline{\beta}}$, the average final energies resemble those for inclusion of the full potential; when this term is absent, the final energies look like those for the fixed-surface set (from Calculation IV). This effect is most clearly seen in the values of $\langle E_V^f \rangle$ in Table 1. LT noticed a similar relationship between V_{id} and $\langle E_V^f \rangle$, which they explained by pointing out that distortions of the lattice from its equilibrium geometry change the force due to V_{id} from an exponentially-decreasing function of Z_{cm} to one that falls off as slowly as $1 / Z_{cm}^3$.[3]

Table 12. Effect of eliminating various parts of the gas-surface interaction potential in calculating the ZDA damping matrix.

Degree of Freedom	Parts of V_{gs} included in calculation of $\underline{\beta}$				
	none	rep	rep + disp	rep + id	all[a]
$\langle E_T^f \rangle$	171 ± 6[b]	167 ± 8	166 ± 8	155 ± 10	149 ± 10
$\langle E_V^f \rangle$	344 ± 1[c]	268 ± 9	272 ± 9	133 ± 11	123 ± 5
$\langle E_R^f \rangle$	57 ± 5[b]	55 ± 5	59 ± 6	28 ± 4	35 ± 4

[a]ZDA values from Calculation I, T_s = 600 K (Table 8).

[b]value taken from fixed-surface set in Calculation IV.

[c]MZDA value from Calculation I, T_s = 600 K (Table 8).

To address the second question mentioned in the preceding paragraph, concerning the number of atoms of the solid which make important contributions to the gas-surface energy transfer, calculations were performed in which the number of lattice ions used to compute $\underline{\beta}$ was reduced from 128 (the whole lattice) to 32 (the central 16 ions of each type, corresponding to the P zone used by LT). This procedure was applied to the sets of trajectories from Calculations I and IV; the 32-ion results for each case (I and IV) are compared to their 128-ion counterparts in

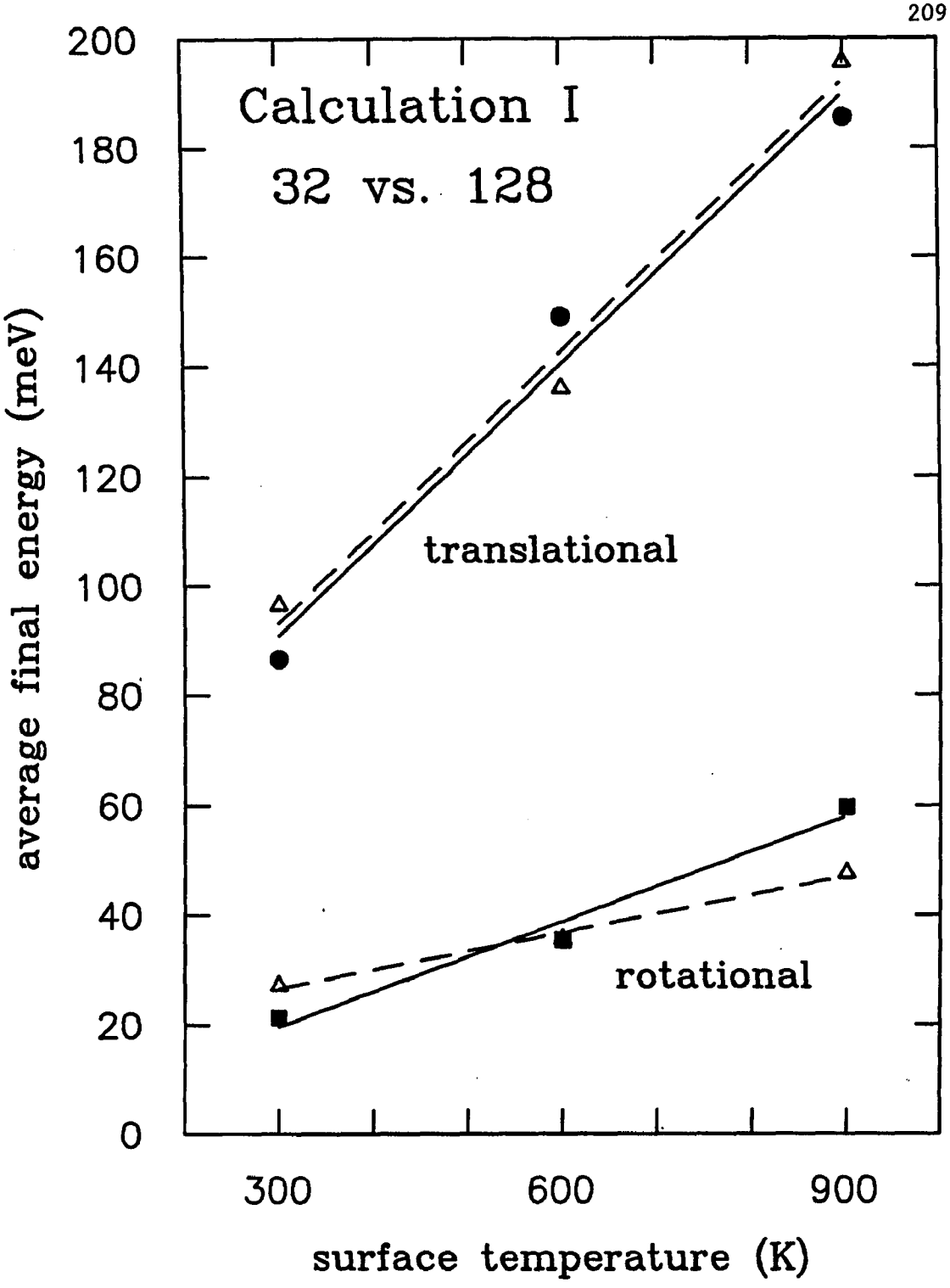

Figure 35. Effect of varying the number of ions included in calculating the damping matrix $\underline{\beta}$, using initial conditions from Calculation I (ω_{NO} = 1904.2 cm^{-1}). Filled symbols are 128-ion results and open triangles are 32-ion results. The lines are least-squares fits to the data.

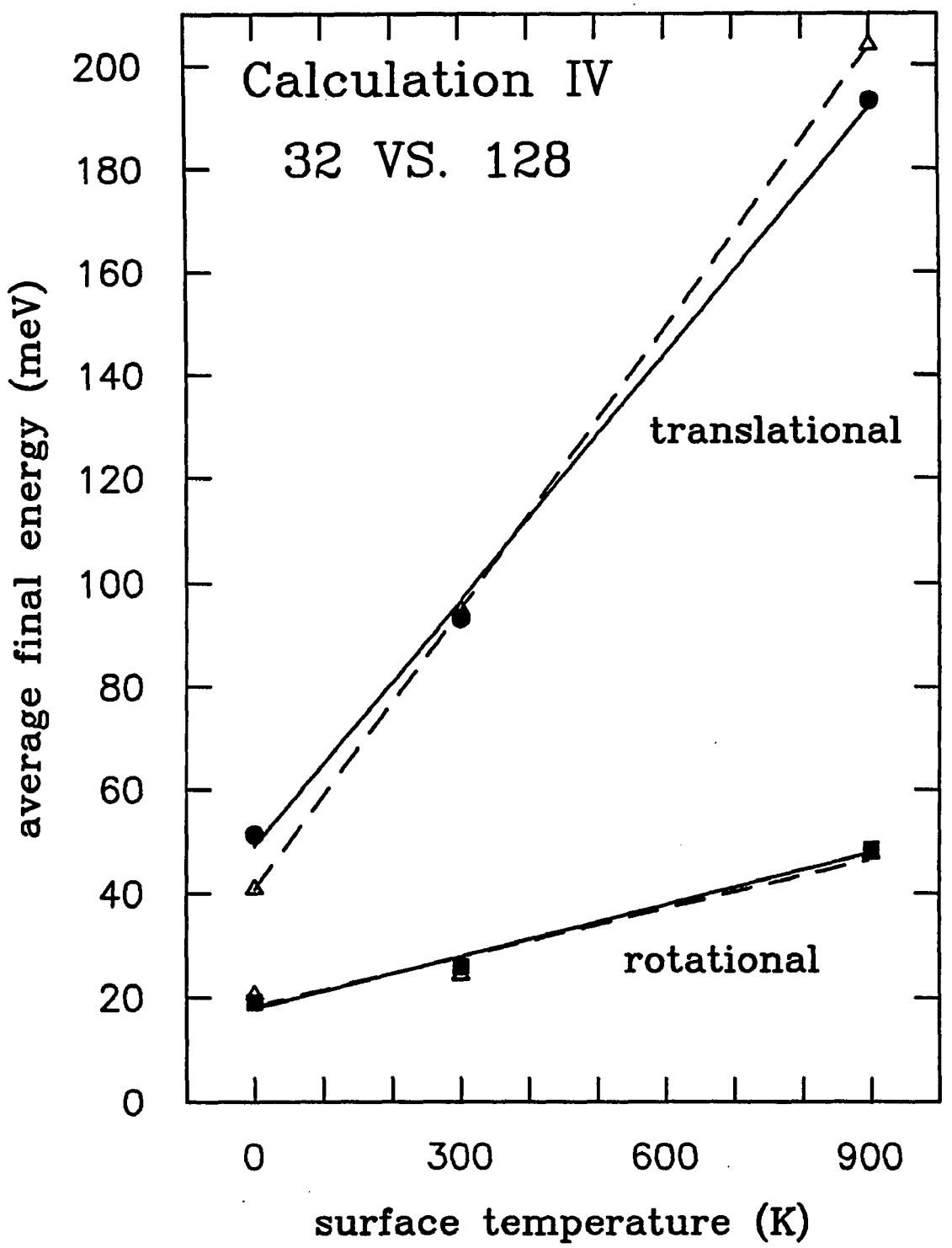

Figure 36. Effect of varying the number of ions included in calculating the damping matrix $\underline{\beta}$, using initial conditions from Calculation IV (ω_{NO} = 875 cm^{-1}). Filled symbols are 128-ion results and open triangles are 32-ion results. The lines are least-squares fits to the data.

Figures 35 and 36, respectively. As the figures indicate, there is very little difference between the 32- and 128-ion results over the range of surface temperatures involved. This means that the effects of the outermost 96 ions of the lattice make only a small contribution to the gas-surface energy transfer, which appears to justify LT's use of a 32-ion P zone.

A final point worth mentioning in evaluating the reduced equations of motion formalism concerns the issue of computer CPU time necessary to perform the calculations. Part of the reason for developing a method which does not include integrating the equations of motion of the surface atoms is the hope that computational effort will be saved in the process. For the present application to the NO/LiF scattering system, integrating the reduced equations of motion took considerably longer than the corresponding LT calculation, which involved integrating equations of motion for 32 ions of the lattice in addition to those for the gas molecule. The particular example for which information is available for comparison is the set of trajectories from calculation I having T_s = 300 K. This computation took LT 3760 CPU-seconds on a Cray 1 computer, using a step size of 0.0002 picosecond.[125] This set of trajectories included 94 direct ones and 6 trapped ones.[124] A calculation from this work most comparable with that is the result for the 600 K ZDA set from Calculation I, which had 95 direct trajectories and 5 trapped ones. Two of the trapped trajectories were integrated for the full trajectory time of 15 psec, so they would count as three LT trapped trajectories (since LT quit after 10 picoseconds). Thus, for comparison purposes, this set had six trapped trajectories. The step size used here was also 0.0002

picosecond, and the required CPU time was 4792 seconds (±10%) on a Cray X-MP; the ZDA computation took 27% longer. This is due almost entirely to the fact that the numerical integrator used in the present calculations is significantly less efficient than that used by LT. This is shown by comparing the CPU times for the fixed-surface trajectory set from Calculation IV. This set required 2271 CPU-seconds here, but only 593 seconds in the LT work.[125] A major factor causing the moving-surface calculation to take six times longer than the frozen-surface one in the LT case was the need to evaluate random forces for the 28 atoms along the P-Q interface at every time step. LT estimate that this extra work required 30-40% of the total computational effort in their moving-surface calculations.[125] In contrast, the ZDA calculation for the moving surface only required random forces for two atoms at every fifth time step.

To obtain a qualitative estimate of whether, for a given integrator efficiency, the REOM approach is faster than the stochastic trajectory method, the following reasoning may be applied. A flowtrace applied to the trajectory code used here revealed that 80.3% (±0.05%) of the CPU time is spent in the integrator, while the reset subroutine accounts for 18.9% (±0.1%). (The percentages were determined by averaging the results for a single direct (2.8 psec.) trajectory and a single trapped (12.3 psec.) trajectory; the uncertainties reflect the deviations of the individual results from the average in each case.) This means that for the set mentioned in the previous paragraph, 906 of the 4792 CPU-seconds were spent in the reset subroutine and would be required regardless of the integrator. Essentially all of the remaining 3886 CPU-seconds were

spent performing the integration. Taking the ratio of fixed-surface integration times as an estimate of the relative efficiencies of the integrators, the LT integrator would have only required 1015 CPU-seconds to do the same amount of work. Therefore, the present calculation with an integrator as efficient as LT's would only take 1015 + 906 = 1921 CPU-seconds, or 51% of the LT result. Although uncertainties in the reported CPU times and differences in the computers used imply that the above value of 1921 CPU-seconds is not accurate to 4 significant figures, it is reasonable to estimate that, in the present application, the REOM approach is roughly twice as fast as the stochastic trajectory method used by LT.

Based on the above discussion, the following evaluation of the reduced equations of motion formalism can be offered. The method can reasonably be applied to diatom-surface collision systems for which the direct vibrational energy transfer between the diatom and the lattice is expected to be small, if the collision energy is on the order of or smaller than the depth of the gas-surface interaction and if the mass of the gas molecule is on the order of or larger than the average mass of the surface atoms. The results should give good qualitative predictions of the dependence of the translational and rotational energy transfer with respect to the various system parameters, but the quantitative results are not necessarily reliable. An advantage of the method is that it provides significant computer time savings (~50% in the present application) compared to the stochastic trajectory method. The reduced equations of motion will not work very well in cases where the vibrational motion is strongly coupled to the surface, since for these cases

neither the adiabatic approximation nor the modified velocity-reset procedure provide a reasonable physical picture for the vibrational energy transfer.

REFERENCES

1. B. D. Kay and K. R. Lykke, to be published.

2. D. J. Diestler and M. E. Riley, J. Chem. Phys. 89, 4137 (1988).

3. R. R. Lucchese and J. C. Tully, J. Chem. Phys. 80, 3451 (1984).

4. J. C. Tully, J. Chem. Phys. 73, 1975 (1980).

5. M. E. Riley, M. E. Coltrin and D. J. Diestler, J. Chem. Phys. 88, 5934 (1988).

6. J. A. Barker and D. J. Auerbach, Surf. Sci. Rep. 4, 1 (1984).

7. M. C. Lin and G. Ertl, Ann. Rev. Phys. Chem. 37, 587 (1986).

8. P. L. Houston and R. P. Merrill, Chem. Rev. 88, 657 (1988).

9. R. B. Gerber, R. Kosloff and M. Berman, Comput. Phys. Rep. 5, 59 (1986).

10. R. B. Gerber, Chem. Rev. 87, 29 (1987).

11. G. Wolken, J. Chem. Phys. 59, 1159 (1973); Chem. Phys. Lett. 21, 373 (1973).

12. J. V. Lill and D. J. Kouri, Chem. Phys. Lett. 112, 249 (1984).

13. R. C. Mowrey and D. J. Kouri, Chem. Phys. Lett. 119, 285 (1985).

14. D. R. O'Keefe, R. L. Palmer, J. N. Smith, Jr. and H. Saltsburg, J. Chem. Phys. 49, 5194 (1968); D. R. O'Keefe, J. N. Smith, Jr., R. L. Palmer and H. Saltsburg, *ibid.* 52, 4447 (1970); Surf. Sci. 20, 27 (1970).

15. R. Schinke, Surf. Sci. 127, 283 (1982).

16. J. P. Cowin, C.-F. Yu, S. J. Sibener and J. E. Hurst, J. Chem. Phys. 75, 1033 (1981).

17. G. Drolshagen, A. Kaufhold and J. P. Toennies, J. Chem. Phys. 83, 827 (1985).

18. J. V. Lill and D. J. Kouri, unpublished work (cited in ref. 47).

19. A. W. Kleyn, A. C. Luntz and D. J. Auerbach, Phys. Rev. Lett. 47, 1169 (1981).

20. A. W. Kleyn, A. C. Luntz and D. J. Auerbach, Surf. Sci. 117, 33 (1982).

21. A. C. Luntz, A. W. Kleyn and D. J. Auerbach, J. Chem. Phys. 76, 737 (1982).

22. A. C. Luntz, A. W. Kleyn and D. J. Auerbach, Phys. Rev. B 25, 4273 (1982).

23. A. W. Kleyn, A. C. Luntz and D. J. Auerbach, Surf. Sci. 152, 99 (1985).

24. G. M. McClelland, G. D. Kubiak, H. G. Rennagel and R. N. Zare, Phys. Rev. Lett. 46, 831 (1981).

25. G. D. Kubiak, J. E. Hurst, Jr., H. G. Rennagel, G. M. McClelland and R. N. Zare, J. Chem. Phys. 79, 5163 (1983).

26. J. A. Barker, A. W. Kleyn and D. J. Auerbach, Chem. Phys. Lett. 97, 9 (1983).

27. H. Voges and R. Schinke, Chem. Phys. Lett. 100, 245 (1983).

28. J. G. Lauderdale, J. F. McNutt and C. W. McCurdy, Chem. Phys. Lett. 107, 43 (1984).

29. J. E. Smedley, G. C. Corey and M. H. Alexander, J. Chem. Phys. 87, 3218 (1987).

30. W. Brenig, H. Kasai and H. Müller, Surf. Sci. 161, 608 (1985).

31. R. Jost and A. Pais, Phys. Rev. 82, 840 (1951).

32. W. Brenig, H. Kasai and H. Müller, Z. Phys. B 60, 489 (1985).

33. T. Brunner and W. Brenig, Surf. Sci. 201, 321 (1988).

34. H. Voges and R. Schinke, Chem. Phys. Lett. 95, 221 (1983).

35. R. B. Gerber, A. T. Yinnon, Y. Shimoni and D. J. Kouri, J. Chem. Phys. 73, 4397 (1980).

36. J. E. Adams, Surf. Sci. 97, 43 (1980).

37. T. R. Proctor, D. J. Kouri and R. B. Gerber, J. Chem. Phys. 80, 3045 (1984).

38. R. Schinke, J. Chem. Phys. 76, 2352 (1982).

39. T. R. Proctor and D. J. Kouri, Chem. Phys. Lett. 106, 175 (1984).

40. R. Schinke and R. B. Gerber, J. Chem. Phys. 82, 1567 (1985).

41. S. Tanaka and S. Sugano, Surf. Sci. 136, 488 (1984).

42. K. B. Whaley and J. C. Light, J. Chem. Phys. 81, 3334 (1984).

43. R. B. Gerber, L. H. Beard and D. J. Kouri, J. Chem. Phys. 74, 4709 (1981).

44. A. O. Bawagan, L. H. Beard, R. B. Gerber and D. J. Kouri, Chem. Phys. Lett. 84, 339 (1981).

45. R. C. Mowrey and D. J. Kouri, J. Chem. Phys. 84, 6466 (1986).

46. H. Tal-Ezer and R. Kosloff, J. Chem. Phys. 81, 3967 (1984).

47. D. Kosloff and R. Kosloff, Jr., J. Comput. Phys. 52, 35 (1983).

48. R. C. Mowrey, H. F. Bowen and D. J. Kouri, J. Chem. Phys. 86, 2441 (1987).

49. L. M. Hubbard and W. H. Miller, J. Chem. Phys. 78, 1801 (1983).

50. G. D. Billing, Chem. Phys. 70, 223 (1982).

51. G. D. Billing, Chem. Phys. 116, 269 (1987).

52. A. M. Richard and A. E. DePristo, Surf. Sci. 134, 338 (1983).

53. A. E. DePristo, Surf. Sci. 137, 130 (1984).

54. C.-Y. Lee, R. F. Grote and A. E. DePristo, Surf. Sci. 145, 466 (1984).

55. D. C. Clary and A. E. DePristo, J. Chem. Phys. 81, 5167 (1984).

56. A. E. DePristo and L. C. Geiger, Surf. Sci. 176, 425 (1986).

57. B. Jackson and H. Metiu, J. Chem. Phys. 84, 3535 (1986).

58. G. Drolshagen and E. J. Heller, J. Chem. Phys. 79, 2072 (1983); Surf. Sci. 139, 260 (1984).

59. B. M. Rice, B. C. Garrett, P. K. Swaminathan and M. H. Alexander, J. Chem. Phys. 90, 575 (1989).

60. D. A. Micha, J. Chem. Phys. 78, 7138 (1983).

61. J. E. Hurst, Jr., G. D. Kubiak and R. N. Zare, Chem. Phys. Lett. 93, 235 (1982).

62. J. C. Polanyi and R. J. Wolf, Ber. Bunsenges. Phys. Chem. 86, 356 (1982).

63. R. Elber and R. B. Gerber, J. Chem. Phys. 79, 4087 (1983).

64. S. C. Park and J. M. Bowman, J. Chem. Phys. 80, 2183 (1984).

65. R. J. Wolf, D. C. Collins and H. R. Mayne, Chem. Phys. Lett. 119, 533 (1985).

66. S. Tanaka and S. Sugano, Surf. Sci. 143, L371 (1984).

67. J. C. Polanyi and R. J. Wolf, J. Chem. Phys. 82, 1555 (1985).

68. J. M. Bowman and S. C. Park, J. Chem. Phys. 77, 5441 (1982).

69. C. J. Ray and J. M. Bowman, J. Chem. Phys. 66, 1122 (1977).

70. R. G. Rowe and G. Ehrlich, J. Chem. Phys. 63, 4648 (1975).

71. S. Saini, D. A. Dows and H. S. Taylor, Chem. Phys. 90, 87 (1984).

72. H. Asada, Surf. Sci. 110, 270 (1981).

73. H. Asada, Japan J. Appl. Phys. 20, 527 (1981).

74. W. L. Nichols and J. H. Weare, J. Chem. Phys. 62, 3754 (1975); *ibid.* 63, 379 (1975); *ibid.* 66, 1075 (1977).

75. M. E. Coltrin and B. D. Kay, J. Chem. Phys. 89, 551 (1988).

76. B. D. Kay, T. D. Raymond and M. E. Coltrin, Phys. Rev. B 36, 6695 (1987).

77. a) R. A. Oman, J. Chem. Phys. 48, 3919 (1968); J. D. McClure, *ibid.* 57, 2810 (1972).
    b) J. Lorenzen and L. M. Raff, *ibid.* 49, 1165 (1968); *ibid.* 52, 1133 and 6134 (1970).

78. J. A. Barker, D. R. Dion and R. P. Merrill, Surf. Sci. 95, 15 (1980).

79. S. A. Adelman and J. D. Doll, J. Chem. Phys. 64, 2375 (1976).

80. J. C. Tully, Acc. Chem. Res. 14, 188 (1981).

81. R. Kubo, Rep. Prog. Theor. Phys. 29, 255 (1966).

82. R. R. Lucchese and J. C. Tully, Surf. Sci. 137, 570 (1983).

83. J. C. Tully, C. W. Muhlhausen and L. R. Ruby, Ber. Bunsenges. Phys. Chem. 86, 433 (1982).

84. H. Zacharias, M. M. T. Loy and P. A. Roland, Phys. Rev. Lett. 49, 1790 (1982).

85. J. Misewich, H. Zacharias and M. M. T. Loy, Phys. Rev. Lett. 55, 1919 (1985).

86. C. W. Muhlhausen, L. R. Williams and J. C. Tully, J. Chem. Phys. 83, 2594 (1985).

87. D. J. Diestler and M. E. Riley, J. Chem. Phys. 86, 4885 (1987).

88. M. E. Riley and D. J. Diestler, Surf. Sci. 175, 579 (1986).

89. H. C. Andersen, J. Chem. Phys. 72, 2384 (1980).

90. Y. Zeiri, J. Chem. Phys. 86, 7181 (1987).

91. H. Goldstein, "Classical Mechanics," 2nd ed. (Addison-Wesley, Reading, MA, 1980).
    a) Chapter 8, specifically equations (8-12).
    b) Equation (10-65).
    c) Section 4-4; the transformation matrices are equations (4-46) and (4-47).

92. J. M. Hammersley and D. C. Handscomb, "Monte Carlo Methods" (Wiley, New York, 1964).
    a) Equation (2.3.21).
    b) Equation (5.2.11).
    c) Equations (2.4.10) and (2.4.11).

93. G. Herzberg, "Molecular Spectra and Molecular Structure II. Spectra of Diatomic Molecules," 2nd ed. (Van Nostrand Reinhold, New York, 1950).
    a) Chapter V, section 2a.
    b) Equations (III,121), (III,150) and (V,12).
    c) Table 39.
    d) Equations (III,94) and (III,100).

94. M. E. Coltrin, M. L. Koszykowski and R. A. Marcus, J. Chem. Phys. 73, 3643 (1980).

95. R. N. Porter and L. M. Raff, in "Dynamics of Molecular Collisions, Part B," edited by W. H. Miller (Plenum, New York, 1976), chapter 1, section 5.

96. J. I. Steinfeld, "Molecules and Radiation" (Harper and Row, New York, 1974), pp. 97-98.

97. F. O. Goodman and H. Y. Wachman, "Dynamics of Gas-Surface Interactions" (Academic, New York, 1976).
a) Section 2.1.
b) Equation (10.1).

98. R. A. LaBudde and R. B. Bernstein, J. Chem. Phys. 55, 5499 (1971).

99. M. K. Gordon, Sandia Laboratories Report, SAND75-0211. For a discussion of the algorithm, see L. F. Shampine and M. K. Gordon, "Computer Solution of Ordinary Differential Equations" (Freeman, San Francisco, 1975).

100. C. W. Gear, "Numerical Initial Value Problems in Ordinary Differential Equations" (Prentice-Hall, Englewood Cliffs, NJ, 1971).
a) Subroutine RK1 on page 84.
b) page 25.

101. E. M. Lifshitz, Sov. Phys. - JETP 2, 73 (1956).

102. J. Harris and P. J. Feibelman, Surf. Sci. 115, L133 (1982).

103. P. W. Langhoff and M. Karplus, J. Chem. Phys. 53, 233 (1970).

104. N. W. Ashcroft and N. D. Mermin, "Solid State Physics" (Holt, Rinehart and Winston, Philadelphia, 1976).
a) Equations (1.37) and (1.38), and Table 1.1.
b) Table 4.5.
c) Tables 23.1 and 23.3.

105. W. A. Steele, "The Interaction of Gases with Solid Surfaces" (Pergamon, Oxford, 1974), chapter 2.

106. N. J. Bridge and A. D. Buckingham, Proc. Roy. Soc. London A295, 334 (1966).

107. J. D. Jackson, "Classical Electrodynamics" (John Wiley and Sons, New York, 1962), equation (4.13).

108. M. Kobayashi and I. Suzuki, J. Mol. Spectrosc. 116, 422 (1986), column 1 of Table IV(b).

109. S. Ron, Y. Shima and M. Baer, Chem. Phys. 101, 45 (1986).

110. L. G. M. Petterson and P. S. Bagus, Phys. Rev. Lett. 56, 500 (1986).

111. F. Illas, J. Rubio, J. M. Ricart and J. A. Garrido, J. Electroanal. Chem. 200, 47 (1986).

112. P. Nordlander, S. Holloway and J. K. Norskov, Surf. Sci. 136, 59 (1984).

113. D. J. Diestler and M. E. Riley, J. Chem. Phys. 83, 3584 (1985).

114. E. Butkov, "Mathematical Physics" (Addison-Wesley, Reading, MA, 1968).
a) Chapter 7, particularly sections 7.1, 7.3 and 7.7.
b) Section 12.1.
c) Section 5.3.

115. N. B. Cabrera, Discuss. Faraday Soc. 28, 16 (1959); R. W. Zwanzig, J. Chem. Phys. 32, 1173 (1960).

116. H. B. Rosenstock and G. F. Newell, J. Chem. Phys. 21, 1607 (1953); E. W. Montroll and R. B. Potts, Phys. Rev. 102, 72 (1956).

117. M. E. Riley, private communication.

118. The equivalence of equation (5.38b) to Tully's result (equation (3.7) of reference 4) is not immediately obvious, since the latter is expressed in terms of the autocorrelation function of the random force. The ghost-atom equation of motion is written out explicitly by Polanyi and Wolf in section IIA of reference 67; their expression for the random force, there denoted by W(Δt), is the same as (5.38).

119. M. E. Riley, private communication.

120. A. D. Buckingham, in "Intermolecular Interactions: from Diatomics to Biopolymers," edited by. B. Pullman (Wiley, New York, 1978), chapter 1.

121. K. P. Huber and G. Herzberg, "Molecular Spectra and Molecular Structure IV. Constants of Diatomic Molecules" (Van Nostrand Reinhold, New York, 1979), p. 476.

122. J. C. Tully, private communication.

123. G. Dolling, H. G. Smith, R. M. Nicklow, P. R. Vijayaraghavan and M. K. Wilkinson, Phys. Rev. 168, 970 (1968).

124. In reference 3, LT state that this set had 96 direct trajectories. However, summing the translational and rotational distributions (parts (b) and (c) of their Figure 3) indicates that there were actually 94 direct trajectories.

125. R. R. Lucchese, private communication.

126. If n_i is the number of (direct) trajectories in the ith bin, n_T the total number of (direct) trajectories and $\Delta\epsilon$ the bin width, then $(N/N_0)_i = n_i / (n_T \Delta\epsilon)$. LT mistakenly used $n_T = 100$ (the total

number of trajectories in the set) rather than $n_T = 94$ (the total number of direct trajectories for the set) when normalizing their distributions (Figure 3 of reference 3). This error has been corrected in the LT results shown in Figures 27 and 28.

127. R. D. Levine and R. B. Bernstein, "Molecular Reaction Dynamics and Chemical Reactivity" (Oxford, New York, 1987), p. 315.

128. A. A. Maradudin, E. W. Montroll, G. H. Weiss and I. P. Ipatova, "Theory of Lattice Dynamics in the Harmonic Approximation," 2nd ed. (Academic, New York, 1971), equation (8.8.31).